

GFZ

Helmholtz-Zentrum
POTS DAM

HELMHOLTZ CENTRE POTSDAM
**GFZ GERMAN RESEARCH CENTRE
FOR GEOSCIENCES**

Johannes Hierold

Analysis of element behavior in mylonites of the Seve Nappe of the Scandinavian Caledonides using different core scanning methods

Scientific Technical Report STR16/07

Recommended citation:

Hierold, Johannes (2016): Analysis of element behavior in mylonites of the Seve Nappe of the Scandinavian Caledonides using different core scanning methods, Master Thesis, (Scientific Technical Report STR; 16/07), Potsdam: GFZ German Research Centre for Geosciences.
DOI: <http://doi.org/10.2312/GFZ.b103-16070>

Supplementary datasets:

Hierold, Johannes., Körting, Friederike, Kollaske, Tina, Rogass, Christian, Harms, Ulrich (2016): "Analysis of element behavior in mylonites of the Seve Nappe of the Scandinavian Caledonides using different core scanning methods" – Operational data sets. GFZ Data Services.
DOI: <http://doi.org/10.5880/ICDP.5054.001>

Description of the supplementary datasets:

Hierold, Johannes., Körting, Friederike, Kollaske, Tina, Rogass, Christian, Harms, Ulrich (2016): Explanatory remarks on the data sets of the master thesis: "Analysis of element behavior in mylonites of the Seve Nappe of the Scandinavian Caledonides using different core scanning methods", (ICDP Data Set Report; 2), Potsdam: GFZ German Research Centre for Geosciences.
DOI: <http://doi.org/10.2312/ICDP.5054.001>

Imprint

HELMHOLTZ CENTRE POTSDAM
**GFZ GERMAN RESEARCH CENTRE
FOR GEOSCIENCES**

Telegrafenberg
D-14473 Potsdam

Published in Potsdam, Germany
December 2016

ISSN 2190-7110

DOI: <http://doi.org/10.2312/GFZ.b103-16070>
URN: urn:nbn:de:kobv:b103-16070

This work is published in the GFZ series
Scientific Technical Report (STR)
and electronically available at GFZ website
www.gfz-potsdam.de



Johannes Hierold

**Analysis of element behavior
in mylonites of the Seve
Nappe of the Scandinavian
Caledonides using different
core scanning methods**

Scientific Technical Report STR16/07



Ernst-Moritz-Arndt-University Greifswald

Department of Geology

**“ANALYSIS OF ELEMENT BEHAVIOR IN
MYLONITES OF THE SEVE NAPPE OF THE
SCANDINAVIAN CALEDONIDES USING
DIFFERENT CORE SCANNING METHODS”**

To obtain the academic degree

Master of Science (M.Sc.)

In the course of studies “Geoscience and Environment”

Written by Johannes Hierold

Born on 18.08.1989 in Eberswalde-Finow

Supervised by:

Dr. Ulrich Harms

(GFZ German Research Centre for Geosciences)

Prof. Dr. Martin Meschede

(Ernst-Moritz-Arndt-University Greifswald)

Potsdam, January 2016

STATEMENT OF AUTHORSHIP

I declare that this Master thesis is the result of my own work and that except where reference is made, it contains no material published elsewhere. No other person's work has been used without due acknowledgement in the main text of the thesis. Statements and ideas which have been used as originally worded or whose meaning has been previously published have been indicated as borrowed, by specifying the source as well as the secondary literature.

Potsdam, January 18th 2016

Johannes Hierold

ACKNOWLEDGEMENTS

The biggest thank of all goes to my supervisor Ulrich Harms for the idea of this thesis. Thank you for your support, for your inspirations and your excellent guidance. Also thanks to my second supervisor Prof. Dr. Martin Meschede who always supported me during my studies in Greifswald. Many thanks have to go out to the persons supporting, supervising or/and providing the measurements. Here I think first of all of Jeannette Meima and Dieter Rammlmair from the BGR in Hannover for leading the EDXRF and LIBS measurements. I also think of Friederike Körting, Christian Rogass and Christian Mielke for the HySpex measurements and the post-processing. Further I would like to thank Tina Kollaske for the support on XRF-measurements and core preparation in Berlin Spandau. Also I thank Ronald Conze for providing expertise and support with all external data sets. Special thanks go to section 6.4 “Zentrum für Wissenschaftliches Bohren”: Ines Thoß, Felix Kraus, Felix Kästner, Knut Behrends, Rüdiger Giese, Thomas Gorgas, Katrin Jaksch, Andreas Jurczyk, Carola Knebel, Kay Krüger, Jochem Kück, Bernd Maushake, Simona Pierdominici, Bernhard Prevedel, Martin Töpfer, Marco Groh and Thomas Wiersberg for being very nice, open minded colleagues who supported me in all situations.

Thanks to my sister Judith Hierold for her commitment to insure a proper linguistic level.

Of course I would also like to thank my family, girlfriend and friends for external motivation and loving support.

Potsdam, January 18th 2016

J.H.

ABSTRACT

The International Continental Scientific Drilling Program (ICDP) performed a dual-phase scientific drilling project to investigate mountain-building processes called Collisional Orogeny in the Scandinavian Caledonides (COSC). The borehole COSC-1 was drilled through the Lower Seve Nappe, as the first of two 2.5 km deep drill holes close to Åre, central Sweden. The recovered rocks comprise a 1650 m thick suite of high grade gneisses and amphibolites with clear Seve Nappe affinities, while the lower 850 m comprise rather homogenous mylonitic gneisses with interfingered K-rich phyllonite bands of cm to several m size and some intercalated amphibolites. The different lithologies all crosscut the core in a subhorizontal direction with foliation of gneisses and phyllonites in the same direction. Albite and garnet porphyroblasts with pressure shadows show syn-deformational growth and the same sub-horizontal alignment.

The focus of this thesis is to detect chemical and mineralogical differences in mylonitic and host rocks and to relate these differences to either metasomatism and deformation or inherited source rock variance. Another goal of this work is to compare chemical core scanning instruments. For this purpose two different μ -Energy-Dispersive X-Ray Fluorescence (μ -EDXRF), Laser Induced Breakdown Spectroscopy (LIBS) and hyperspectral imaging techniques served to measure seven samples from the lower 850 m of the COSC-1 core.

The measurements reveal sharp borders between different rock types without indication of metasomatic changes, pointing to a heterogeneous protolith such as greywacke. Element and mineral maps show strong pervasive ductile deformation with mylonite recrystallization. The comparison of the scanning devices shows that the μ -EDXRF scanner with 50 μ m resolution can be used perfectly for microstructural investigations and heavy element analysis. The XRF core scanner from AVAATECH is very useful and sufficiently precise for element profiles of line scans. The LIBS scanner is great to create distribution maps of elements from H to U with a resolution of 200 μ m. The hyperspectral cameras are extremely fast in acquiring spectral mineral maps and structural information. However, several rock forming minerals in gneisses can currently not be identified and a calibration for metamorphic rocks is still needed.

TABLE OF CONTENTS

Statement of Authorship.....	1
Acknowledgements	3
Abstract	5
Table of Contents.....	7
Table of Figures.....	9
List of Abbreviations	13
1 Motivation.....	15
2 Geological Background of the COSC Drilling Project.....	17
3 COSC-1 Drilling Project.....	24
4 Samples.....	27
5 Methods and Evaluation Software	31
5.1 Laser-Induced Breakdown Spectroscopy.....	32
5.2 X-Ray Fluorescence	34
5.2.1 μ -Energy Dispersive X-Ray Fluorescence Mapping.....	35
5.2.2 Avaatech XRF Core Scanner	37
5.2.3 Minalyze Core Scanner.....	38
5.3 Hyperspectral Image Analyses	40
5.4 Evaluation Software ENVI	45
6 Data Sets and Initial Results	46
6.1 Pre-Existing Data used.....	46
6.2 LIBS Measurements	48
6.3 EDXRF Measurements.....	52
6.4 EDXRF Data of the AVAATECH Core Scanner	57
6.5 Hyperspectral Imaging	59
7 Interpretation.....	65
7.1 Mineral Mapping using LIBS Data	65

7.1.1	Error Discussion	71
7.2	Structural Interpretation using EDXRF Data and Microscopic Investigations....	73
7.3	Comparison of Core Scanning Methods.....	76
7.4	Comparison to Thin Section Microscopy	80
7.5	Integrated Rock Classification	81
7.6	Element Distribution in Mylonites	84
8	Outlook.....	88
9	Conclusion	89
	References.....	90
10	Appendix.....	94
10.1	LIBS Data.....	94
10.1.1	Distribution Maps of Elements Detected	94
10.1.2	Horizontal Profiling on Sample 550	100
10.1.3	Horizontal Profiling on Sample 689	101
10.2	EDXRF Data.....	102
10.2.1	Distribution Maps of Elements Detected	102
10.3	XRF Results of the AVATECH Core Scanner	110
10.4	Diagrams for Comparison of the EDXRF CS Tornado M4, the LIBS CS and the AVAATECH CS.....	114
10.5	Core Sample Photos (On A Scale 1:1).....	116

TABLE OF FIGURES

Figure 1: The Caledonides prior to opening of the North Atlantic Ocean. Modified by Lorenz et al. (2015) from Lorenz et al. (2012).	17
Figure 2: Schematic map and cross-section through the Earth's crust and mantle 600 Ma ago. (Wastenson, et al., 1994).....	18
Figure 3: Schematic map and cross-section through the Earth's crust and mantle 490 Ma ago. (Wastenson, et al., 1994).....	18
Figure 4: Schematic map and cross-section through the Earth's crust and mantle 470 Ma ago. (Wastenson, et al., 1994).....	19
Figure 5: Schematic map and cross-section through the Earth's crust and mantle 425 Ma ago. (Wastenson, et al., 1994).....	19
Figure 6: Possible paleogeographical positions of Baltica (B), Laurentia (L), Siberia (S), Gondwana (G) and Avalonia (A) by (Cocks & Torsvik, 2002) at (a) 500 Ma ago, alternative positions by (van Staal, et al., 2012) at (b) 460 Ma BP, alternative positions after (van Staal, et al., 2012), and (c) at 420 Ma BP, alternative position by (Colpron & Nelson, 2009).....	20
Figure 7: Tectonostratigraphic map of the Scandinavian Caledonides and sketch section along the geotraverse from Östersund to the Norwegian coast. Modified by Lorenz et al. (2015) from Gee et al. (2010).....	22
Figure 8: Location of COSC-1 drill site and the regional geology in the studied area. Modified after Hedin et al. (2012).	25
Figure 9: Section A shows the migrated and depth converted section of the seismic reflection survey CDP Lines (2010) and the interpretation of it by (Hedin, et al., 2012) in Section B. The locations of COSC-1 and optional COSC-2 drill sites are also displayed. Modified after Hedin et al. (2012).	26
Figure 10: Migrated seismic section (left, after Hedin et al. 2015) with simplified lithological column (center, after Lorenz et al. 2015) and depth location and photo of the selected core samples for this study. The numbers next to the sample photos denote the core identifier. The S-numbers in the seismic section denote characteristic reflectors... 30	30
Figure 11: General setup of a LIBS device. Modified after US Army Research Laboratory (2015)	32
Figure 12: LIBS drill core scanner in Hannover. (Photo by Jeannette Meima)	33

Figure 13: EDXRF device M4 TORNADO from Bruker. (www.laboratoryequipment.com, 2015)	35
Figure 14: General setup of a Micro EDXRF device (www.xos.com, 2015).....	36
Figure 15: Avaatech XRF core scanner. (Photo by Johannes Hierold)	37
Figure 16: EDXRF drill core scanner by Minalyze AB (Sjöqvist, et al., 2015).....	38
Figure 17: Illustration of a hyperspectral data cube (Norsk Elektro Optikk AS, 2015) ..	41
Figure 18: General principle of the HySpex. (Norsk Elektro Optikk AS, 2015)	41
Figure 19: Setup of the HySpex hyperspectral camera at GFZ section 1.4. Figure by Friederike Körting, GFZ.....	43
Figure 20: Functioning and key elements of the MICA image cube analysis. (Kokaly, 2011)	44
Figure 21: Preliminary major element contents measured with the new XRF corebox scan instrument along the whole COSC-1 drill core in 0.1m resolution. (Sjöqvist, et al., 2015)	47
Figure 22: Mean intensities of the detected elements of the samples 550, 625 and 689 based on the LIBS data.	49
Figure 23: Distribution map of K in grey scale in sample 550.....	50
Figure 24: Distribution map of K and curve (red) showing the average intensity values of 13 horizontal profiles. The darker non-transparent central band shows the area that was used to calculate this average intensity line.	51
Figure 25: Mean intensities of the detected elements of samples 550, 625 and 689 based on EDXRF measurements with the M4 Tornado.....	53
Figure 26: Distribution map of K in sample 550 with a graph showing the average intensity values of 51 horizontal profiles. The investigated band is the non-transparent area in the central part of the sample.....	54
Figure 27: Results of the horizontal profiling on sample 550 including the elements Si, Al, Fe, Ca and K. In the background sample 550 is illustrated.	54
Figure 28: Horizontal profiling on sample 550 with smoothed values including the elements Si, Al, Fe, Ca and K. In the background sample 550 is illustrated.	55
Figure 29: Horizontal profiling on sample 689 with smoothed values including the elements Si, Al, Fe, Ca and K. In the background sample 689 is illustrated.	55
Figure 30: Linear trends of the elements Si, Al, Fe, Ca and K of the two varying rock section in sample 689. In the background sample 689 is illustrated.....	55

Figure 31: Intensity values of the elements Si, Al, Fe, Ca and K detected with the AVAATECH core scanner in sample 550. In the background sample 550 is illustrated. .	57
Figure 32: Intensity values of the elements Si, Al, Fe, Ca and K detected with the AVAATECH core scanner in sample 689. In the background sample 689 is illustrated. .	58
Figure 33: Classified minerals determined using MICA algorithm based on the hyperspectral data on sample 550. .	59
Figure 34: Classified minerals after MICA algorithm based on the hyperspectral data on sample 625. .	60
Figure 35: Classified minerals after MICA algorithm based on the hyperspectral data on sample 689. .	61
Figure 36: Classified Fe-bearing minerals based on the hyperspectral data on sample 550. .	62
Figure 37: Classified Fe-bearing minerals based on the hyperspectral data on sample 625. .	63
Figure 38: Classified Fe-bearing minerals based on the hyperspectral data on sample 689. .	64
Figure 39: Mineral distribution map classified on LIBS data. Sample 550 with separate sections and the mineralogical composition in percentage, also shown in a data table. .	66
Figure 40: Mineral distribution map classified on LIBS data. Sample 625 with separate sections and the mineralogical composition in percentage, also shown in a data table. .	68
Figure 41: Mineral distribution map classified on LIBS data. Sample 689 with separate sections and the mineralogical composition in percentage, also shown in a data table. .	69
Figure 42: Element Distribution map of Si, Fe, Al, Ca, K and Na in sample 550, showing the schistosity of the mica-rich parts (yellow). .	73
Figure 43: Garnet with so-called pressure shadows (traced with transparent white) to the right and left of the crystal in sample 691. The size of the garnet is approximately 4 mm. .	74
Figure 44: Element distribution map of Si, Fe, Al, Ca, K and Na in sample 689, showing the parallel stretched out texture of the leucocratic gneiss in the left half of the figure and albites porphyroclasts to the right. .	75
Figure 45: Comparison of the K-intensities obtained by LIBS, EDXRF and XRF on sample 550. .	78
Figure 46: Comparison of the Al-intensities obtained by LIBS, EDXRF and XRF on sample 550. .	78

Figure 47: Comparison of the hyperspectral data with the EDXRF results of the Avaatech core scanner.....	79
Figure 48 (Left): Element distribution of Fe (red), K (green) and Si (blue) in sample 550. The white diamonds represent the density values; the yellow lines show the K ₂ O concentration according to Minalyze CS data.	82
Figure 49 (Right): Element distribution of Fe (red), K (green) and Si (blue) in sample 689. The white diamonds represent the density values; the yellow lines show the K ₂ O concentration according to Minalyze CS data.	82
Figure 50: Li distribution map of sample 550 based on LIBS measurements.....	85
Figure 51: Li distribution map of sample 689 based on LIBS measurements.....	85
Table 1: Tectonostratigraphy of the Lower and Middle allochthons in the Jämtland Caledonides by (Gee, et al., 2013).....	23
Table 2: Sample description of the investigated cores. (The IGSN can be resolved e.g. for sample 5054_1_A 550-3 using the url-link: http://hdl.handle.net/10273/ICDP5054EX2Z501).....	29
Table 3: Analytical parameters used for the COSC-1 measurements with the X-ray fluorescence scanner by Minalyze AB (Sjöqvist, et al., 2015)	39
Table 4: Mean intensities of the detected elements of the samples 550, 625 and 689 based on the Libs data.	49
Table 5: Mean intensities of the detected elements of samples 550, 625 and 689 based on EDXRF measurements with the M4 Tornado.....	53
Table 6: Results of the hyperspectral mapping on sample 550 using the algorithm MICA.	59
Table 7: Results of the hyperspectral mapping on sample 625 using the algorithm MICA.	60
Table 8: Results of the hyperspectral mapping on sample 689 using the algorithm MICA.	61
Table 9: Results of the hyperspectral mapping on sample 550 using the algorithm for Fe and Fe-bearing minerals.....	62
Table 10: Results of the hyperspectral mapping on sample 625 using the algorithm for Fe and Fe-bearing minerals.....	63
Table 11: Results of the hyperspectral mapping on sample 689 using the algorithm for Fe and Fe-bearing minerals.....	64

LIST OF ABBREVIATIONS

BGR	Federal Institute for Geosciences and Natural Resources, Hannover, Germany
COSC	Collisional Orogeny in the Scandinavian Caledonides (ICDP Drilling Project)
CS	Core Scanner
DOI	Digital Object Identifier
EDXRF	Energy dispersive X-ray fluorescence
GFZ	German Research Center for Geosciences
ICDP	International Continental Scientific Drilling Program
IGSN	International Geo Sample Number
LIBS	Laser induced breakdown spectroscopy
LTB	Lasertechnik Berlin
Ma	Million years
MICA	Material identification and characterization algorithm
MSCL	Multi-sensor core logger
Nd-YAG	Neodymium-doped yttrium aluminium garnet laser
PRISM	Processing routines in IDL for spectroscopic measurements
RGB	Red, Green, Blue
SWIR	Short wave infrared
USGS	United States Geological Survey
VNIR	Visible- and near infrared
XRF	X-Ray Fluorescence

1 MOTIVATION

This study is integrated in the international Collisional Orogeny in the Scandinavian Caledonides (COSC) scientific drilling project. The main goal of COSC is to understand Himalayan-style mounting building processes by examining mid Paleozoic Caledonian thrust sheets. The Scandinavian Caledonides serve in this context as a prime example of a deeply eroded plate-collision orogeny. Of particular interest is the subducted, far-transported and exhumed Seve Nappe Complex, because of its protracted geological history, partial ultra-high-pressure metamorphism and emplacement with continent-ocean transition zone assemblages onto the Baltoscandian platform.

The 2.5 km deep COSC-1 well was drilled in 2014 within the International Continental Scientific Drilling Program (ICDP). ICDP is a multinational research program offering financial and operational support for international continental drilling projects whose projects are of global geoscientific importance and of societal relevance. The German Research Centre for Geoscience (GFZ) acts as executive agency for ICDP and provides the Operational Support Group.

Site survey seismic data acquired before drilling served to locate a suitable location for the borehole truncating a 2.5 km thick section of the Lower Seve Nappe and a basal thrust zone towards underlying lower-grade allochthon of the so-called Särvi Nappe. However, the cored sequence of leucocratic gneisses and subducted amphibolites did not unambiguously show a simple transition to lower grade rocks, but rather an 800 m thick mylonite-rich zone comprising a few lower-grade metasedimentary rock intercalations.

The goal of this study is to investigate two key aspects:

- 1) Shed light on the composition, origin and tectono-metamorphic evolution of mylonitic gneisses and their relation to the accompanying host rocks.

For this purpose a set of characteristic core samples has been chosen and their chemical and mineralogical composition has been studied with different X-ray fluorescence devices as well as with LIBS and VNIR spectroscopy. The composition of the migmatitic gneisses, quartzo-feldspatic elongated mylonitic gneisses and intercalated K-rich phyllonites is investigated to understand where the strongly deformed rocks are of metasomatic origin or feature compositional differences inherited from their source

rocks. A second task was to shed light on possible changes in element behavior over the 900 m pressure and temperature difference in the mylonitic stack.

- 2) Compare different chemical and mineralogical core scanning methods to derive recommendations for applications in crystalline rocks.

For this purpose the same core samples have been analyzed with three different methods energy dispersive X-ray fluorescence, laser induced breakdown spectroscopy and hyperspectral imaging. Similarities and differences as well as possibilities, advantages and disadvantages of the methods have been developed.

2 GEOLOGICAL BACKGROUND OF THE COSC DRILLING PROJECT

Modern understanding of deep mountain building processes is based on limited surface information on eroded old orogenies and geophysical as well as geological information from active mountain ranges such as the Andes, the Himalayas or the Alps. A well-exposed example of folding and thrusting in the deep crust is the Caledonian Orogeny of Northern Europe.

With a length of more than 2000 km the Caledonides of Scandinavia extend from Stavanger in the south to the Barents Sea in the north. Extensions are reaching much further, as far as East Greenland, Ireland, Great Britain and the Appalachian in Eastern North America, as highlighted in **Figure 1**. All these regions were connected once, before today's North Atlantic broke apart about 65 Ma ago. (Wastenson, et al., 1994)

The Latin word "Caledonian" originates from the Roman emperors of the British Isles, who called a Scottish tribe Caledonians (Krause, 2007).

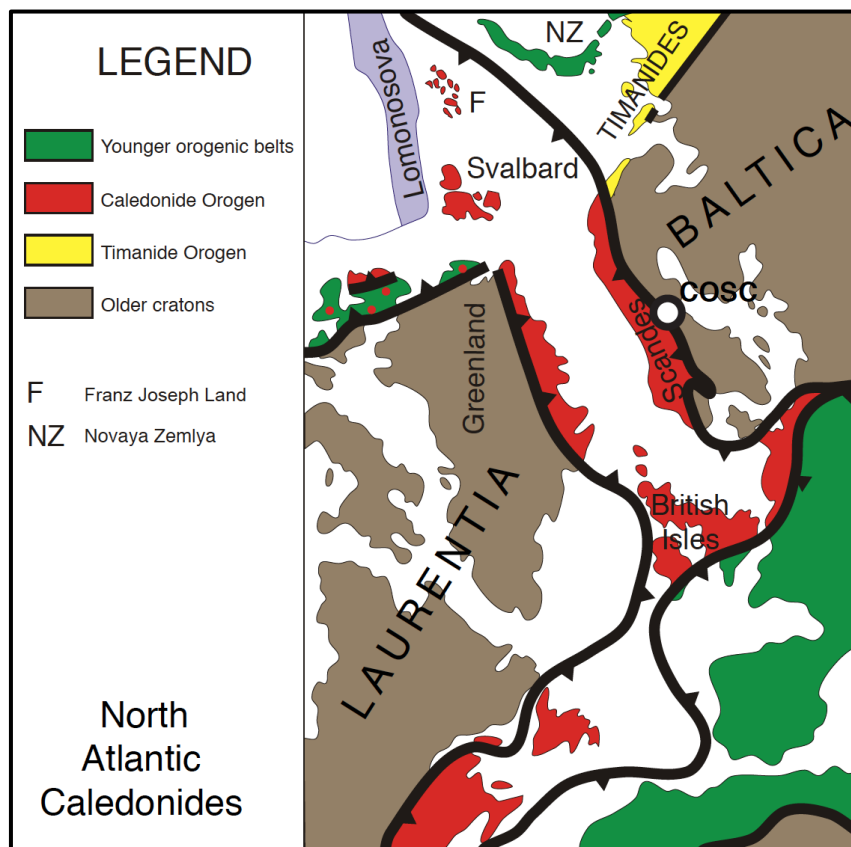


Figure 1: The Caledonides prior to opening of the North Atlantic Ocean. Modified by Lorenz et al. (2015) from Lorenz et al. (2012).

According to Wastenson et al. (1994) the Caledonides were formed when the Iapetus Ocean closed and juxtaposed the ancient continents Baltica, today Northern Europe, and Laurentia, the current North America and Greenland. After Iapetus was completely subducted, the marginal zone of Baltica was forced underneath Laurentia during the continent-continent-collision. A modern analog of such a process is the current collision of the Indian plate with Asia piling up the Himalayas.

The Caledonian orogeny can generally be summarized in three phases. The first phase involves the breakup of the supercontinent Rodinia about 800 Ma ago. At this time Rodinia was situated in the southern hemisphere. The continuing continental rifting process was accompanied by dolerite intrusions about 600 Ma ago (**Figure 2**). (Wastenson, et al., 1994)

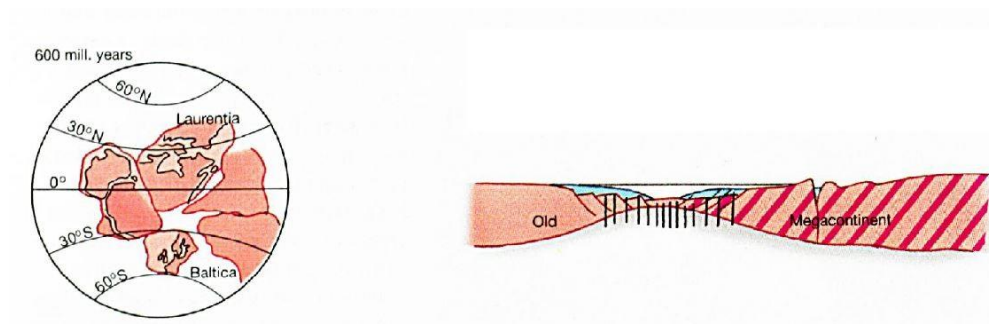


Figure 2: Schematic map and cross-section through the Earth's crust and mantle 600 Ma ago. (Wastenson, et al., 1994)

As a result two continental margins with a transition zone into an oceanic crust of the Iapetus Ocean occurred (**Figure 3**). (Wastenson, et al., 1994)

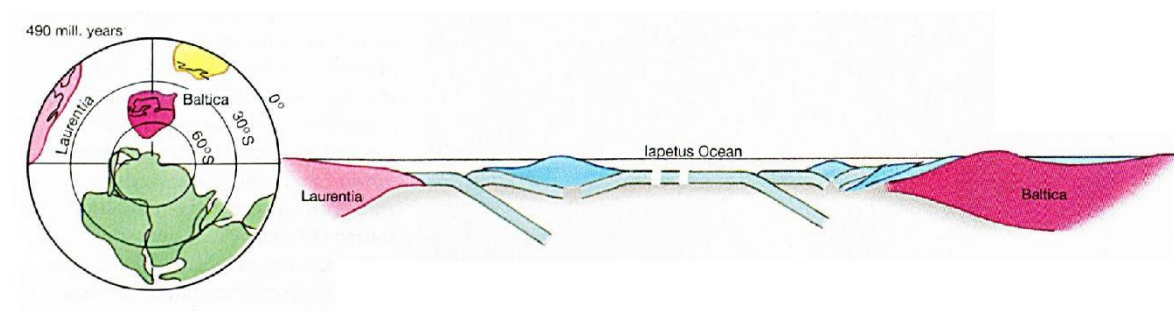


Figure 3: Schematic map and cross-section through the Earth's crust and mantle 490 Ma ago. (Wastenson, et al., 1994)

In the second phase at the end of the Cambrian subduction zones formed, shifting Laurentia towards Baltica at the expense of the Iapetus Ocean. The "western" part of the

continental margin of Baltica collided with an island arc and the outermost margin was subducted down to a depth of about 60 km in some areas as exhumed high-grade metamorphic rocks testify. Subsequently parts of the subducted metamorphosed rocks such as ocean basalts transformed to eclogites were transported upwards in major thrust sheets and nappe complexes. In the later stages of the Ordovician a subduction zone was formed under the continental margin of Laurentia, similar to today's Andes (**Figure 4**). (Wastenson, et al., 1994)

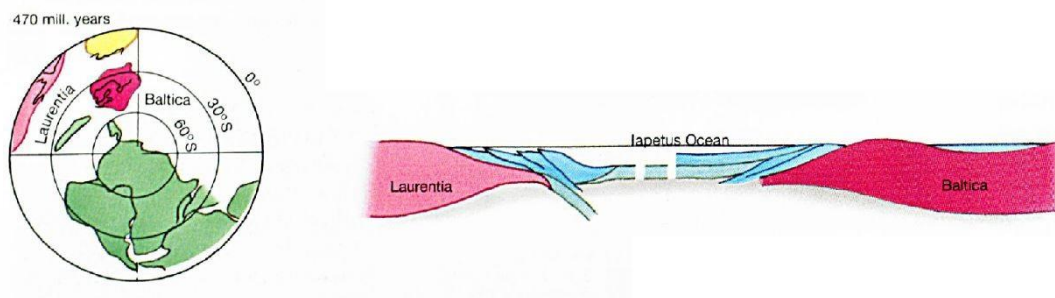


Figure 4: Schematic map and cross-section through the Earth's crust and mantle 470 Ma ago. (Wastenson, et al., 1994)

The third and final phase of the Caledonian orogeny is the continent-continent collision. During the Silurian, Baltica was situated near the equator. The Iapetus Ocean gradually disappeared due to subduction on both sides by Laurentia and Baltica, until it finally came to a continent-continent collision. The result was that Baltica was submerged underneath Laurentia and several thrust zones developed and emplaced nappes onto each other (**Figure 5**). (Wastenson, et al., 1994)

Baltica, the smaller of the two continents, had a similar role as India has in the current Himalaya orogeny process. (Lorenz, et al., 2015)

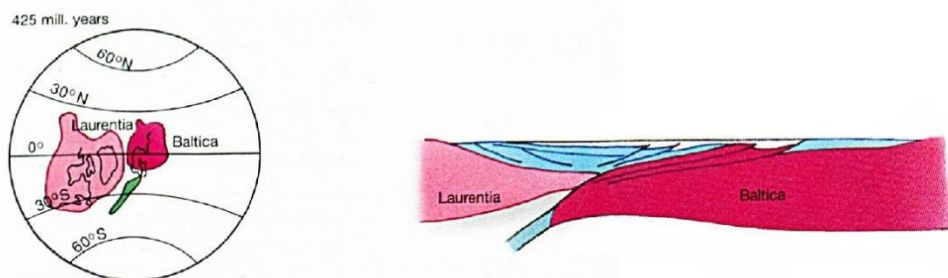


Figure 5: Schematic map and cross-section through the Earth's crust and mantle 425 Ma ago. (Wastenson, et al., 1994)

However, Corfu et al. (2014) claim a more complex plate tectonic setting and collisional system. In their point of view the traditional model is lacking the highly complex architectures of passive margins, which are shaped by hyperextension and mantle exhumation, as well as the presence of continental slivers and micro-continents. The simplified scheme furthermore lists Baltica, Iapetus and Laurentia as the only sources of the Caledonian. Several reconstructions from (Torsvik, 1998; Torsvik, 1996; Torsvik, 2012; Cocks & Torsvik, 2002; Torsvik, 2005) show however that the Caledonian margin of Baltica might have been confronting several seaways on its way to the equatorial position in the Silurian 430 Ma ago, as illustrated in **Figure 6**. The potential paleogeographical positions of the resulting tectonic plate leaves the option of input from other tectonic elements including diverse Siberia-, Gondwana- and ocean-derived units outside of a Baltica-Iapetus-Laurentia system into the Scandinavian Caledonides.

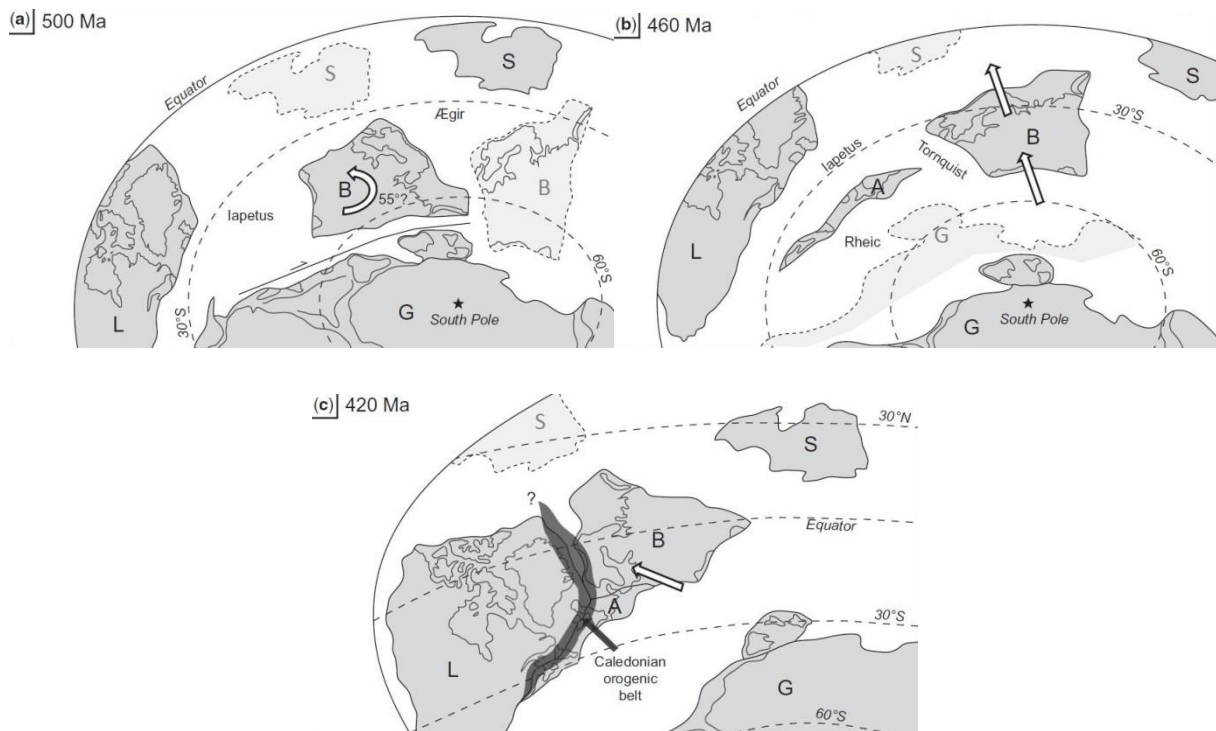


Figure 6: Possible paleogeographical positions of Baltica (B), Laurentia (L), Siberia (S), Gondwana (G) and Avalonia (A) by (Cocks & Torsvik, 2002) at (a) 500 Ma ago, alternative positions by (van Staal, et al., 2012) at (b) 460 Ma BP, alternative positions after (van Staal, et al., 2012), and (c) at 420 Ma BP, alternative position by (Colpron & Nelson, 2009).

Around 400 Ma ago, the western part of the orogenic belt mountain collapsed under its own weight and began to move apart, while simultaneously thrusting continued in the eastern part. (Wastenson, et al., 1994)

According to Gee and Sturt (1985) the Scandinavian Caledonides are primarily characterized by overthrust flat-lying nappes that have been transported up to several hundred kilometers towards east-southeast. At contact with the Baltican basement the Caledonian front proceeds with a single thrust dipping 1 to 2 degree westwards.

Figure 7 shows the tectonostratigraphy of the Scandinavian Caledonides as well as its profile to illustrate the overthrust nappes transported onto the Palaeozoic platform of the Baltoscandian margin. The far-transported nappes are called Allochthon and are differentiated into the Middle, the Upper and the Uppermost Allochthons (Gee & Sturt, 1985). Mostly originated from outer parts of the continental margins, these allochthonous units were subjected to high-grade metamorphism during subduction and uplifted and transported most likely still hot and ductile onto the adjacent platforms (Gee, et al., 2008). Gee and Sturt (1985) state that in general, the metamorphic grade is higher, the higher the Nappes are located in the stacked sequence. In the lowest level units most sedimentary rocks are largely unaffected by metamorphic overprint. The subdivision of the allochthon is listed in detail in **Table 1**. In the prominent Seve Nappe in Central Sweden, the target of the COSC-1 drilling project, ultrahigh pressure metamorphism has recently been identified. According to Gee et al. (2012) thermobarometric results assume peak pressure conditions of approximately 3 GPa and 800 °C within the coesite stability field. This suggests exhumation from depth of over 100 km. Majka et al. (2014) even found microdiamonds in the Seve Nappe further confirming ultrahigh pressure metamorphism overprint. The present lithologies and source rocks of the autochthon and the various nappes of the allochthon differ in composition. A brief summary of each section is listed in **Table 1** and the lithology of the Seve Nappe is explained in more detail below.

The Seve Nappe represents the uppermost part of the Middle Allochthon (Gee, et al., 2013) originating from the outermost continental rim of Baltica, the transition between continental and newly formed oceanic crust (Wastenson, et al., 1994). The Seve Nappe itself can be separated into three main units (Zachrisson & Sjöstrand, 1990): the Lower, Middle and Upper Seve Nappe. The lower part shows protoliths similar to the Särvi Nappe but with amphibolite and regionally eclogite facies deformation. The Middle Seve Nappe consists of migmatites and paragneisses (Arnbom, 1980) that underwent a preceding ultra-high-pressure metamorphism (Klonowska, et al., 2015). The overlying

Upper Seve Nappe is dominated by amphibolites but also comprises micaschists and metapsammities. As Ladenberger et al. (2014) claim, the high-grade metamorphism is of Early Silurian age synchronous with leucogranitic intrusions.

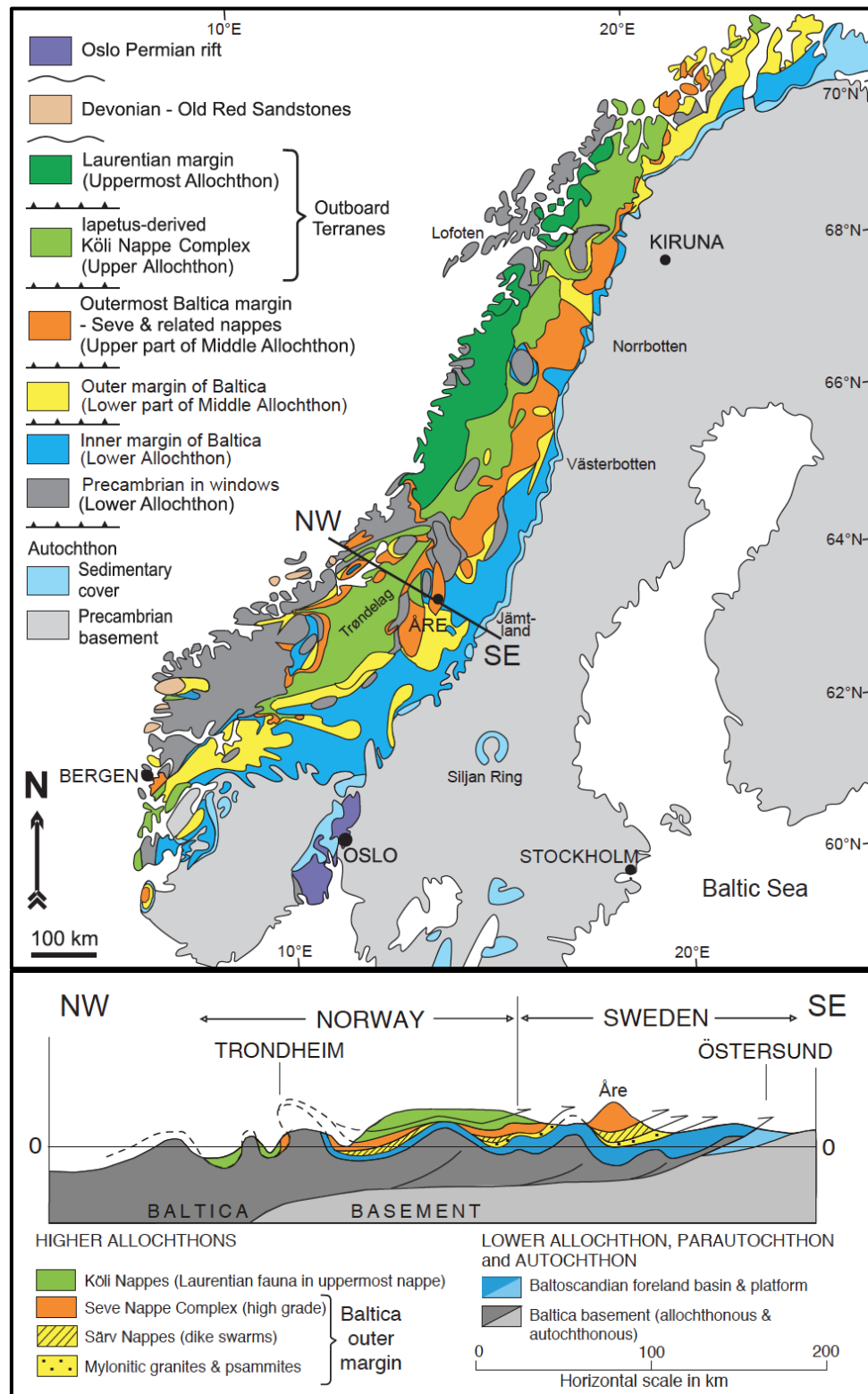


Figure 7: Tectonostratigraphic map of the Scandinavian Caledonides and sketch section along the geotraverse from Östersund to the Norwegian coast. Modified by Lorenz et al. (2015) from Gee et al. (2010).

Table 1: Tectonostratigraphy of the Lower and Middle allochthons in the Jämtland Caledonides by (Gee, et al., 2013).

Tectonic units		Stratigraphy	Lithologies	Age
Upper Allochthon	Köli Nappes	Middle	Greywackes and conglomerates	Llandovery (or younger Silurian)
		Lower	Calcareous phyllites, greywackes, conglomerates with subordinate limestone and quartzites; gabbros and ultramafites (Handöl ophiolite)	Ordovician and Silurian
Major thrusts and subsequent extensional detachments ductile and brittle				
Middle Allochthon	Seve Nappes	Hot extrusion	Amphibolites and psammities granulite facies gneisses and migmatites; amphibolite facies metasediments and schists, marbles, amphibolites and solitary ultramafites	Mainly Neoproterozoic, as in Särvi Nappes
	Särvi Nappes	Tossåsfjället group	Feldspathic sandstones, carbonates and tillites. Dolerite dyke swarms	Neoproterozoic, incl. Vendian
	Offerdal Nappe		Flaggy, feldspathic sandstones	Probably Neoproterozoic
	Granite Mylonite Nappe		Mylonitized crystalline and sedimentary rocks	Palaeo/Mesoproterozoic
	Veman Nappe Tännäs Augen Gneiss Nappe		Coarse augen gneisses and granodiorites (mylonitic and cataclastic)	Precambrian, approx. 1700 Ma
Major ductile shear zones and thick mylonites				
Lower Allochthon	Jämtlandian Nappes (including Early-Mid Proterozoic basement of the windows and minor units in the Caledonian front)	Änge group	Greywackes, black shales, sandstones and limestones	(Wenlock?) Llandovery
		Tåsjön group	Greywackes, shales and limestones	Ordovician and Cambrian
		Sjoutälven group	Quartzite, shales and tillite	Early Cambrian to Ediacaran
		Risbäck group	Feldspathic sandstones, shales and conglomerates	Neoproterozoic
		Frösön, Hoverberget and Mullfjället	Porphyritic rhyolites, sandstones and granites	Mesoproterozoic, approx. 1500 Ma
Major thrusting				
Autochthon	Baltoscandian platform	Tåsjön group	Limestones, alum shales	Ordovician Cambrian
		Basement	Dolerites	1.2 and 1.0 Ga
			Dala sandstones	approx. 1.5 Ga
			Granites and gneisses	1.7–1.8 Ga

3 COSC-1 DRILLING PROJECT

After an initial workshop for the COSC project in 2010, a four years preparation period for the drilling has been implemented, including intensive exploration of the Seve Nappe Complex and the surrounding area. In order to find the ideal spot for the drilling site, a high-resolution reflection seismic survey was conducted in 2010 and 2011. The ideal site was found in a thickened part of the Lower Seve Nappe, including a diverse structure profile and a possible truncation into the lower nappes. A suitable location with necessary infrastructure such as road access was found near the Swedish towns of Åre and Järpen. In **Figure 8** the position of the drill site is marked with the exact coordinates lying at 63°24'6"N 13°12'11" E, as well as the described seismic reflection survey from 2010. A section of the seismic reflection survey, as well as an interpretation (Hedin, et al., 2012) is shown in **Figure 9**. (Lorenz, et al., 2015)

COSC-1 was in operation between the 1st of May 2014 and 26th of August 2014. The total depth was 2495.8 m, the coring section was 2392 m long and the resulting core recovery was 2396 m (100.1 % due to core expansion). The initial 102.8 m were drilled or rammed without core recovery in order to make fast progress. A conductor casing was installed and cemented to that depth. Coring and detailed investigations started at 102.8 m depth. (Lorenz, et al., 2015)

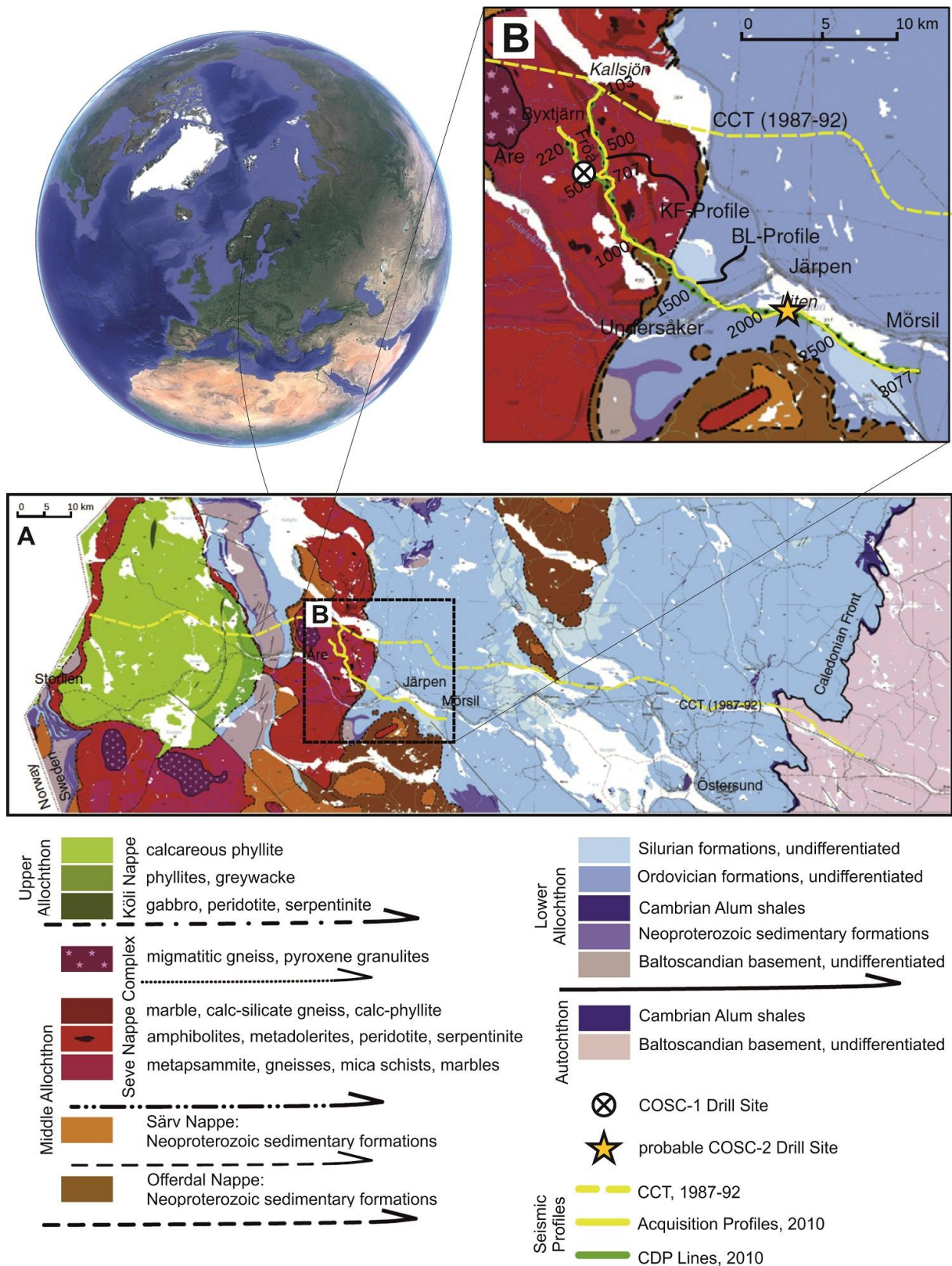


Figure 8: Location of COSC-1 drill site and the regional geology in the studied area. Modified after Hedin et al. (2012).

Next to the COSC-1 drilling project, a second drilling project called COSC-2 is planned for further investigations. The aim of this project will be to understand the basal decollement in a Himalaya-type orogenic process and to yield additional information on the composition, metamorphism and structure of the Lower Allochthon, as well as the footwall alum shale and the underlying Precambrian basement, all of which are below the Seve Nappe drilled during the COSC-1 project. The COSC-2 drilling spot will be located further to the East of COSC-1 as demonstrated in **Figure 9**, to avoid costly ultra-deep drilling. (Lorenz, et al., 2015)

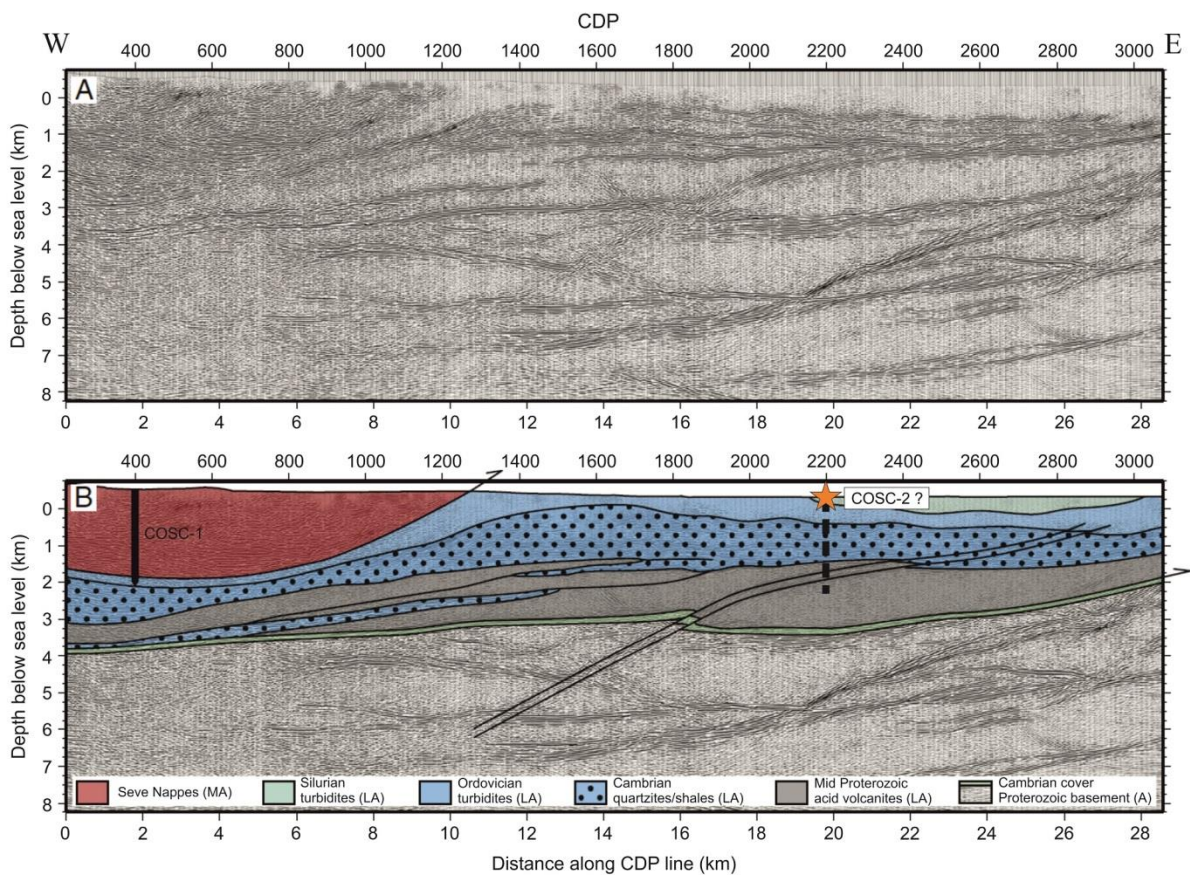


Figure 9: Section A shows the migrated and depth converted section of the seismic reflection survey CDP Lines (2010) and the interpretation of it by (Hedin, et al., 2012) in Section B. The locations of COSC-1 and optional COSC-2 drill sites are also displayed. Modified after Hedin et al. (2012).

4 SAMPLES

All cores of the COSC-1 project are stored in one-meter-long core boxes with 4 or 5 up to 1-m-long pieces of core at the BGR National Core Repository in Berlin-Spandau. Initially three core samples were taken by Dr. Ulrich Harms (GFZ) and Dr. Henning Lorenz (Uppsala University) to study the mica-rich mylonitic bands occurring from about 1500 to 2500 m depth. Sampling was conducted during the sampling party in Berlin-Spandau in February 2015 (Lorenz, et al., 2015). All collected samples originate from different parts of the approximately 900 m thick mylonitized section, show similar mineralogy and contain very mica-rich mylonitic bands.

Mylonitization is the comminution of rocks at tectonic shear planes during ductile deformation under grain comminution combined with syntectonic recrystallization. Mylonites are always hardened and foliated or in some cases show distinct lineation. Some mylonites called augen mylonites can contain lenticular porphyroclasts with pressure shadows similar to augen gneisses. This is also the case in occasional selected samples. Further some of the mylonites found in the selected samples are very rich in phyllosilicates and consequently got the nomenclature phyllonites. (Vinx, 2015)

The samples originally taken by Ulrich Harms and Henning Lorenz comprise 550, 625 and 689 as described in detail in **Table 2**. Four additional core samples have been selected by the author of this thesis at the BGR Berlin-Spandau to study the chemical composition of the samples with the Avaatech core scanner and for comparison with the EDXRF and LIBS methods. These four samples comprise 578, 641, 658 and 691.

In **Figure 10** the location of the investigated core sections are illustrated. **Table 2** shows the description of the studied core samples with their International Geo Sample Number (IGSN), sample-ID, depth, length, the simplified lithologic description and the devices used for investigations. Photos of each core sample in 1:1 scale are provided in the appendix. In the following shortcuts for the sample names will be used as shown in **Figure 10**.

According to the simplified lithologic description (**Figure 10**) the drilled core consists of undifferentiated felsic and mafic lithologies, gneisses with increasing amount of mica schists and mylonite bands and of mylonites. Based on the macroscopic and microscopic investigation on the selected core samples for this thesis, the lithologies of the rocks can

in more detail be described as amphibolites, less deformed gneisses, but also mylonitic elongated gneisses, very mica-rich mylonites that in literature also have the nomenclature phyllonites (Vinx, 2015). In the bottom region of the drilled section additionally solitary marbles were found. The elongated mylonitic gneisses are in general less coarse-grained than the other parts. Some other gneissic areas show migmatitic appearance. In greater depth mylonitic bands seem to become thicker and more frequent and also contain larger porphyroclasts like garnets more often.

Table 2: Sample description of the investigated cores. (The IGSN can be resolved e.g. for sample 5054_1_A 550-3 using the url-link: <http://hdl.handle.net/10273/ICDP5054EX2Z501>)

IGSN	Sample-ID	Short form of sample	Depth from top of section [m]	Length [cm]	Used devices for investigation	Lithology
ICDP5054EX2Z501	5054_1_A 550-3	550	1682.057	15.5	EDXRF; LIBS; Minalyzer; Avaatech xrf scanner; Hypsax	amphibolite, gneiss, flaky mica-rich mylonite, calcite vein
BGRB5054RX25201	5054_1_A 578-6	578	1802.50	15	Minalyzer; Avaatech xrf scanner	very fine grained gneiss with quartz veins on upper core half, on bottom core half: mica-rich flaky mylonite, pyrite, elongated porphyroblasts composed of mica
ICDP5054EX3Z501	5054_1_A 625-7	625	2077.20	19	EDXRF; LIBS; Minalyzer; Avaatech xrf scanner; Hypsax	highly deformed gneiss with quartz veins, some parts with smaller grainsize
BGRB5054RX15201	5054_1_A 641-3	641	2170.17	35	Minalyzer; Avaatech xrf scanner	top 3.5 cm: very fine grained gneiss horizontal lineation, rest mica-rich mylonite, big quartz veins partly with small amphiboles, porphyroblasts composed of mica, garnets up to 5 mm with pressure shadows, albites in flow texture
BGRB5054RX05201	5054_1_A 658-6	658	2273.46	17.5	Minalyzer; Avaatech xrf scanner	middle part fine-grained gneiss, top and bottom part mica-rich mylonite very reflective (mainly sericite), showing flow texture, albites as porphyroblasts, pyrite
ICDP5054EX4Z501	5054_1_A 689-2	689	2456.46	18	EDXRF; LIBS; Minalyzer; Avaatech xrf scanner; Hypsax	mylonitic gneiss with elongated structure and quartz lenses, platy mica-rich mylonite with albite porphyroblasts
BGRB5054RXZ4201	5054_1_A 691-2	691	2469.26	16	Minalyzer; Avaatech xrf scanner	mica-rich mylonite showing flow texture, quartz vein in middle part, garnets up to 5 mm with pressure shadows

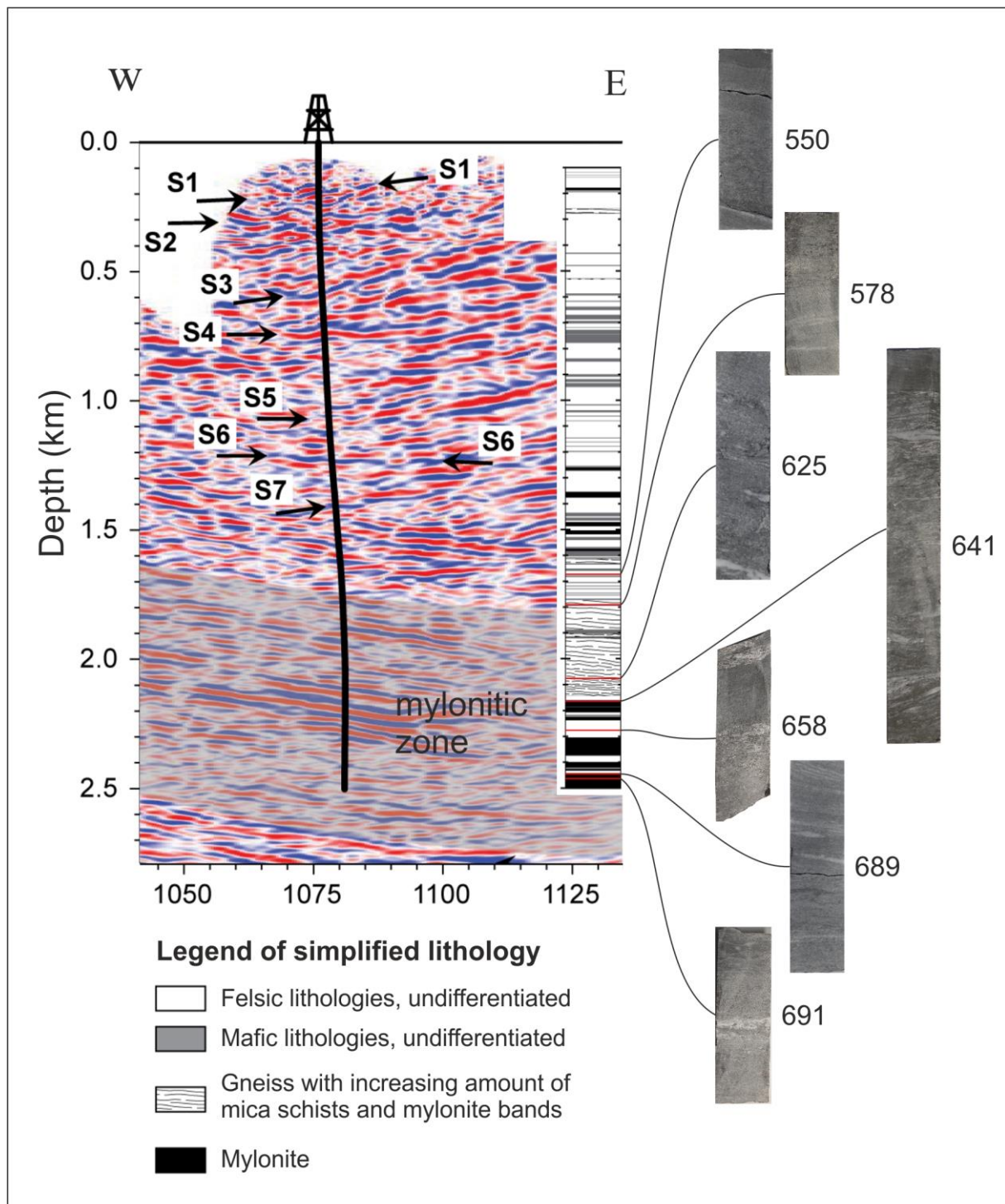


Figure 10: Migrated seismic section (left, after Hedin et al. 2015) with simplified lithological column (center, after Lorenz et al. 2015) and depth location and photo of the selected core samples for this study. The numbers next to the sample photos denote the core identifier. The S-numbers in the seismic section denote characteristic reflectors.

5 METHODS AND EVALUATION SOFTWARE

In order to elucidate differences in the geochemistry and mineralogy of Lower Seve Nappe rocks and microstructures representative for mylonites, the selected core samples have been examined with different analytical methods.

EDXRF- and LIBS-measurements have been performed at the BGR, the Federal Institute for Geosciences and Natural Resources in Hannover. AVAATECH XRF core scanning was conducted in the National Core Repository of the BGR in Berlin-Spandau. In addition, the core samples have been scanned at the GFZ in Potsdam with a hyperspectral camera set. These data have been acquired for comparison with XRF-measurements performed immediately after drilling in fall 2014 on the complete core by the company Minalize AB with a newly developed drill core scanner named “Minalyzer CS” in Gothenburg.

5.1 LASER-INDUCED BREAKDOWN SPECTROSCOPY

The Laser-Induced Breakdown Spectroscopy (LIBS) is an optical atomic emission method that allows for detection of the full spectrum of all elements of a specimen. The general principle of a LIBS device is illustrated in **Figure 11**.

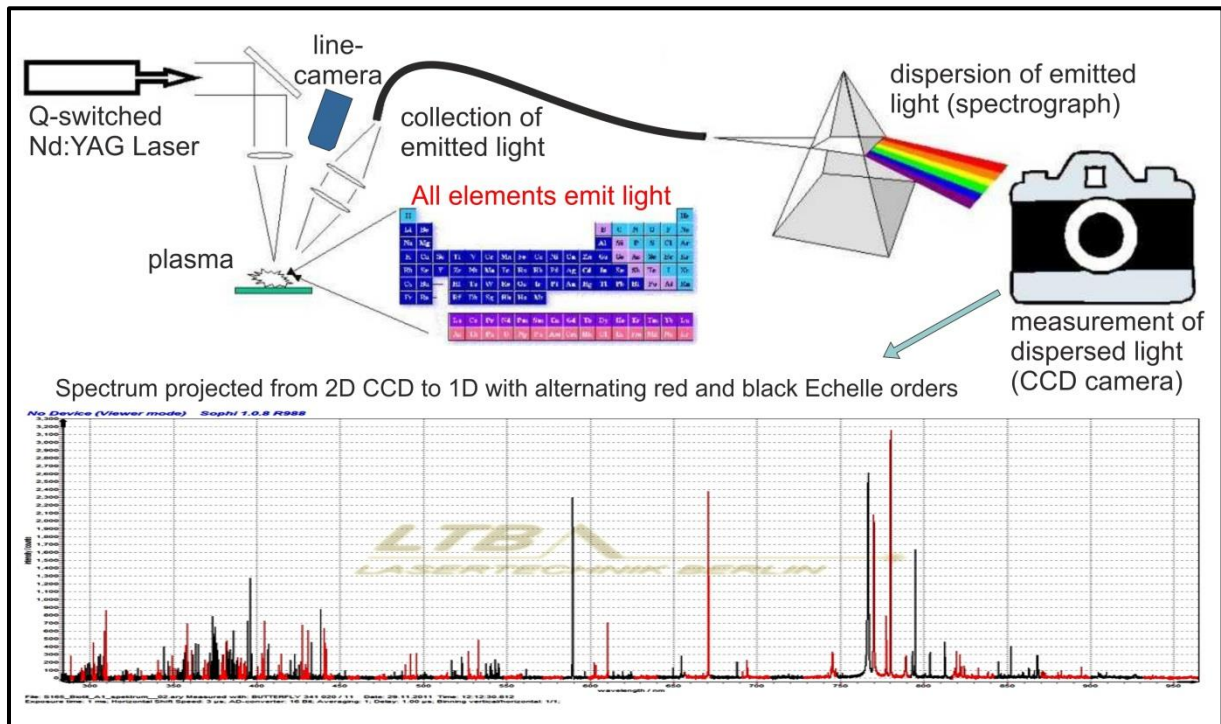


Figure 11: General setup of a LIBS device. Modified after US Army Research Laboratory (2015)

LIBS utilizes a solid-state Nd-YAG-Laser (neodymium-doped yttrium aluminium garnet crystal) as an active medium that emits infrared radiation with a wavelength of 1064 nm in a pulsed form. The Nd-ions of the crystal are either stimulated by a gas-filled tube (xenon or krypton) or with a laser diode. They can be stored as energy in the crystal and released as a short pulse not lasting longer than 10 to 100 ns. Thus high energy radiation several hundred megawatts can be produced. (Graf, 2009)

The laser beam is reflected by a mirror and focused by a lens onto the probe. Consequently a micrometre-sized volume of the specimen is evaporated; this process is called laser ablation. The ablated mass is ionised into a high-temperature plasma containing free electrons, excited atoms and ions. After each laser pulse the plasma starts to cool down, allowing the electrons of the atoms and ions fall down back into natural ground states. This leads to an emission of light with element-specific spectral peaks. The complete spectrum of light is collected, dispersed by a spectrograph and

measured by a CCD camera. The spectrum projected from the 2D CCD can be transformed to 1D with alternating black and red Echelle orders from which the atomic composition can be determined. Every single element from Hydrogen to Uranium can be determined by unique LIBS spectral peaks, representing the individual wavelength of the element. Thus the complete chemical composition of the specimen can be resolved. A quantification of the element concentration is possible by comparison to known samples while a semi-quantitative element content estimation can be given by comparison with other analysing methods. (www.appliedspectra.com, 2015)

The used device is a LIBS drilling core scanner with an Echelle spectrometer is produced as a prototype for the BGR in Hannover by the company LTB (**Figure 12**).

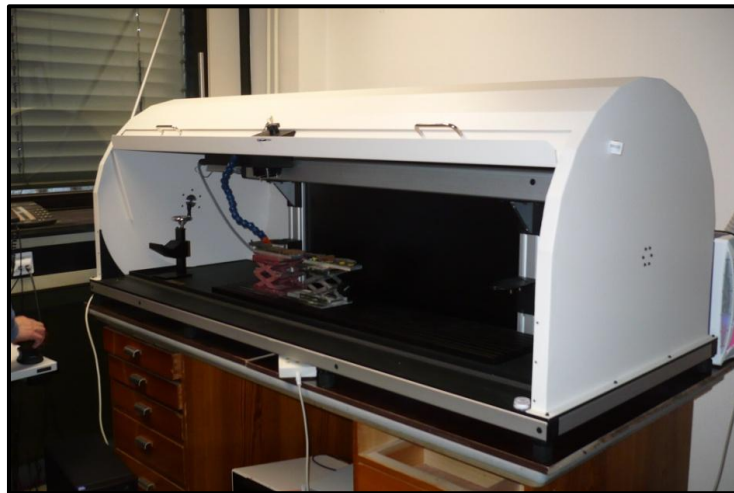


Figure 12: LIBS drill core scanner in Hannover. (Photo by Jeannette Meima)

The measurements have been conducted with a resolution of 0.2 mm. Two laser pulses have been shot per point, to increase the signal strength. The saw-cut drill core sample was detected along a 25 mm wide and up to 1000 mm long band. The accumulated signals have been summarized to one spectrograph. The results of the LIBS measurements have been saved as intensities for selected elements in an ENVI dataset. As the device is in the prototype stage, some measurements had to be repeated due to low-resolution issues. Furthermore, the LIBS measurements are very matrix dependent due to physical and chemical differences in the plasma on the sample surface. The emission lines selected for analysis are often overlain by interferences of other elements. Because a very thin layer of the probe is ablated this method is slightly destructive so that a barely visible slight roughness is produced on the sample surface.

5.2 X-RAY FLUORESCENCE

Energy Dispersive X-ray Fluorescence (EDXRF) is a very well established method for analyzing elements in a solid specimen. In general X-rays are electromagnetic waves which have a wavelength range from about 80 nm down to approximately 0.001 nm. The X-radiation is generated by accelerating electrons towards a cathode in a vacuum tube. When the electrons pass into the cathode metal they are slowed down in the outer field of the atomic nucleus or by variances of bound states of the electrons in the electronic shell of the atom. This process of slowing down electrons produces free-energy released as short wavelength photons called “Bremsstrahlung” causing a typical X-ray fluorescence emission from the probe. Upon treatment with Bremsstrahlung the sample emits secondary or fluorescent X-rays in form of photons with a characteristic energy for each individual element. The electrons are uplifted in a higher electron level according to the Bohr atomic model and release energy in such characteristic photons. An energy dispersive detector combined with a multi-channel analyzer collects the emitted radiation according to wavelength and intensity. By comparing intensities of known samples with unknown samples, the amount of an element in a sample can be determined precisely. (Beckhoff, et al., 2006)

However light elements such as Li or Na emit characteristic x-rays absorbed by the matrix, so they cannot permeate into the detector. Consequently some elements cannot be detected with this method due to their detection limit being too low. Theoretically the lightest element possible to be analyzed is beryllium. However caused by instrumental limitations and low X-ray yields for the light elements, the quantification of elements lighter than Mg was not possible.

5.2.1 μ -ENERGY DISPERSIVE X-RAY FLUORESCENCE MAPPING

A M4 TORNADO EDXRF system of the company Bruker (**Figure 13**) at the Federal Institute for Geosciences and Natural Resources (BGR) in Hannover was used for measurement on COSC-1 samples. This energy-dispersive method is highly sensitive, non-destructive and uses for optimization special X-ray optics a so-called polycapillary X-ray optic. It collects the radiation from the divergent X-ray source and focusses it into a beam of a spot size of e.g. 25 μm . This spatial resolution is much finer than in normal XRF-devices (TORNADO-brochure, 2015), consequently enhancing the spatial resolution and therefore the measurement of trace elements for Micro EDXRF applications like the M4 TORNADO. (Beckhoff, et al., 2006) A general configuration of a Micro EDXRF can be seen in **Figure 14**.

In the M4 TORNADO instruments two instead of one detector units are deployed with the big advantage that the two measurements on the same spot can be compared to minimize crystal reflection effects and increase precision. (TORNADO-brochure, 2015)

An electric voltage of 49 kV and a current of 597 μA were used to register with a very high resolution of 50 μm on the entire half core surface with a measuring time per point of 2 ms.



Figure 13: EDXRF device M4 TORNADO from Bruker. (www.laboratoryequipment.com, 2015)

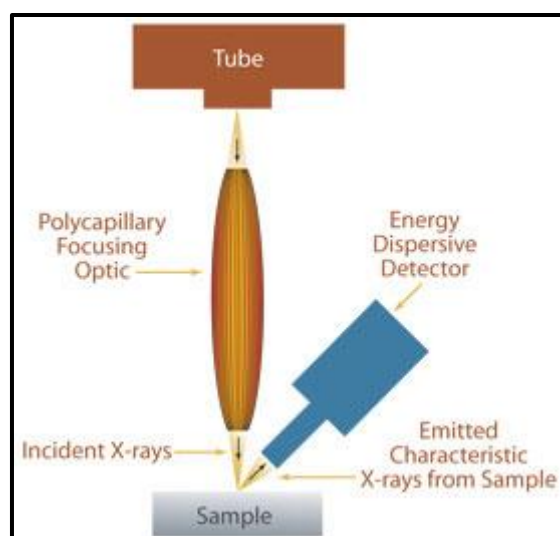


Figure 14: General setup of a Micro EDXRF device (www.xos.com, 2015)

5.2.2 AVAATECH XRF CORE SCANNER

XRF measurements have been performed with an Avaatech XRF Core Scanner of the Dutch company Doeschot, see **Figure 15**. The general functioning of a XRF device is already explained above. The Avaatech Core Scanner has been constructed for a fast and non-destructive determination of the chemical composition on drill cores and similar samples. The system and similar devices of competitors are usual used in Earth sciences for high-resolution point scans on soft-sediment samples for e.g. paleoclimate investigations. The device can however also be utilized to perform analyses on hard rock core samples with the disadvantage of crystal lattice reflections causing enhanced analytical errors. For this study, the XRF measurements were carried out on split cores halved along the longitudinal axis. The core samples were placed along the long axis insight the Avaatech XRF Core Scanner ensuring an even alignment for detection. The utilized analyzing setup consists of an X-ray source with a Rhodium anode and a detector system, both positioned accurately above the sample. Due to a computer controlled positioning system the exact positioning was achieved, even if the core splitting was not along the central axis. The analytical parameters for the Avaatech were 10 kV and 1 mA to detect the elements from Mg to Fe, with a step size of 2 mm and a beam size of 2 cm. The device is connected to a computer, where the data set can be saved and post-processed.

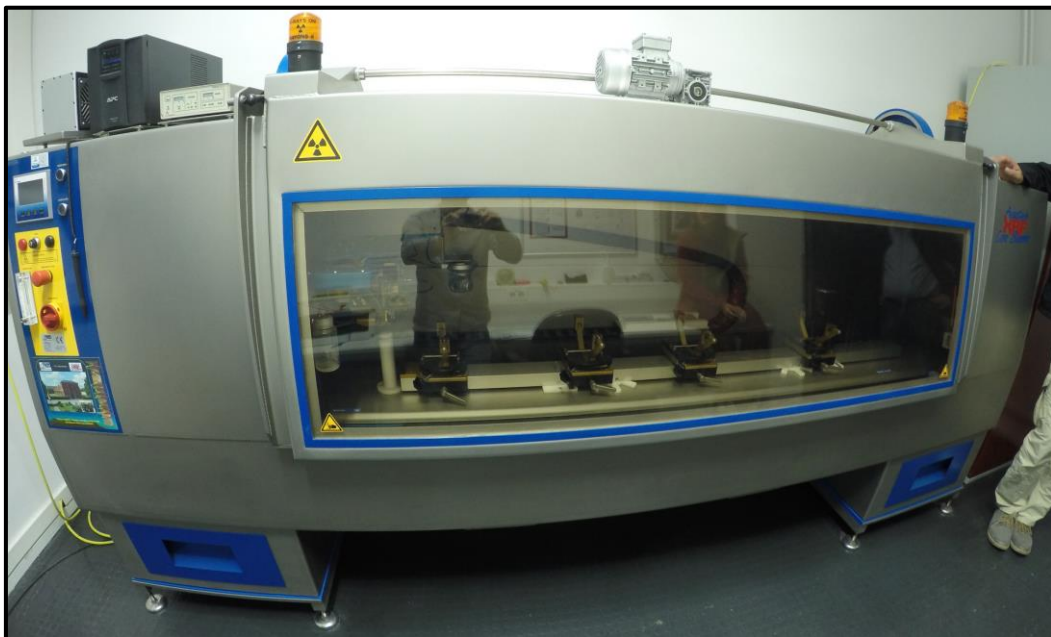


Figure 15: Avaatech XRF core scanner. (Photo by Johannes Hierold)

5.2.3 MINALYZE CORE SCANNER

For comparison with the M4 TORNADO and AVAATECH EDXRF acquired in this study existing data acquired by the company Minalyze on the complete core section of the COSC-1 drilling project have been used. The “innovative optical and chemical drill core scanner”, designed and build by Minalyze AB, a Swedish company specialized on analyzing devices for drill samples is described by Sjöquist et al. 2015.

The measurements have been conducted by Minalyze AB, who provided the data set to the science team of the COSC-1 project.



Figure 16: EDXRF drill core scanner by Minalyze AB (Sjöqvist, et al., 2015).

This scanning device (**Figure 16**) is capable to image high-resolution digital photographs to determine the position of uncut drill cores in core trays and to analyze element content via XRF technique. A scan of 5 m of core in one box can be provided within just 15 minutes. An algorithm, developed by the company calculates the geometry of the core trays, number of slots, length of the cores and so on. A 3-D model of the core provides the needed information about the geometry and location. Additionally it discerns cracks and holes from rock which is also useful for geotechnical purposes such as rock strength. In difference to the EDXRF device of Bruker at BGR, the Minalyze core scanner does not measure pixel per pixel, but is scanning continuously by moving over the probe with a linear beam of 2 cm width and 1 mm thickness. For this purpose the X-ray tube moves along the core surface. The emitted X-rays of the sample are detected by a high-quality Si drift detector (SDD). As illustrated in **Table 3**, where all analytical parameters are shown, the used anode for the COSC-1 investigation is a Cr X-

ray tube anode. Both this system and the EDXRF scanner M4 TORNADO from Bruker work non-destructively. The complete core was scanned using an analysis resolution of 0.1 m. The data over the 0.1 m are integrated.

Table 3: Analytical parameters used for the COSC-1 measurements with the X-ray fluorescence scanner by Minalyze AB (Sjöqvist, et al., 2015)

X-ray tube anode	Cr
Voltage	40 kV
Current	20 mA
Elemental suite	Al, Si, P, S, Cl, K, Ca, Ti, Fe, Cu, Zn, Ga, Rb, Sr, Y, Zr, Nb, Pb
Scanning speed	10 mm s ⁻¹
Analysis resolution	0.1 m

5.3 HYPERSPECTRAL IMAGE ANALYSES

Hyperspectral imaging combines digital imaging with the solar optical spectroscopy. Digital images consist usually of millions of “pixels”, little squares with individual color values, representing different spectral channels. Each of the channels comprises a spectral range within the visible range of red, green and blue. A hyperspectral camera is not only registering the information about the spectral range of the visible light of each pixel, but is also receiving the light intensity, so-called radiance for numerous adjacent spectral bands. Thus each single pixel has a continuous spectrum in radiance or reflectance of the solar optical light at the object and therefore provides a detailed characterization of a sampled area. Due to the huge number of information, hyperspectral images offer a vastly improved ability to classify the objects in the scene based on their spectral properties and thus are very qualified for automated image processing. (Norsk Elektro Optikk AS, 2015)

Originally hyperspectral imaging is being used for satellite-based and airborne remote sensing but it is also applicable for near-field measurements in laboratory setups or outcrops (Norsk Elektro Optikk AS, 2015). Investigations on ores, sediment cores and soil samples are already standard but applications on crystalline rocks are still at the beginning of its development. The reason is mainly that rock forming minerals such quartz and feldspars cannot be differentiated by the visible and near-infrared spectroscopy.

A hyperspectral camera works with a method called “pushbroom”, scanning the image line by line. The light reflected to the sensor is split into its spectral components when reaching the sensor and its solar optical properties are recorded in each line of the acquired image. The array of the sensor works in two dimensions, where one is for the spectral separation and the other one is for imaging in one spatial direction. The latter can be realized by the movement of the camera over the area of interest. In an airplane this happens due to the flight motion, whereas in the laboratory setup, a motorized sleigh is being used moving the samples while the camera is fixed. The resulting image has two spatial dimensions and one spectral dimension, resulting in a data cube, see **Figure 17**. Here every pixel in the image contains one full spectrum. (Norsk Elektro Optikk AS, 2015)

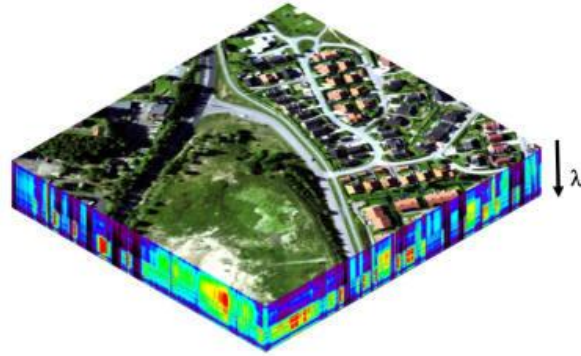


Figure 17: Illustration of a hyperspectral data cube (Norsk Elektro Optikk AS, 2015)

The pushbroom scanning method can be executed by the projection of the scene onto a focusing mirror which sends the focused rays onto a slit only letting light through from a limited line. The passing light is reflected by a collimating mirror, which parallels the rays onto a transmission grating. This separates the different wavelengths and another lens optic finally focuses the light onto a detector array, the sensor. The described principle is displayed in **Figure 18**. (Norsk Elektro Optikk AS, 2015)

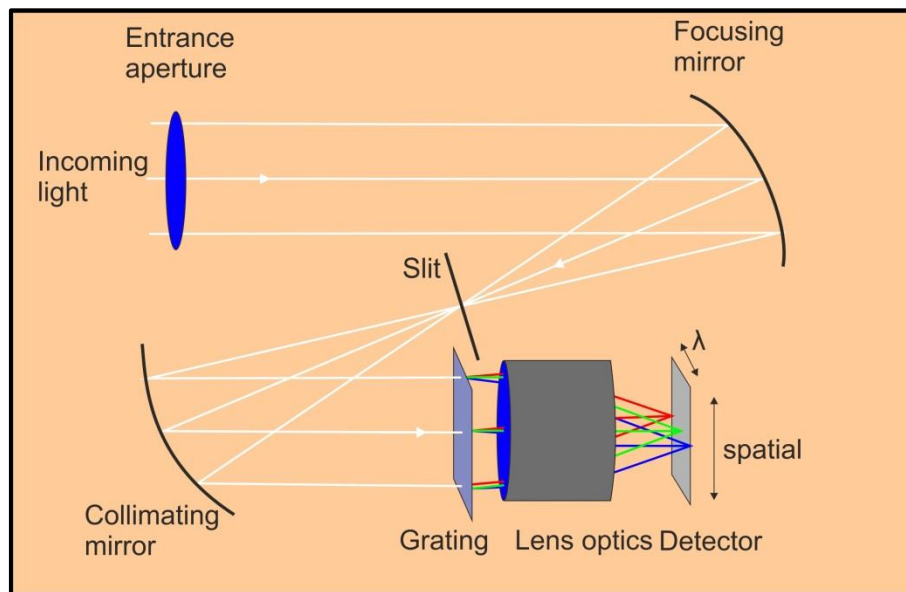


Figure 18: General principle of the HySpex. (Norsk Elektro Optikk AS, 2015)

In this work, the hyperspectral data were acquired using a hyperspectral camera by *HySpex Norsk Elektro Optikk*, Norway. The company produces high resolution, high speed hyperspectral cameras for laboratory, industrial and airborne applications. (Norsk Elektro Optikk AS, 2015)

In contrast to the human eye, capable to sense wavelengths to a maximum of around 700 nm, the HySpex hyperspectral camera is able to detect a much wider range of wavelengths. (Norsk Elektro Optikk AS, 2015)

The HySpex system is using two different sensors. The first one is the HySpex VNIR1600 operating in the visible- and near infrared (VNIR) wavelength region from 400 to 1000 nm and detecting in 160 different channels. The second one is the SWIR320 m-e, which operates in the short wave infrared (SWIR) wavelength region from 1000 to 2500 nm and detects in 256 channels. Consequently the spectral resolution of the VNIR is 3.75 nm and of the SWIR around 6 nm. (www.hyspex.no, 2015)

With the two cameras used, the detection of several minerals is possible based on the reflected wavelength. However, the cameras used are not able to detect neither feldspars nor quartz.

The measurements were performed at the GFZ in the remote sensing lab of section 1.4 Remote Sensing. The purpose-built setup consists of an Al frame with the camera mounted 1 m above the sample sleigh. The construction is static with the sensors pointing vertically, perpendicular to the sample table. The sleigh can be moved mechanically with the desired speed in one direction. The laboratory setup of the HySpex analysis is shown in **Figure 19**.

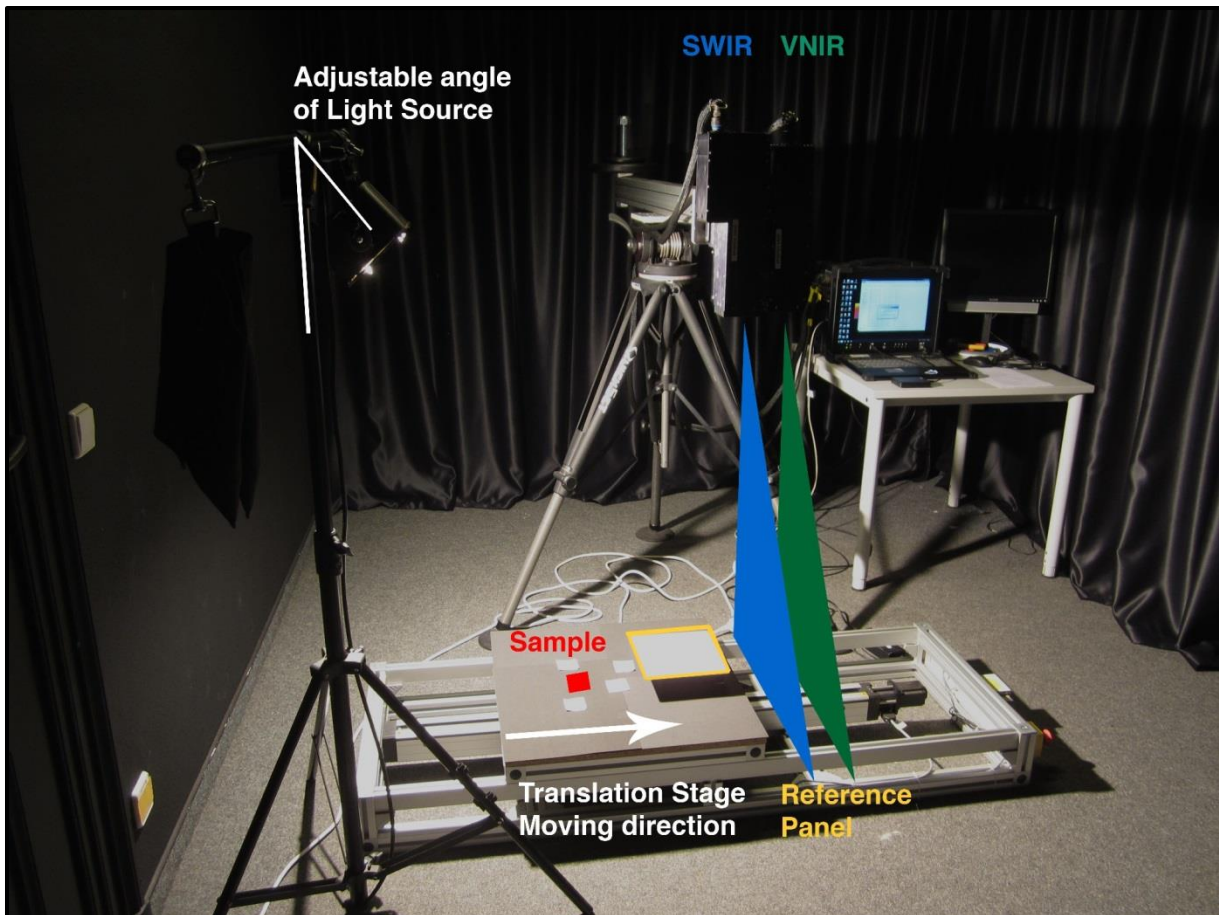


Figure 19: Setup of the HySpex hyperspectral camera at GFZ section 1.4. Figure by Friederike Körting, GFZ.

The measurements were carried out in a lab with dark surfaces to prevent any influence of sun light or reflections that could have an impact on the measurement. The darkness ensures that only the desired light source is utilized in a certain angle towards the sample sleigh. The angle is applied to exclude unwanted shadows and direct interferences with the sensor by avoiding a total reflection at the sample. The utilized lamp emits light in the maximum spectral range of the SWIR. Also important is a so-called reference panel (Spectralon® panels), a reflection standard in front of the sleigh in moving direction. It is used to set a baseline, which can be extrapolated on the complete measurement in the post-processing of the imagery. Through this process all pixel spectra have been normalized.

By using an iterative log-polar phase correlation approach (Rogass, et al., 2013), the VNIR and SWIR image raw data were co-registered and normalized by the described reference panel procedure.

The HySpex data were then processed with the PRISM program, “**P**rocessing **R**outines in **I**DL for **S**pectroscopic **M**easurements”, a software package for hyperspectral mineral analyses created by the USGS. Within this software, an incorporated algorithm called MICA (“**M**aterial **I**dentification and **C**haracterization **A**lgorithm”) was used to identify best fits with reference spectra of known minerals in a spectral library customized for this purpose. The principle of MICA is depicted in **Figure 20**. (Kokaly, 2011)

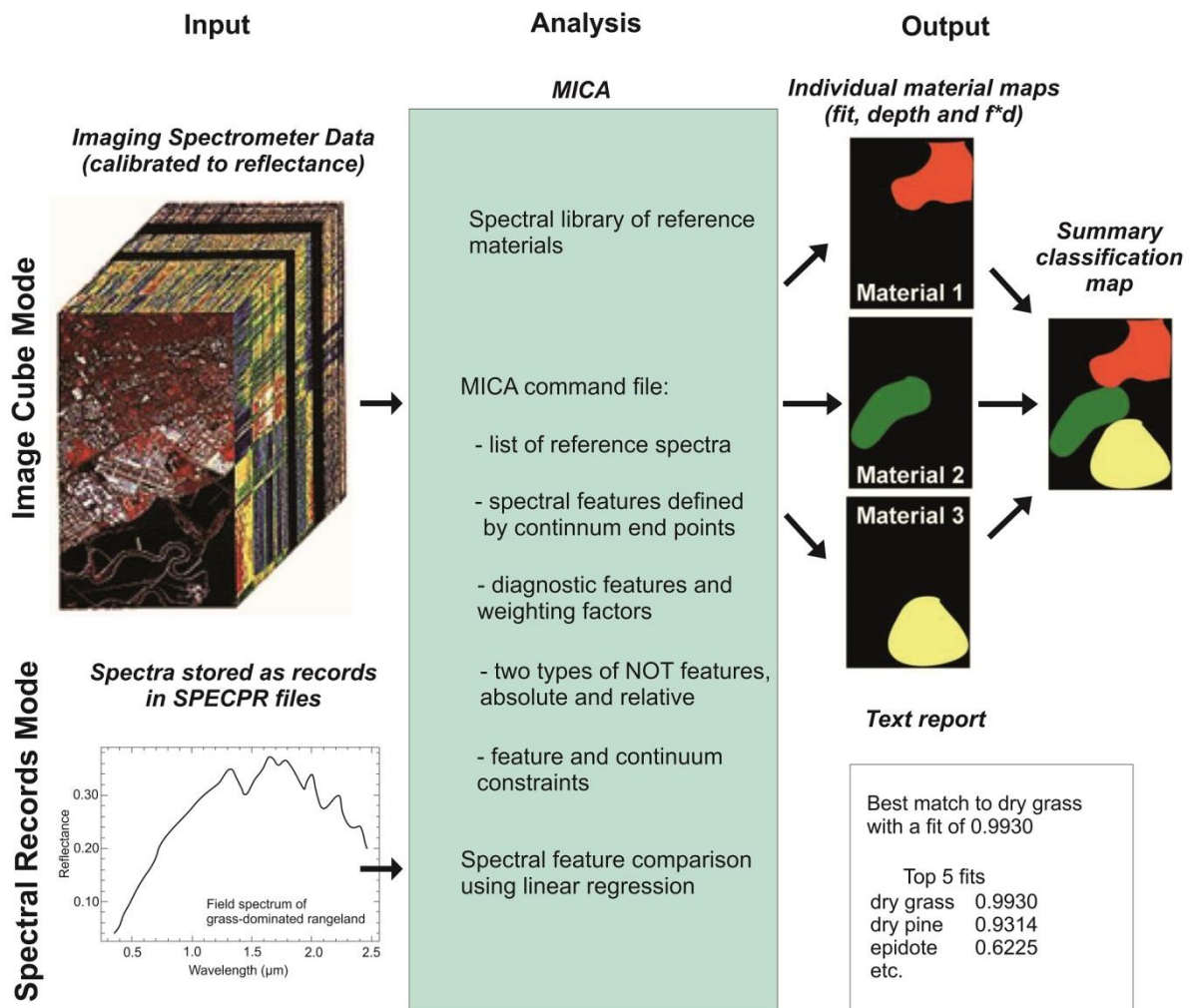


Figure 20: Functioning and key elements of the MICA image cube analysis. (Kokaly, 2011)

5.4 EVALUATION SOFTWARE ENVI

The evaluation of all data measured with the techniques introduced above was performed with the processing software package ENVI “Environment for Visualizing Images”. At the GFZ a few licenses allow utilizing this very large and complex software package. It is usually used in remote sensing or related fields to evaluate measurements, to assess statistical data and to display evaluation results of the data in images. The program can import different types of image formats combined with the additional raster information. Statistical information can be calculated and illustrated in tabular form or as graphs. Additionally data sets can be exported for other programs such as Microsoft Excel.

As described earlier, a digital image consists of pixels arranged in a 2-D grid. Each pixel contains additional information depending on the data source. **Figure 17** shows that an image is made up of multiple bands that can be pictured as layers, all representing the same geographic area but containing different information. This multispectral data can be illustrated through ENVI by choosing a single or several bands. In hyperspectral images for example the different bands represent the intensity of the reflected light in the wavelengths. Together with algorithms like MICA it is possible to create images consisting of several bands referring to the spatial occurrence of different mineral assemblages in the image. In the XRF data the bands stand not for minerals but for the individual elements with their characteristic wavelength.

By loading the data set into ENVI, distribution maps of single elements can be illustrated and statistical data sets of the complete sample, selected areas or profiles can be made. The pixels are displayed either in grey tones or in colors for demonstrating the intensity of the elements.

ENVI offers other functions such as loading the information of three bands/elements simultaneously as an RGB color map and for the identification of characteristic minerals. Another useful application is the “Region of Interest (ROI)” tool. Regions can be chosen by selecting areas of the sample, or by displaying distributions of bands. For the classification of minerals for example, regions of interest were chosen based on the distribution of the high intensity of an element e.g. Si in order to derive quartz distribution. A mineral classification map can be created as a result.

6 DATA SETS AND INITIAL RESULTS

6.1 PRE-EXISTING DATA USED

The data initially acquired during the drilling comprise the lithological descriptions, the MSCL data and the XRF logging data and were used by the author of this thesis. This pre-existing data have been uploaded to the ICDP Drilling Information System (DIS) and have been published already (Lorenz, et al., 2015), but is digitally available for ICDP Science Team members only until the moratorium period ends on 2017-03-01. After that a public access will be arranged.

The data sets produced during the course of this study are attached in electronic form and have been uploaded to the Drilling Information System (DIS) data bank at ICDP and will be available for public access after the moratorium period of two years. The data will be published electronically on the ICDP web page with the DOI: 10.1594/GFZ.SDDDB.ICDP.5054.2016. The Digital Object Identifier (DOI) is a serial code used to uniquely identify objects. The explanatory document has the DOI: 10.2312/ICDP.2016.001.

The included data set of the XRF measurements by Minalyze AB have been published already in form of oversight results by Sjöqvist, et al. (2015). **Figure 21** shows the chemical data of elements of the COSC-1 core measured with the Minalyze core scanner.

The initial lithological core description acquired during drilling at the drill site has been used for this thesis. In addition, also information about the density, p-wave-velocity, magnetic susceptibility, impedance and other geophysical properties have been measured by the COSC-1 science team members during drilling with a Geotech MSCL core scanner. Furthermore the complete core has been scanned on the drill site with an optical 360°-core scanner, resulting in digital photos of each section of the core. The complete set of digital photos can be uploaded into a program called “corelyzer”. Additionally, all other core data can be loaded into the software and can be laid over the core images. Hence the geochemical and geophysical data measured can be put in context with the lithology of the core.

An interpretation of the pre-existing geophysical and geochemical data with an integrated context to the other results will follow in the chapter “*Integrated rock classification*”.

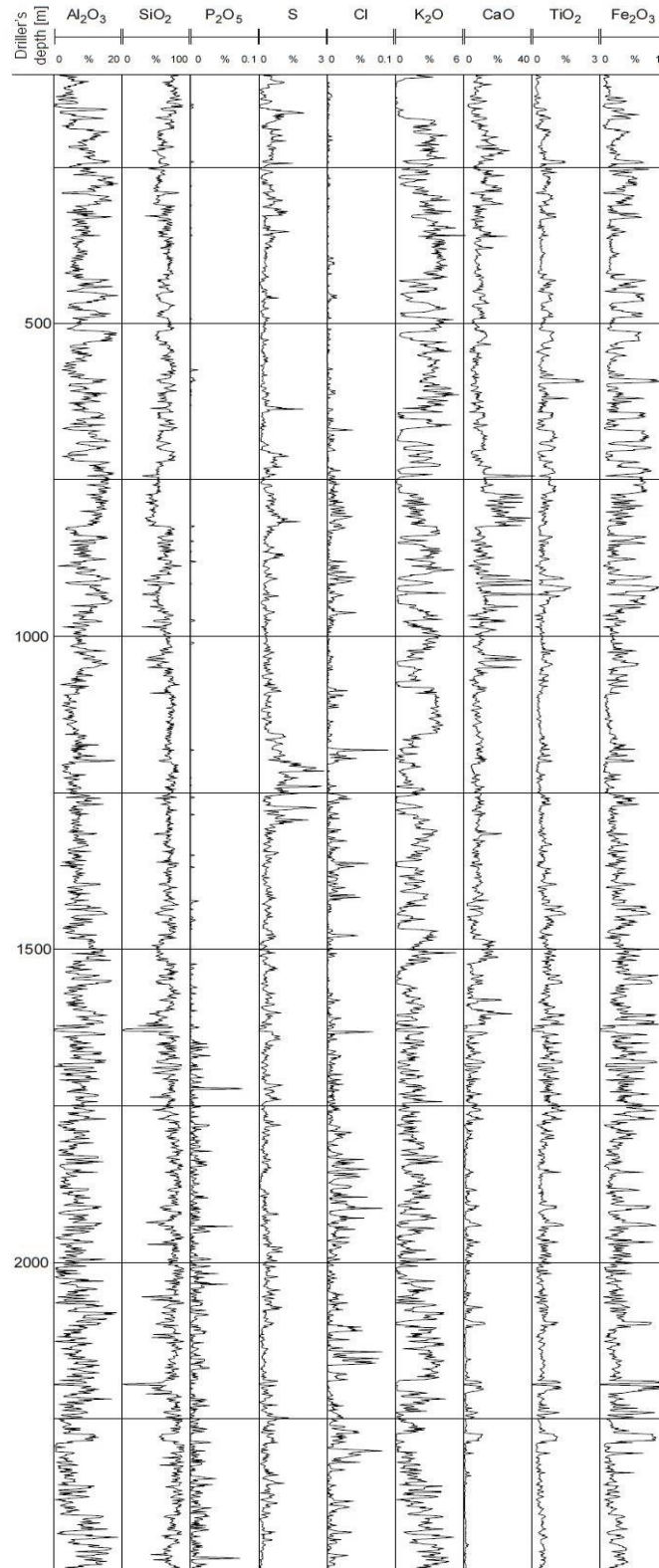


Figure 21: Preliminary major element contents measured with the new XRF corebox scan instrument along the whole COSC-1 drill core in 0.1m resolution. (Sjöqvist, et al., 2015)

6.2 LIBS MEASUREMENTS

LIBS measurements have been carried out on the core pieces 550, 625 and 689. For this purpose all samples have been placed inside the LIBS core scanner at the BGR in Hannover. After the scanning procedure, the data set was loaded into the evaluation software ENVI Version 5.2. The data set consists of 50 bands representing the intensities of different elements. Some of the elements are represented by several bands, because they demonstrate the wavelength of K- and L-shells of the atoms. Also the data of the elements Ba, Co, Cr, Cu, Mn, P, S and Zr had to be normalized and calibrated in a post-process resulting in multi-allocation. In the end only 17 different elements have been used for further analysis. These are the major elements: Si, Ti, Al, Fe, Mn, Mg, Ca, Na, K, P and the trace elements B, Ba, Ca, Co, Cr, Cu, Li, Nb, S, Y and Zr. However, the elements B, C, Nb and Y did not provide any suitable data and were not used for further interpretation.

A diagram showing the mean intensities of the elements detected in the samples 550, 625 and 689 is depicted in **Figure 22**. The measured intensities can be found in the corresponding **Table 4**.

Noticeable differences between the samples can be determined for almost all elements. The mean intensity value however does not represent directly the quantitative chemical composition of the specimen. The partially large deviations between the elements can be attributed to quantum mechanical properties. As already explained, LIBS is a method of emission spectroscopy. Atoms have different energy levels. With the laser of the LIBS, atoms can be brought onto a higher energy state. The energy needed to achieve the different levels varies with each element. Thus some elements like Na and K will be excited easily, while others like Cl and Br will be harder excite. Thus the LIBS spectrum indicates the energy transitions between different energy levels of atoms. The intensities of the individual emission lines are in particular dependent on the concentration, the occupation number and quantum mechanical selection rules. This means that the mean intensities do not give information about the quantitative chemical composition. Comparing the mean values of a single element in all three samples however can provide qualitative information about the presence of the element.

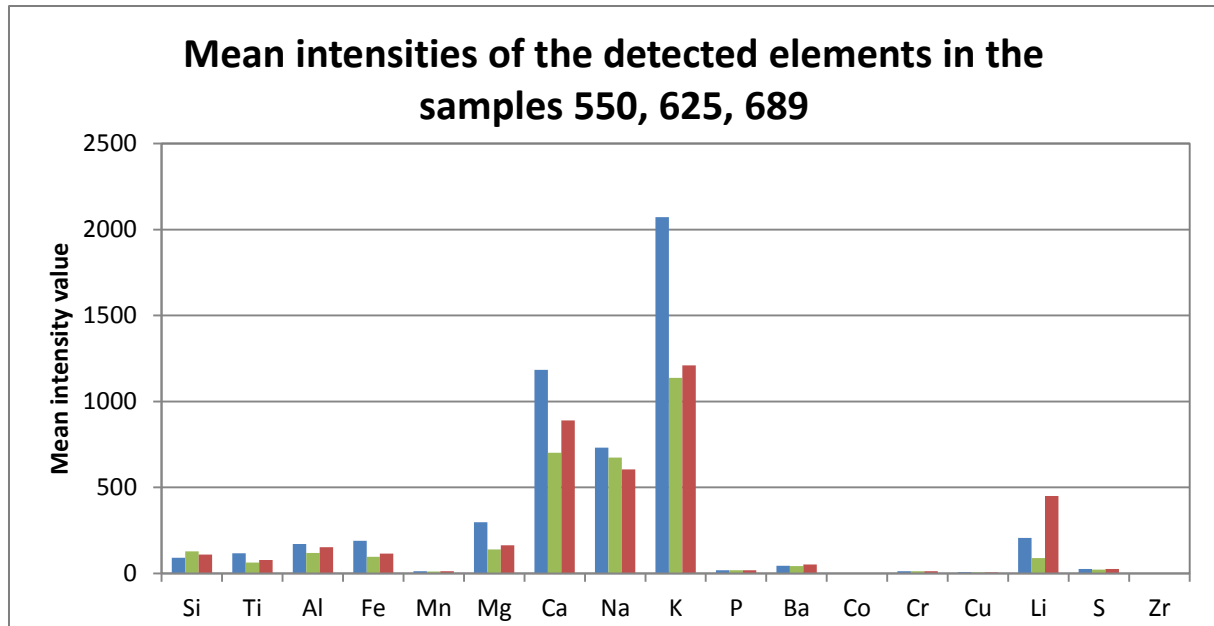


Figure 22: Mean intensities of the detected elements of the samples 550, 625 and 689 based on the LIBS data.

	■ Sample 550	■ Sample 625	■ Sample 689
Si	91.1293	128.5935	109.8443
Ti	117.6594	64.1168	78.7385
Al	171.1883	119.9786	153.3970
Fe	189.6465	97.7450	116.0022
Mn	13.6145	11.6354	12.4826
Mg	298.0276	140.4433	163.5255
Ca	1184.6416	702.2247	890.4014
Na	732.1856	673.3439	604.9425
K	2073.0866	1136.9010	1210.7510
P	17.7638	17.7741	18.1610
Ba	44.1096	41.9646	51.3802
Co	0.1904	0.1284	0.0263
Cr	12.5700	12.6253	12.4996
Cu	7.3588	5.4711	4.7696
Li	207.2396	89.5568	450.8311
S	26.3792	21.7435	26.4159
Zr	0.7738	1.6505	1.0603

Table 4: Mean intensities of the detected elements of the samples 550, 625 and 689 based on the Libs data.

Considering K as an example, the mean intensity in sample 550 is higher than in samples 625 and 689. This means that in sample 550 in general there were more pixels counted, corresponding to a higher intensity than in the other two samples.

For detailed investigation, maps showing the spacial distribution of the selected element were created. As an example **Figure 23** shows a distribution map of the element K of sample 550 in grey scales with the rule: the brighter the color, the higher the concentration at this particular spot. The same procedure was realized on all elements and on all three samples 550, 625 and 689 to point out chemical differences between the three samples as well as in different parts of each individual sample. These distribution maps can be found in the appendix.

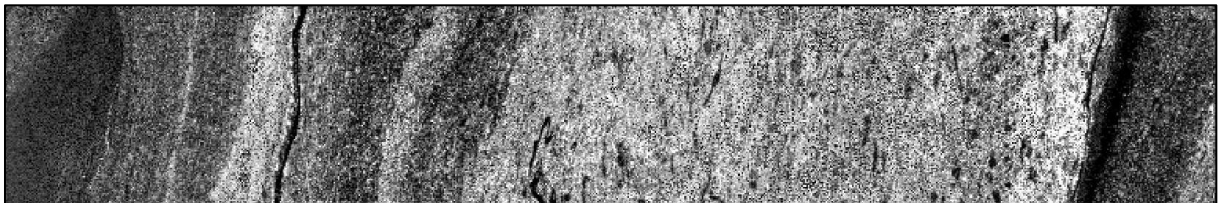


Figure 23: Distribution map of K in grey scale in sample 550.

On the elements Si, Al, Fe, Ca and K horizontal profiling was further used to point out chemical differences along the core samples, particularly along the macroscopic identified phyllonitic bands to the surrounding rock. Due to the identical diameter, the elemental distribution maps of all three samples 550, 625 and 689 consist of 125 vertical pixels resulting in 125 horizontal profiles. To get more reliable statistics a band of 13 horizontal profiles from the center part of each core piece was selected and mean values were calculated. The area covered with this data set is 2.55 mm wide and as long as the whole core sample. Horizontal profiling was first applied on the EDXRF data, where 51 horizontal lines created a band of 2.55 mm wideness. To get comparable results of the same area, 13 profile lines from the LIBS data were used to cover the same area. This approach was chosen to analyze whole rock chemistry of an area instead of single point compositions. The combined 13 bands of the distribution map clearly show chemical differences in the samples, see **Figure 24**. The graph displays the results of the element distributions in the sample. The dark blue areas in the distribution map are highlighting the areas of the lowest K intensities. As assigned in the legend, the dark red areas show areas of high K content. The areas of high K content are concentrated in areas where potassium-rich K-feldspars and micas were identified with the binocular.

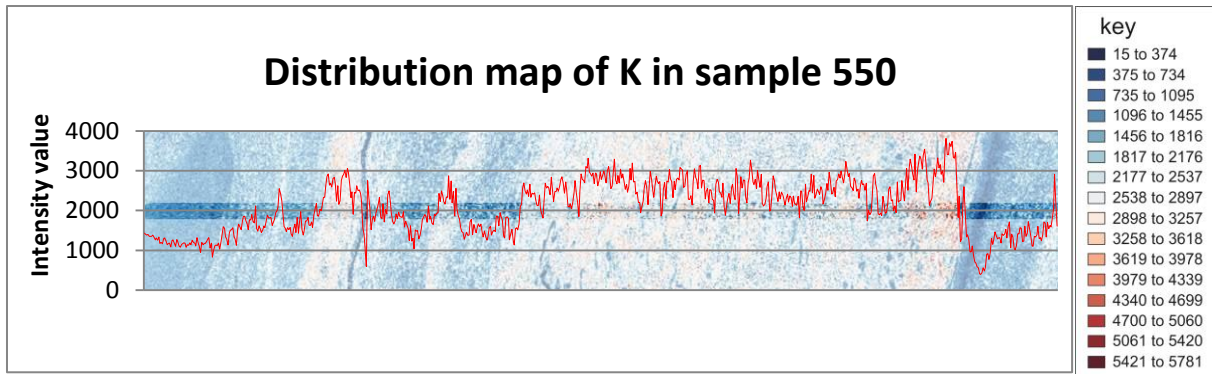


Figure 24: Distribution map of K and curve (red) showing the average intensity values of 13 horizontal profiles. The darker non-transparent central band shows the area that was used to calculate this average intensity line.

The diagrams showing the results of the horizontal profiling for the elements Si, Al, Ca and Fe are attached in the appendix. Additionally the diagrams of sample 689 can be found in the appendix.

6.3 EDXRF MEASUREMENTS

EDXRF measurements with the M4 TORNADO instrument have been carried out on the core pieces 550, 625 and 689. The resulting data set was loaded into an analytical software included in the Bruker tool to create a tiff-image of each element. The image contains all acquired data such as the element intensities at each measured point. The images were imported into the evaluation software ENVI for further analyses.

With the M4 TORNADO 24 elements have been measured, including the major elements: Si, Ti, Al, Fe, Mn, Mg, Ca, Na, K, P and the trace elements Ba, Cl, Co, Cr, Cu, Nb, Ni, Pb, Rb, S, Sr, V, Y, Zn and Zr. The elements Ba, Na, Cu, Nb, Ni, Rb, Sr, Y, Zn and Zr were not used for interpretation because their content was either below the detection limit of this tool or they were randomly distributed without structural or mineralogical relation. The distribution maps of all analyzed elements of the samples 550, 625 and 689 are attached in the appendix.

A comparison of the mean intensities of the detected elements in the samples 550, 625 and 689 is displayed in **Figure 25**. It highlights the differences in composition for all samples, e.g. the mean intensity value of Si in sample 550 is the lowest and in sample 625 the highest. The mean intensities of Fe and K are higher in samples 550 and 689 in comparison to sample 625.

Comparable to the LIBS data, distribution maps of all 14 elements determined on samples 550, 625 and 689 were displayed in grey scale and can be found in the appendix.

Horizontal profiling as described above has been carried out on the elements Si, Al, Fe, Ca and K. A band of 51 horizontal profile lines has been used to cover an area of 2.55 mm along the sample axis and to derive mean element values. As an example the distribution of K for sample 550 as well as the results of the horizontal profiling is displayed in **Figure 26**.

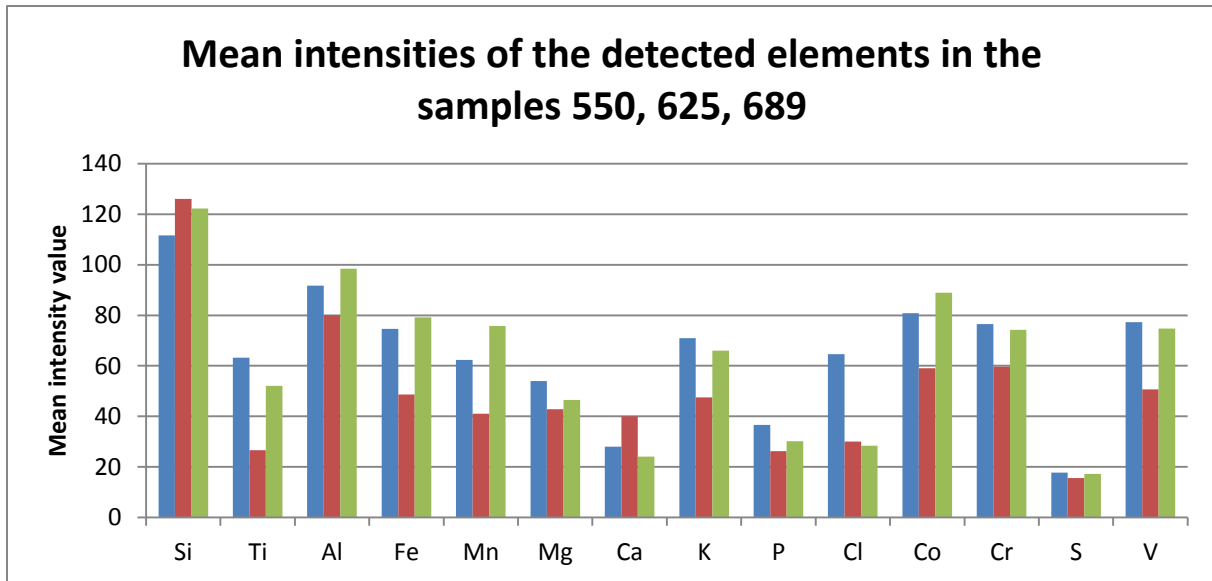


Figure 25: Mean intensities of the detected elements of samples 550, 625 and 689 based on EDXRF measurements with the M4 Tornado.

	■ Sample 550	■ Sample 625	■ Sample 689
Si	111.5707	126.0048	122.2779
Ti	63.2358	26.5848	52.1126
Al	91.6750	80.0574	98.4926
Fe	74.6578	48.6830	79.1383
Mn	62.3758	40.9969	75.7261
Mg	54.0120	42.8602	46.4932
Ca	27.9948	40.0043	24.1006
K	70.9625	47.5603	66.0025
P	36.6041	26.1922	30.1189
Cl	64.5978	29.9838	28.3278
Co	80.7692	59.0238	88.9203
Cr	76.5665	59.6640	74.2247
S	17.6904	15.6173	17.2630
V	77.3399	50.6278	74.7867

Table 5: Mean intensities of the detected elements of samples 550, 625 and 689 based on EDXRF measurements with the M4 Tornado.

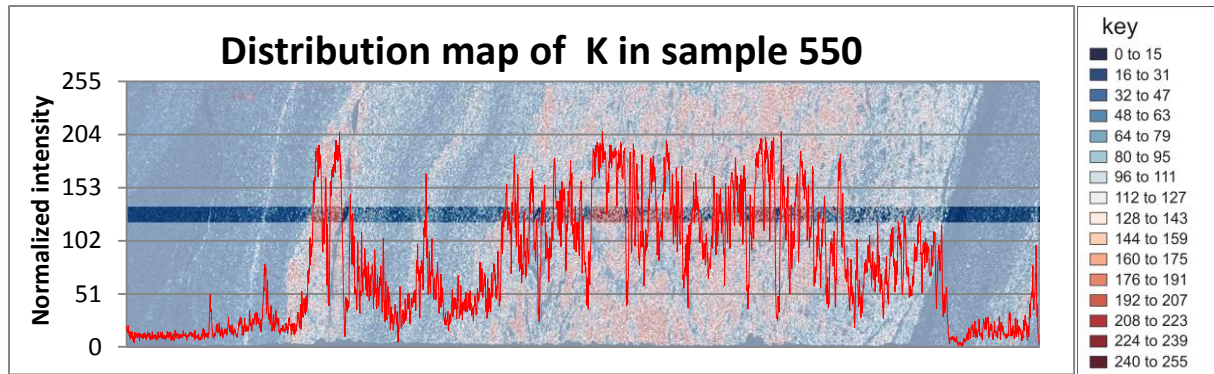


Figure 26: Distribution map of K in sample 550 with a graph showing the average intensity values of 51 horizontal profiles. The investigated band is the non-transparent area in the central part of the sample.

Caused by the high resolution of the EDXRF scan, the graph showing the result of the horizontal profiling is not as smooth as for the LIBS measurements. Nonetheless the graph follows the trend identified with the LIBS distribution map. The intensity of all elements has been normalized automatically by the Bruker software to 255 intensity values to allow a better comparability of elements.

For simplicity and a better comparability the results of the horizontal profiling of the elements Si, Al, Fe, Ca and K are displayed together in **Figure 27**. In order to enable an easier optical analysis, the graphs have been smoothed using the trendline option “Moving Average” with a period of 10 in Microsoft Excel. The smoothed results are displayed in **Figure 28**. A comparison of the two diagrams in **Figure 27** and **Figure 28** reveals an identical overall trend, proving that the mathematical simplification does not influence the validity of the results. This process has also been applied to sample 689, see **Figure 29**.

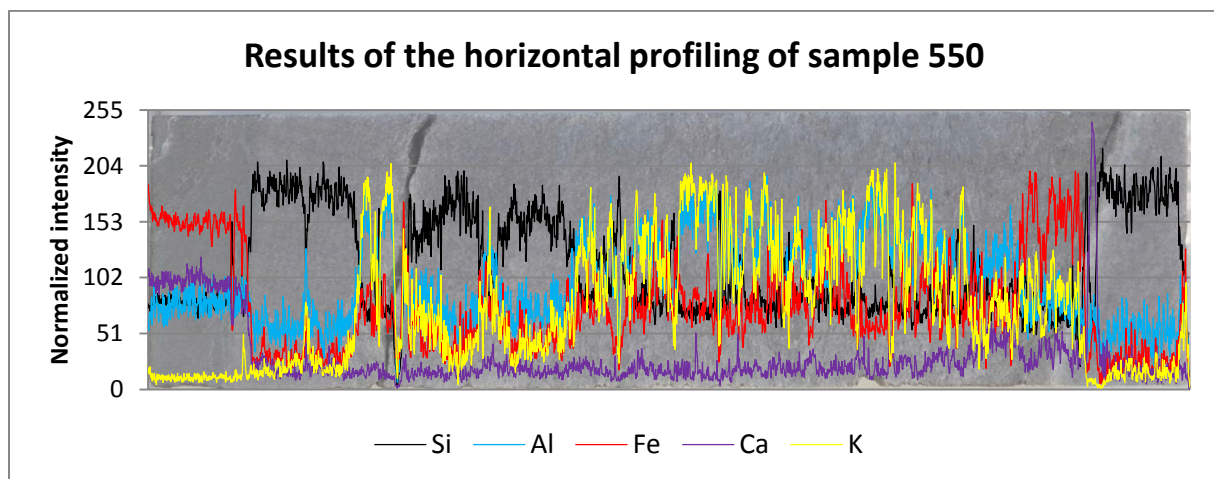


Figure 27: Results of the horizontal profiling on sample 550 including the elements Si, Al, Fe, Ca and K. In the background sample 550 is illustrated.

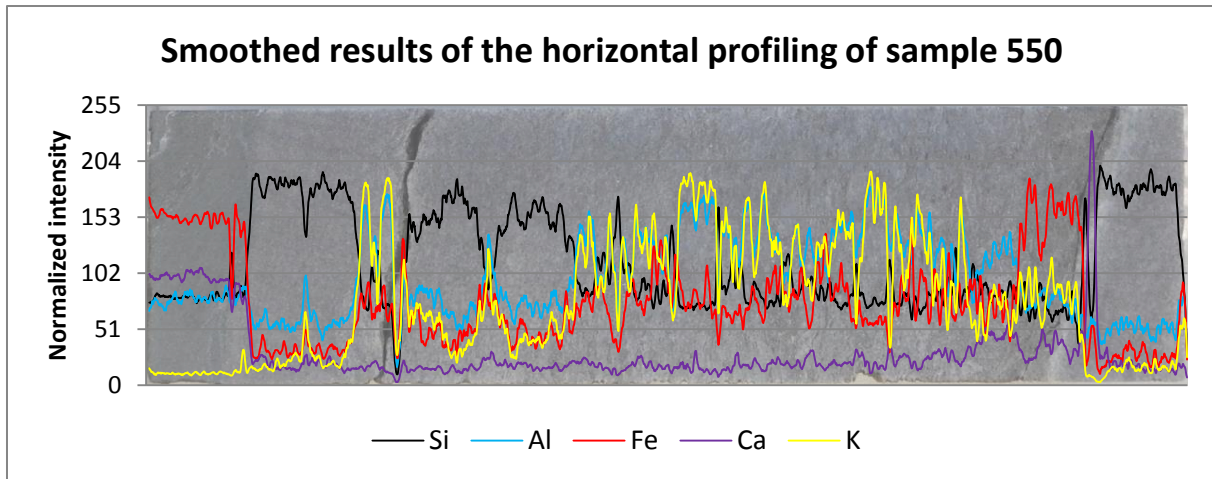


Figure 28: Horizontal profiling on sample 550 with smoothed values including the elements Si, Al, Fe, Ca and K. In the background sample 550 is illustrated.

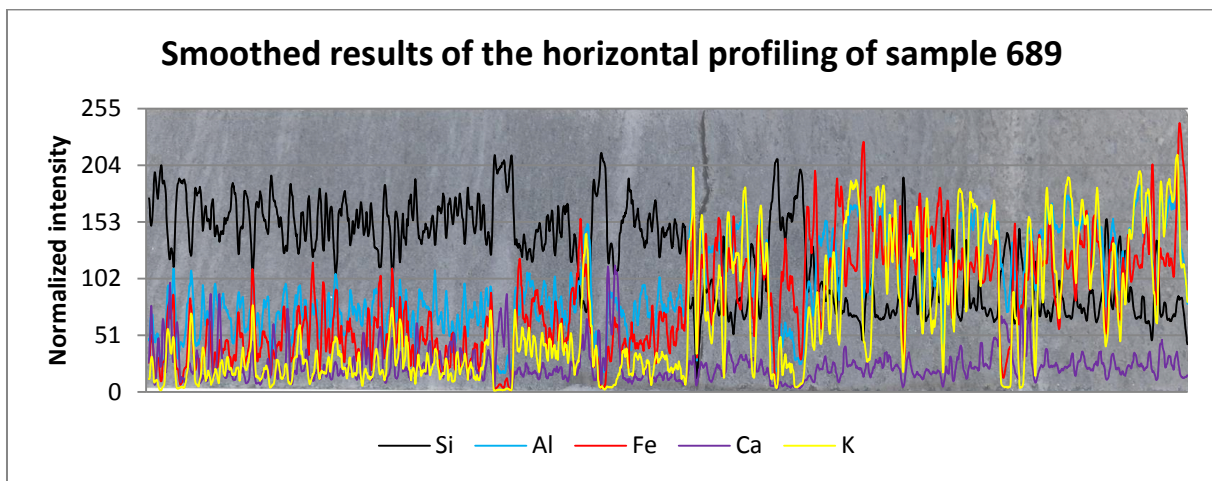


Figure 29: Horizontal profiling on sample 689 with smoothed values including the elements Si, Al, Fe, Ca and K. In the background sample 689 is illustrated.

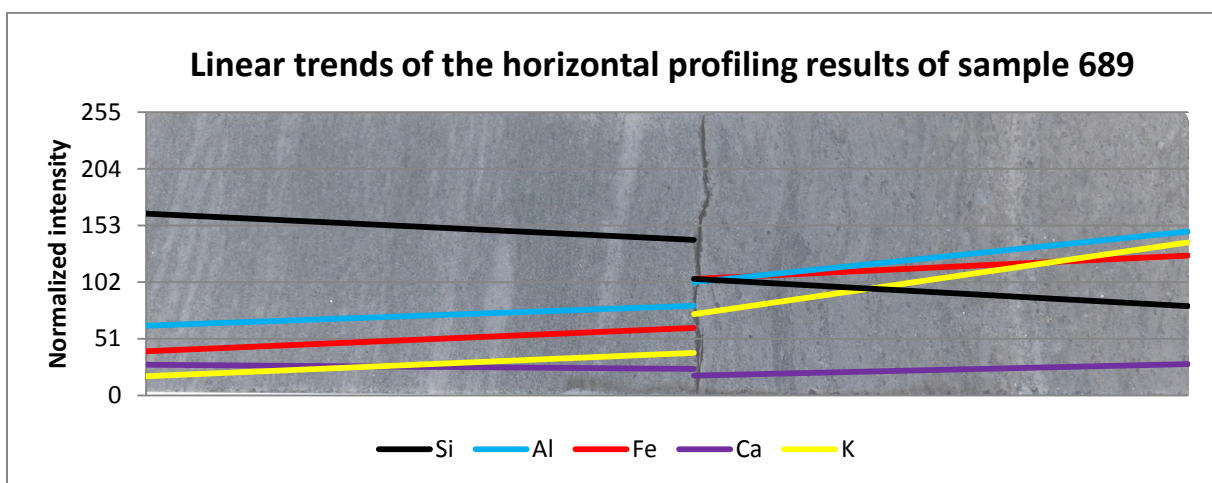


Figure 30: Linear trends of the elements Si, Al, Fe, Ca and K of the two varying rock section in sample 689. In the background sample 689 is illustrated.

According to the macroscopic description, sample 689 consists of two different rock types, a mylonitic gneiss with quartz lenses in the upper half of the core and a platy phyllonite with albite porphyroblasts in the lower half (**Figure 44** page 75). To illustrate how sharp the border between the two rocks is or if element transport between different lithologies can be traced, linear trend lines of the element intensities in the two different rocks have been calculated, as displayed in **Figure 30**. While Ca is near-consistent throughout the entire sample, all other major elements show a very sharp change along the boundary. In the upper half of the sample, the mylonitic gneiss, the Si intensity is higher than in the bottom half described as phyllonite. Conversely, the concentrations of the elements Al, Fe and K are lower in the gneissic region compared to the phyllonitic part.

6.4 EDXRF DATA OF THE AVAATECH CORE SCANNER

The measurements with the AVAATECH core scanner at the BGR in Berlin-Spandau were conducted with all selected core samples, see **Table 2**. The results are illustrated in the same way as the horizontal profiling of the EDXRF measurements with the M4 TORNADO or LIBS. In **Figure 31** the results of the measurements of the five index elements of sample 550 are displayed. The full data set is provided in the attachment under “*XRF results of the AVAATECH core scanner*”. Because of the variation in the intensities of the individual elements, only elements of similar intensities are put together in one group. The results of other element “groups” of similar measured intensity are attached in the appendix.

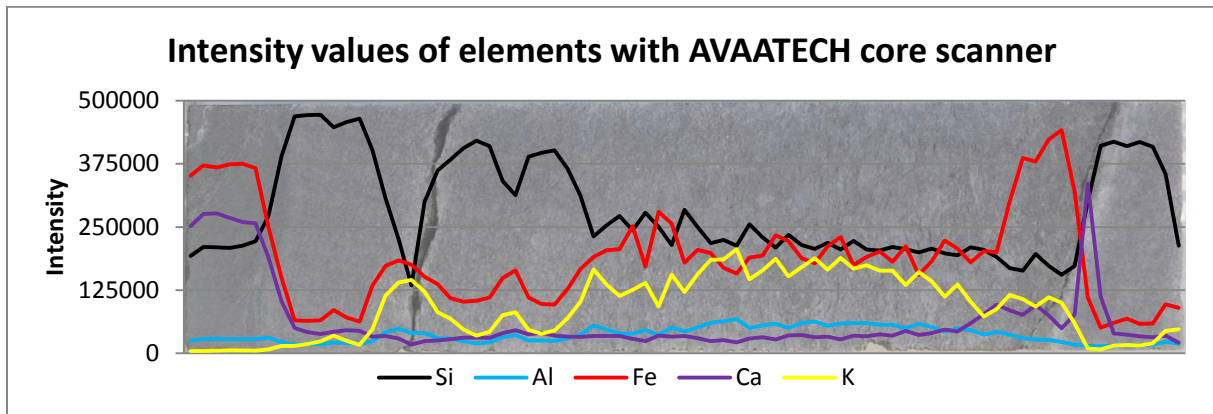


Figure 31: Intensity values of the elements Si, Al, Fe, Ca and K detected with the AVAATECH core scanner in sample 550. In the background sample 550 is illustrated.

By looking at the Si intensities, the lowest measured intensity is about 134,000 and the highest measured intensity is about 472,000. The areas of the highest measured intensities correlate to the regions where gneiss can be macroscopically identified. In these areas the intensities of all other detected elements are low. In the regions where amphibolites have been macroscopically identified, the Si intensities are the lowest and the intensities of Fe and Ca are high. The highest measured intensities of K were detected in the regions that have been assigned to phyllonites. In these areas the intensities of Si are lower while Fe intensities are above average. The macroscopically suspected calcite vein shows, as expected, the highest measured Ca intensity. Accordingly, the major element data obtained are in full agreement with the rock composition optically identified.

In **Figure 32** the results of the AVAATECH core scan for sample 689 are shown as before for the elements Si, K, Ca, Fe and Al.

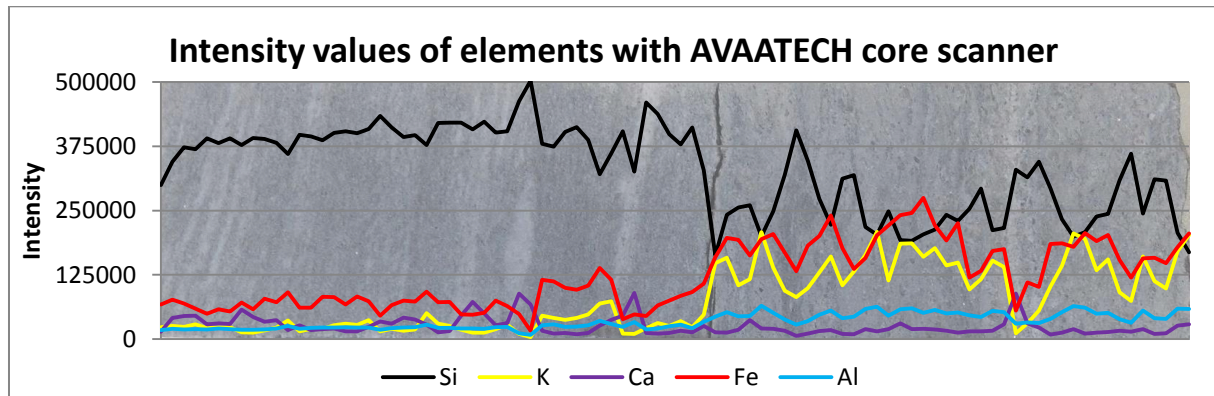


Figure 32: Intensity values of the elements Si, Al, Fe, Ca and K detected with the AVAATECH core scanner in sample 689. In the background sample 689 is illustrated.

The Si intensities on the leucocratic gneiss (left hand side in **Figure 32**) are with values reaching from roughly 300,000 to 500,000 consistently high, while on the right hand side in the figure the Si intensities vary from about 200,000 to 400,000. The highest Si intensity measured is 502,757 and was found in the area of a big quartzo-feldspatic vein. The intensities of the other elements are all low in the leucocratic region of the sample. On the right side of the sample the intensities of the elements Fe and K rise significantly higher than Al and Ca up to values of approximately 300,000. The Al intensities only show a slight increase beyond the rock boundary. Whenever high K intensities have been detected, the measured Si intensities were decreased and vice versa.

The results of the other five samples (578, 625, 641, 658 and 691) are very similar. Areas with high Si intensities (gneiss) show low intensities of other elements while K, Ca, Fe and Al is clearly enriched in the mica-rich phyllonites. The results of the other samples and a full list of data acquired are attached in the appendix.

6.5 HYPERSPECTRAL IMAGING

The samples 550, 625 and 689 were scanned as described in chapter 5.3 “*hyperspectral image analyses*”. The data were first processed using the standard mineral identification algorithm MICA (Kokaly, 2011) which has been well calibrated for sediment minerals (Koerting, et al., 2015) and a number of metamorphic minerals such as white mica, epidote and a few others. Additionally the data were processed using an algorithm to identify Fe and Fe-bearing minerals (Mielke, et al., 2014). In **Figure 33** the result of the hyperspectral mapping of sample 550 is displayed. The table to the left of the figure shows the classified mineral phases and their determined percentage. As already mentioned in the methodology a detection of the minerals quartz and feldspars is not possible with the hyperspectral cameras used. Hence, almost 80% of the sample remained unclassified using the results of the MICA algorithm while sedimentary minerals such as illite (that cannot be present in this sample) have been falsely identified.

Table 6: Results of the hyperspectral mapping on sample 550 using the algorithm MICA.

	Class Summary	Percent
	Not_classified	78.5411
	calcite	0.2383
	calcite+muscovite	0.0081
	calcite+montmorillonite_Ca	0.0202
	calcite+montmorillonite_Na	0.0646
	carbonate_Fe_bearing	4.0147
	epidote	8.8170
	chlorite+muscovite	0.1777
	muscovite_lowAl	0.1050
	muscovite_medAl	3.6027
	muscovite_medhighAl	0.4645
	illite	0.2625
	illite_gds4	0.0606
	kaolin+muscovite_mix_intimate	0.0040
	kaolin+calcite	0.0081
	pyrophyllite	0.0040
	buddingtonite	0.0202
	buddingtonite+montmorillonite	0.0040
	dry_veg_grass_2_3um	0.9855
	dry_veg_nongrass	1.5833
	dry_veg_nongrass_2_3um	1.0138



Figure 33: Classified minerals determined using MICA algorithm based on the hyperspectral data on sample 550.

Accordingly, these results have to be critically interpreted and calibration for minerals in typical rock forming metamorphic samples still has to be made. Nevertheless the results provide useful information on the mineralogy of the sample. In the area consisting of amphibolite, Fe-bearing carbonate and epidote were identified by the MICA algorithm. Epidote was identified and is certainly present as it is a common mineral in metamorphic rocks like amphibolites. A further correct identification was muscovite in three different stages of Al-content according to the MICA calibration. The regions correlate to those in which mica minerals were found microscopically and where high contents of K were measured with all devices.

Table 7: Results of the hyperspectral mapping on sample 625 using the algorithm MICA.

	Class Summary	Percent
	Not_classified	60.7948
	calcite	0.0086
	calcite+muscovite	0.0115
	calcite+montmorillonite_Ca	0.0230
	calcite+montmorillonite_Na	0.2214
	carbonate_Fe_bearing	0.1812
	epidote	5.6217
	chlorite+muscovite	0.2070
	muscovite_lowAl	0.1524
	muscovite_medAl	18.7859
	muscovite_medhighAl	2.1337
	muscovite_Fe-rich	0.0173
	illite	0.5291
	illite_gds4	0.0115
	kaolinite_pxl	0.0058
	dry_veg_grass_2_3um	1.6822
	dry_veg_nongrass	1.9784
	dry_veg_nongrass_2_3um	7.6346



Figure 34: Classified minerals after MICA algorithm based on the hyperspectral data on sample 625.

The areas classified as “*dry_veg_grass_2_3um*”, “*dry_veg_nongrass*” “*dry_veg_nongrass_2_3um*” can be attributed to the support on which the samples have been placed on. Since the figures have been cropped to only show the relevant sample sections, these support regions cannot be seen in **Figure 33**.

In sample 625 the percentage of unclassified regions is 60%. The most frequent mineral identified by MICA is muscovite in several variations with approximately 21%. Further the mineral epidote was measured with a percentage of 5.6%. Other mineral phases classified appear in trace amounts only.

Table 8: Results of the hyperspectral mapping on sample 689 using the algorithm MICA.

	Class Summary	Percent
	Not_classified	70.6635
	calcite_abundant	0.0064
	calcite	0.2821
	calcite+montmorillonite_Ca	0.8397
	calcite+montmorillonite_Na	0.1218
	carbonate_Fe_bearing	0.1122
	epidote	0.2564
	chlorite+muscovite	0.5096
	muscovite_lowAl	0.1827
	muscovite_medAl	2.4295
	muscovite_medhighAl	0.0096
	muscovite_Fe-rich	1.5385
	illite	14.7340
	illite_gds4	3.4936
	kaolinite_wxl	0.0032
	kaolin+calcite	0.0032
	montmorillonite_Na	0.0160
	buddingtonite	0.0064
	tremolite_or_talc	0.0032
	dry_veg_grass_2_3um	1.1474
	dry_veg_nongrass	0.6955
	dry_veg_nongrass_2_3um	2.9455



Figure 35: Classified minerals after MICA algorithm based on the hyperspectral data on sample 689.

In sample 689 approximately 70% of the investigated area remained unclassified applying MICA calculations, with the majority of unclassified regions situated in the leucocratic gneiss section. The most frequently classified mineral is illite with about 18%. According to Vinx (2015) Illite is a term for a series of clay minerals with a very similar structure to micas. It can occur authigenic and due to low-grade overprint of micas, feldspar and other silicates (Vinx, 2015). As the applied MICA algorithm is calibrated for sedimentary rocks, what was assigned as illite might correlate to chemically related mica minerals such as biotite and muscovite in the investigated metamorphic rock samples. The results of the EDXRF and LIBS scans show higher intensities of K and Al in these regions.

Other more frequently classified minerals in sample 689 were variations of muscovite and calcite.

Table 9: Results of the hyperspectral mapping on sample 550 using the algorithm for Fe and Fe-bearing minerals.

	Class Summary	Percent
	Not_Classified	44.1077
	epidote	0.3688
	chlorite_low_Fe	0.0281
	chlorite_high_Fe	0.8097
	Fe ²⁺ _Type_3	0.0241
	Fe ²⁺ _Type_4	9.9166
	Fe ²⁺ _Fe ³⁺ _Type_1	0.1122
	Fe ²⁺ _Fe ³⁺ _Type_2	1.5793
	Fe ²⁺ _Fe ³⁺ _Type_3	0.0080
	Fe ²⁺ _Fe ³⁺ _Type_4b	37.0290
	Fe ²⁺ _Fe ³⁺ _Type_4c	5.3952
	dry_veg_grass_2_3um	0.0401
	dry_veg_nongrass	0.0281
	dry_veg_nongrass_2_3um	0.5532



Figure 36: Classified Fe-bearing minerals based on the hyperspectral data on sample 550.

A classification for Fe and Fe-bearing minerals according to a new index termed “iron feature depth” (IFD) developed by (Mielke, et al., 2014) allows distinguishing the oxidation states of Fe in minerals. The distinction of Fe²⁺ and Fe³⁺ is particularly interesting for identifying mineral hydration and oxidizing processes caused by fluid migration (Mielke, et al., 2014). **Figure 36** shows the classification results on sample

550. In **Table 9** the legend shows results of the processing with various Fe-bearing minerals in different oxidation states and their relative percentage. The results of samples 625 can be found in **Table 10** and **Figure 37**, for sample 689 in **Table 11** and **Figure 38**. Compared to the classification with the MICA algorithm, the classification using Fe-bearing minerals is more successful when taking the overall percentage of classified minerals into account.

Table 10: Results of the hyperspectral mapping on sample 625 using the algorithm for Fe and Fe-bearing minerals.

	Class Summary	Percent
	Not_Classified	57.7121
	epidote	0.0518
	chlorite_high_Fe	1.6024
	Fe ²⁺ _Type_3	0.0274
	Fe ²⁺ _Type_4	2.0289
	Fe ²⁺ _Fe ³⁺ _Type_1	0.0183
	Fe ²⁺ _Fe ³⁺ _Type_2	4.0883
	Fe ²⁺ _Fe ³⁺ _Type_4a	0.0305
	Fe ²⁺ _Fe ³⁺ _Type_4b	19.1622
	Fe ²⁺ _Fe ³⁺ _Type_4c	11.2963
	dry_veg_grass_2_3um	0.1828
	dry_veg_nongrass	0.0061
	dry_veg_nongrass_2_3um	3.7928



Figure 37: Classified Fe-bearing minerals based on the hyperspectral data on sample 625.

Nevertheless, with 51% a considerable amount of the sample is still unclassified. Minerals that have been identified include epidote and chlorite, as well as different valences of Fe. Areas classified as “dry_veg_grass_2_3um”, “dry_veg_nongrass” or “dry_veg_nongrass_2_3um” are again caused by the underlayment on which the samples have been placed. The majority of minerals in all samples can be assigned to different types of “Fe²⁺_Fe³⁺” followed by different types of “Fe²⁺”. According to Vinx (2015)

chemical weathering under the presence of water leads to oxidation of Fe^{2+} to Fe^{3+} . This causes a destruction of minerals that mainly contain Fe^{2+} like biotite, olivine or pyroxene. Secondary iron minerals, e.g. goethite or ferrihydrite are also stable in a specific, more acidic pH range (Mielke, et al., 2014) that might be important for investigations on siliciclastic metamorphic rocks. Based on the distribution of the different Fe phases, transport movements of water or deformational directions might be possible to explain. Hence, a water-involved element transport and therefore a possible metasomatic process could be proved. In sample 689 (**Figure 38**) an alternation of primary and secondary iron phases occur in the lower part of the sample. This might be evidence for fluid involving element mobilization. However the alternation is orientated parallel to the deformational direction. Hence if fluid related processes have occurred, element transport was only possible along the horizontal shear planes.

Table 11: Results of the hyperspectral mapping on sample 689 using the algorithm for Fe and Fe-bearing minerals.

	Class Summary	Percent
	Not_Classified	52.5956
	kjarosite200	0.0032
	epidote	0.0063
	chlorite_low_Fe	0.0126
	chlorite_high_Fe	0.2300
	Fe^{2+} _Type_3	0.6017
	Fe^{2+} _Type_4	12.4961
	Fe^{2+} _Fe $^{3+}$ _Type_1	0.6237
	Fe^{2+} _Fe $^{3+}$ _Type_2	9.4091
	Fe^{2+} _Fe $^{3+}$ _Type_3	0.0063
	Fe^{2+} _Fe $^{3+}$ _Type_4b	2.5358
	Fe^{2+} _Fe $^{3+}$ _Type_4c	19.4733
	dry_veg_grass_2_3um	0.1890
	dry_veg_nongrass	0.0032
	dry_veg_nongrass_2_3um	1.8144



Figure 38: Classified Fe-bearing minerals based on the hyperspectral data on sample 689.

7 INTERPRETATION

7.1 MINERAL MAPPING USING LIBS DATA

Based on the intensity distribution common rock-forming minerals have been classified to generate a mineral map of the measured sample surfaces. At first the distribution of quartz was characterized using the highest intensities of Si measured in the regions without other element peaks such as Al, Fe, and alkali-elements. The next mineral classified was albite, based on high intensities of sodium and very small intensities of K. K-feldspar was classified based on high intensity K, absence of Fe and low sodium. To show the occurrence of the mineral muscovite, regions of high K and Al intensities and no Fe or Mg intensities were used. Biotite has been correlated with high intensities of Fe, K and Mg. In addition to biotite other minerals also contain high intensities of Fe, K and Mg including most of the common amphibole minerals. Accordingly, amphibole was identified using biotite features combined with elevated Ca levels. The distribution of pyrite was illustrated by merging regions with high contents of Fe and sulfur. Calcite is categorized in regions with a very high intensity of Ca but no other element shown. Apatite was recognized by high intensities of Ca and phosphorous and titanite by high intensities of titanium and Ca.

After classification of the minerals, the samples 550, 625 and 689 have been compared to examine differences in their mineralogy. For more detailed investigations the three samples were divided into sections of similar mineralogy. **Figure 39** to **Figure 41** show the mineralogical composition of the samples 550, 625 and 689 as well as their separated sections. From the mineral assemblage the rock petrology was derived. Already macroscopically the samples show different types of rocks. Including the results of the mineral mapping, a separation was made, as illustrated in

Figure 39 on the example of sample 550.

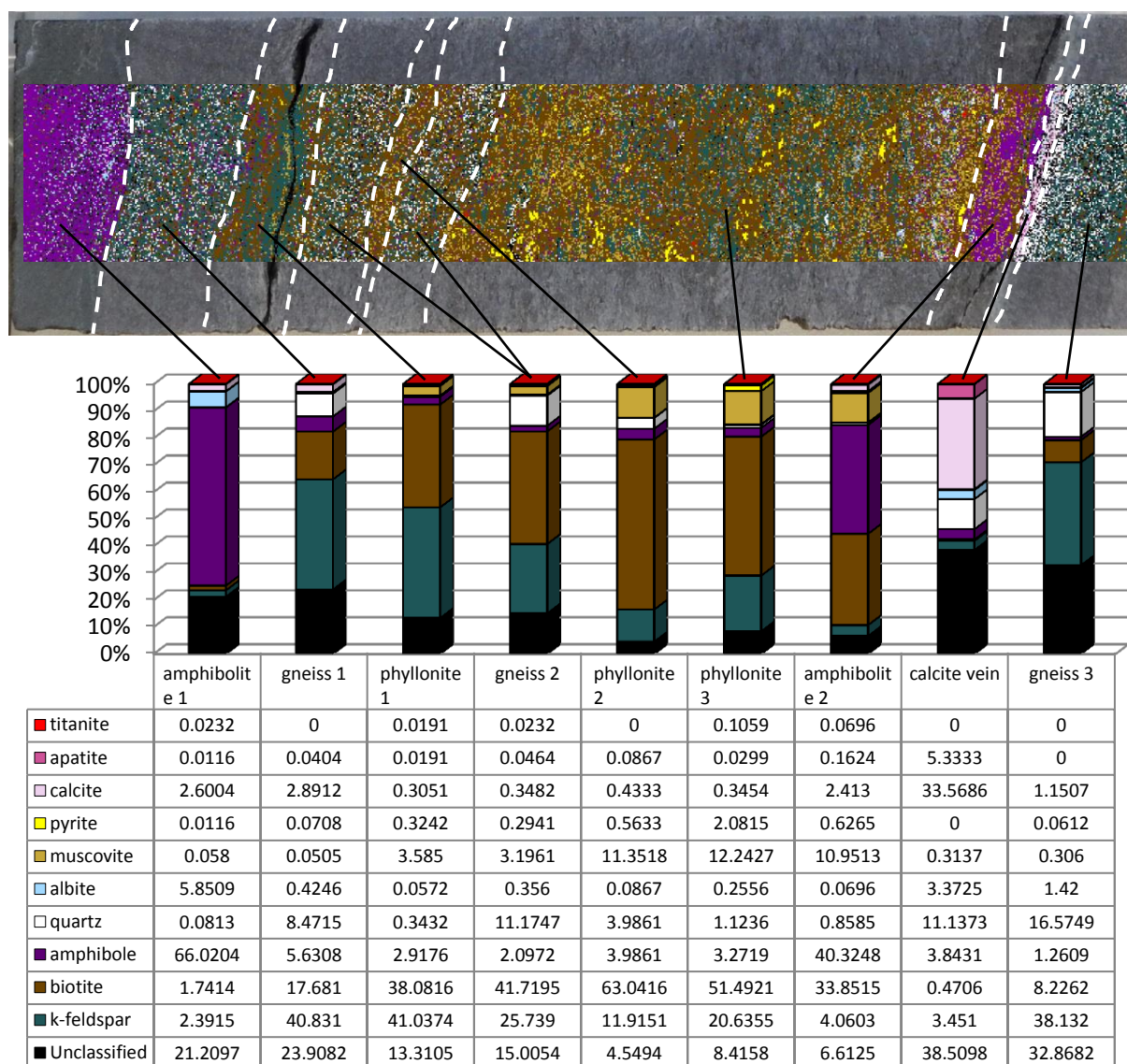


Figure 39: Mineral distribution map classified on LIBS data. Sample 550 with separate sections and the mineralogical composition in percentage, also shown in a data table.

Macroscopically visible in sample 550 is a mafic rock in the upper part (left part of **Figure 39**). Resultant from the EDXRF and LIBS analysis this area shows high contents of Fe and Mg. According to Vinx (2015) mafic minerals contain mainly the chemical components Fe and Mg or their geochemical representatives. When the visible color is dark to black, Fe is the major element of the mutual convertible elements Fe and Mg. A typical representative of mafic minerals is amphibole. This mineral is most common in amphibolite facies mafic rocks such as amphibolites (Vinx, 2015). Based on the element distribution generated by LIBS data, the macroscopic assignment of amphibolites can therefore be further supported.

Next to amphibolites other rocks have been classified. For example the areas classified as gneiss showed a high content of quartz and K-feldspar. The gneissic regions in sample 550 alternate with phyllonite. According to Vinx (2015) phyllonites are described as phyllosilicate-rich mylonites. The areas classified as phyllonites showed in the EDXRF and LIBS data very high intensities of K and higher intensities of Al when compared to the remaining regions. According to Vinx (2015) the essential elements in the interlayers of muscovite are K and Al and of biotite additionally Fe, Mg and Ti. Micas such as muscovite or biotite are one of the most important groups of rock-forming minerals. Alongside magmatic rocks they are especially common in metamorphic rocks. According to the mineral classification based on the LIBS data the mica minerals biotite and muscovite were enriched in phyllonites. The enrichment was further supported by microscopic investigations.

In sample 550 an area with very high calcite content was measured. This white vein-like area is directly located at a crack. Calcite can occur as hydrothermal vein fills in metamorphic rocks (Vinx, 2015). Consequently a calcite vein as classified adjacent to an already macroscopically visible crack formed by hydrothermal activities is plausible.

In comparison to the samples 625 and 689, in sample 550 almost no albites occur.

After macroscopic investigations sample 625 can be described as migmatitic gneiss (Vinx, 2015). More homogenous parts with fine grain size (Markl, 2015) occur next to very heterogeneous parts of middle coarse grain size (Markl, 2015) and complex deformational structures. In the inhomogeneous areas big leucocratic parts sometimes occurring in veins are present, according to Vinx (2015) described as leucosome. The leucosome (usually quartz and feldspar) is interpreted as crystallized partial anatexic melt (Vinx, 2015). The still largely unchanged protoliths in migmatites are called paleosome (Vinx, 2015). In sample 625 the homogenous, fine-grained gneisses are interpreted as such. The other more heterogeneous parts that faced partial melting are called neosome (Vinx, 2015). Consequently sample 625 has been divided into the sections paleosome and neosome 1 and 2.

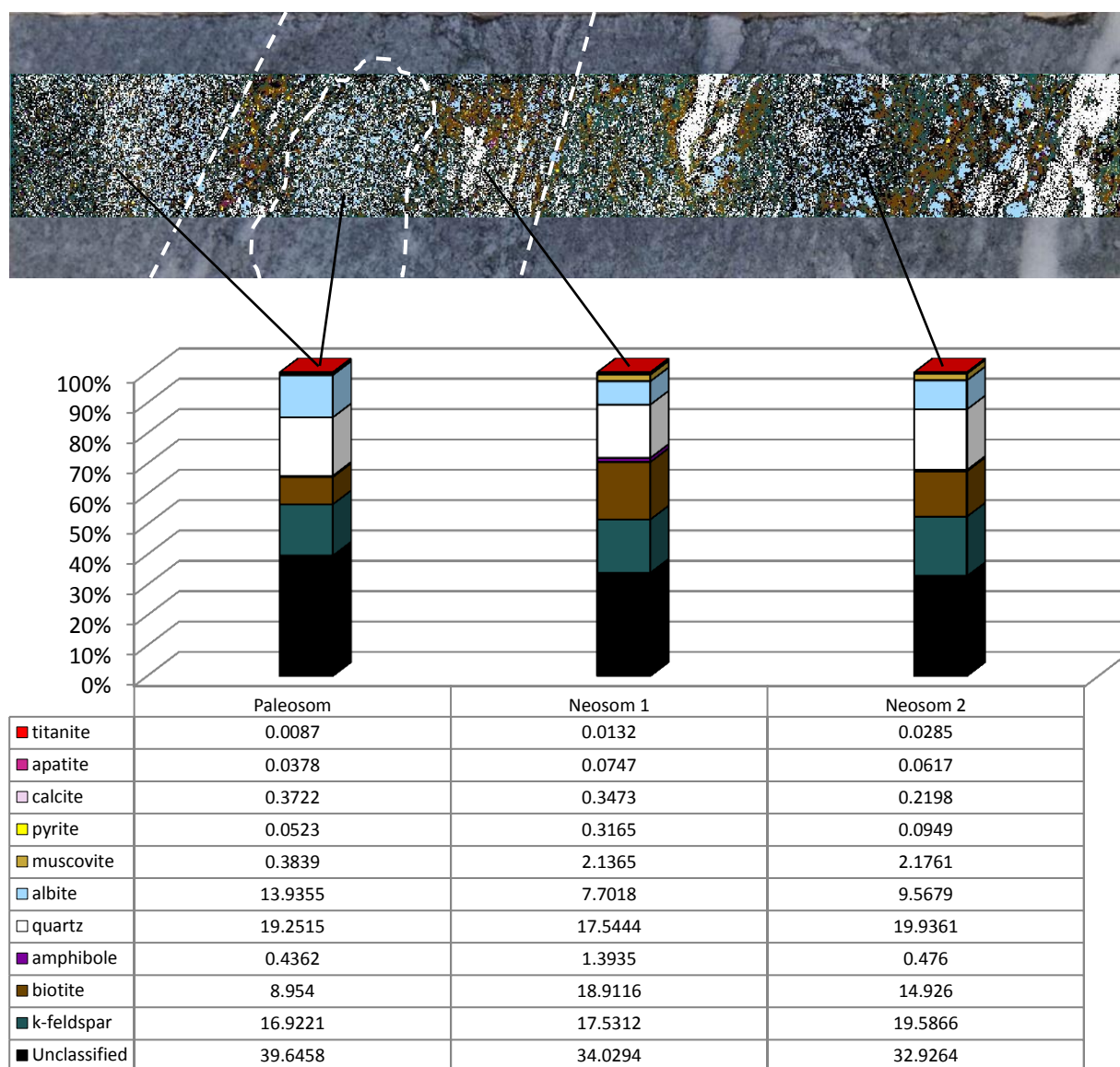


Figure 40: Mineral distribution map classified on LIBS data. Sample 625 with separate sections and the mineralogical composition in percentage, also shown in a data table.

In general the minerals classified most frequently were quartz, feldspar and biotite. According to the mineralogical classification, the composition of sample 625 differs from sample 550. The average quartz content in sample 625 is much higher than in sample 550. The content of micas is lower than on sample 550 as a phyllonitic part of several centimeters thickness is not present. However biotites occur in some neosome for example as reaction rims surrounding quartz veins. In general, the mineralogical composition of all differentiated lithologies in sample 625 is very similar. This leads to the conclusion that neosome and paleosome have the same protolith. Only the grain size and the concentration of the minerals in the neosome show differences. For instance, in the neosome albite porphyroblasts of up to 4 mm diameter occur.

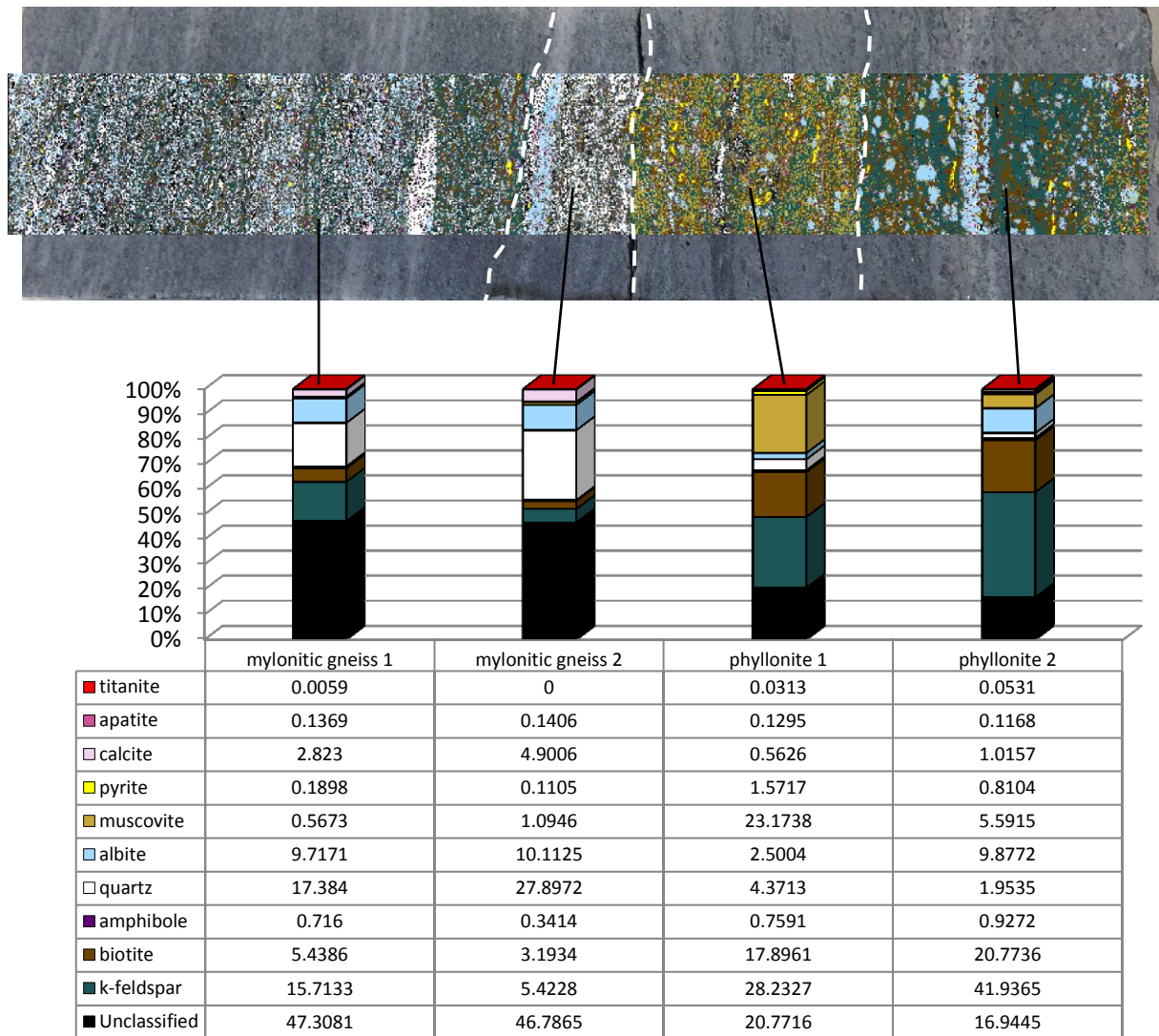


Figure 41: Mineral distribution map classified on LIBS data. Sample 689 with separate sections and the mineralogical composition in percentage, also shown in a data table.

Due to the mineral classification based on the LIBS data, sample 689 was separated into four rock sections with different mineral composition. On the upper half of the core piece (left hand in **Figure 41**) a gneiss similar to the gneiss labeled “paleosome” in sample 625 was found. Both paleosome gneisses share features such as small grain size and similar mineral composition. Distinguished from the gneiss in sample 625, the leucocratic gneiss (sample 689) is banded with alternations of mafic and felsic parts. The mylonitic gneiss 2 differs slightly from mylonitic gneiss 1 as the quartz content is 10% higher than mylonitic gneiss 1 and there is a calcite vein increasing the calcite amount up to almost 5%. In addition to the calcite vein an albite accumulation is located in the same area. However the amount of albite classified in both mylonitic gneiss sections is almost equal. The amount of K-feldspar is 10% lower than in the mylonitic gneiss 1. The lower half of sample 689 (right half of **Figure 41**) is categorized as phyllonite 1 and 2

showing significant differences to the upper half of sample 689. First of all, the assignment of the two phyllonite regions was more successful, with only 20% and 17% remaining unclassified. A possible explanation is discussed in the chapter "Error Discussion". Furthermore, the amount of quartz in the phyllonite is much less than in the mylonitic gneiss. In accordance to the characterization as phyllonite, the region is richer in biotite and muscovite. Interesting is the higher content of K-feldspar in the right half compared to the left half of **Figure 41**. With an amount of 42% K-feldspar is the most frequently classified mineral in the phyllonite 2. Based on the EDXRF element distribution maps the complete lower half of the core was presumed mineralogically equal. However, according to the mineral classification based on the LIBS dataset, this lower half of the core is very in-homogeneous and is therefore separated into two different phyllonites. Phyllonite 1 consists of more muscovite than phyllonite 2. The latter has a higher percentage of K-feldspar and albite. These albites occur predominantly as large mineral porphyroblasts of several millimeters size. Although the amount of pyrite might be not as high with a percentage of approximately 1.6 and 0.8 in the right core half, the occurrence of this iron sulfide in occasional spots is visible in the mineral classification map (**Figure 41**).

7.1.1 ERROR DISCUSSION

“Gross errors” are caused by mistakes made by the scientist, e.g. incorrect documentation of data or the usage of incorrect units. “Systematical errors” occur due to incorrectly calibrated instruments or similar. In this case repetition of measurements will always show the same errors. Additionally, “random errors” can occur, e.g. due to parallax or objective errors (fluctuations). These errors occur within a statistical range. (Schenk & Kremer, 2014)

XRF, LIBS and Hyperspectral measurements have not been performed in the course of this study with purpose to gain quantitative measurements of element contents. Hence, none of the data sets have been calibrated and only a semi-quantitative approach has been taken. Therefore, further error discussions of measurements of intensities on these data are not considered further.

The mineral mapping based on LIBS data developed here has been verified by spot-check with a binocular. Nevertheless uncertainties and misinterpretations remain due to the fact that each laser beam spot may cover not only a single mineral but also borders and transition that give mixed analyses. Additionally unidentified minerals such as epidote, chlorite or accessories such as zircon or magnetite occur but could not be separated clearly due to intergrowth or small size of the grains or due to similar chemistry of classified minerals. Hence up to 47% measured sample surface remained unclassified. Especially in the areas with small grain sizes the percentage of unclassified minerals is large. Smaller grain sizes make it particularly difficult to avoid the detection of mineral borders or transitions. Some minerals like titanite or apatite however can be detected due to very high intensities measured even with very small grain sizes. Therefore, the main error type for the mineral classification based on the LIBS data is systematical. The LIBS instrument, build by LTB is still a prototype with not documented stability. Furthermore, the mineral classification is biased due to personal interpretation. Further, the resolution limitation of the device leads to mixed analyses along grain boundaries and causes therefore systematical errors. Finally the natural given variation of mineral chemistry make a clear mineral classification impossible.

Next to the mineral classification based on the LIBS data also the other methods contain possible sources of errors. The MICA used for the hyperspectral data is calibrated

predominantly for use on sedimentary minerals (Koerting, et al., 2015). Hence misinterpretations of “classified” minerals are likely and thus the results have to be treated carefully.

The data are listed with four post point decimal places without shortening as they were produced by instruments and software. The results are presented with this high accuracy to detect even accessory mineral phases such as titanite, apatite and zircon.

However, despite the measurements have not been calibrated and only a semi-quantitative approach has been taken, the results show very clear differences between the lithologies even on the microscale. Structural differences as well as mineral distribution, size and accumulation could be highlighted.

7.2 STRUCTURAL INTERPRETATION USING EDXRF DATA AND MICROSCOPIC INVESTIGATIONS

The element maps acquired in this study give a very clear structural overview of the rock sequences in the Lower Seve Nappe. The macroscopic inspection and the initial core description of the entire core section of the COSC-1 core imply a horizontally directed deformation almost orthogonal to the drilling. This confirms the previous understanding and interpretation of the nappe emplacement and demonstrates the deformational processes.

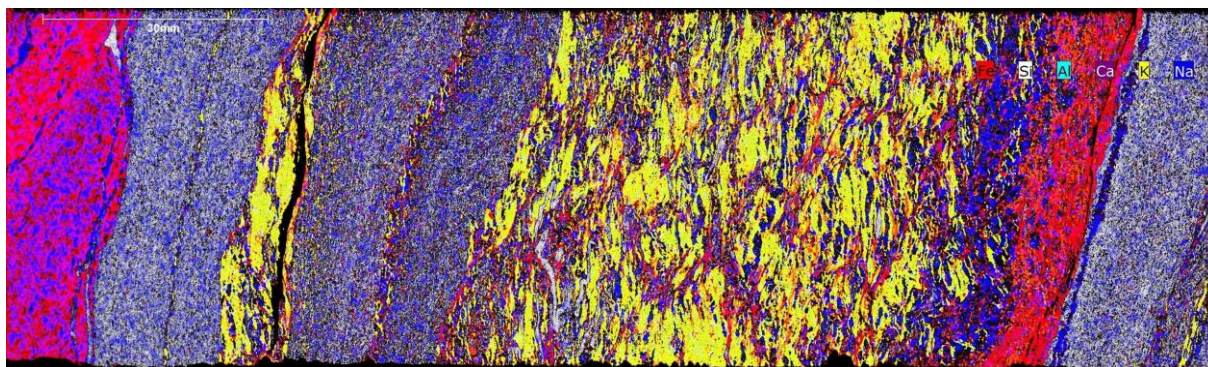


Figure 42: Element Distribution map of Si, Fe, Al, Ca, K and Na in sample 550, showing the schistosity of the mica-rich parts (yellow).

As noticeable in **Figure 42** the mica-rich parts classified although their high K intensity (here yellow) exhibits schistosity orthogonal to the drilling direction. According to Markl (2015) this schistosity in metamorphic gneisses is often related to the different temperature behaviors of biotite at the degradation of rocks in greater depth. Biotite and other phyllosilicates often tend to recrystallize sideways under high differential stress at enhanced p-t-conditions. The schistosity corresponds to the direction of the maximum tectonic shear strength. Other minerals like quartz or feldspars show a more granular structure and therefore don't display the direction of tectonic movements obviously.

Optical and the binocular inspection indicate this schistosity as well as directed deformation is indicated but the element maps as in **Figure 42** show it very pronounced. In samples 578, 641, 658 and 689 similar phyllonitic areas were identified (see last page), all showing schistosity orthogonal to the drill direction.

Cracks along the core are all orientated parallel to the foliation. This further supports the theory of directional deformation, as cracks will mostly form on weak zones, e.g. planes of schistosity (Vinx, 2015).

Porphyroclastic garnets occur in several samples in the COSC core and increase in quantity with increasing depth. Porphyroclasts are crystals that are bigger in size than the surrounding matrix (Vinx, 2015).

Especially the porphyroclastic garnets with sizes of up to several millimeter exhibit pressure shadows parallel to the foliation. Pressure shadows are accumulated areas of fine-grained material from matrix minerals or the clast itself. The orientation is symmetrical to two sides wedge-like in the foliation plain.

Figure 43 shows a photo of a garnet crystal with the described pressure shadows. Pressure shadows imply a dynamic recrystallization during regional metamorphism and underline the protracted history (Gee, et al., 2008). The porphyroblastic albites in sample 689 (**Figure 44**) are additional examples.

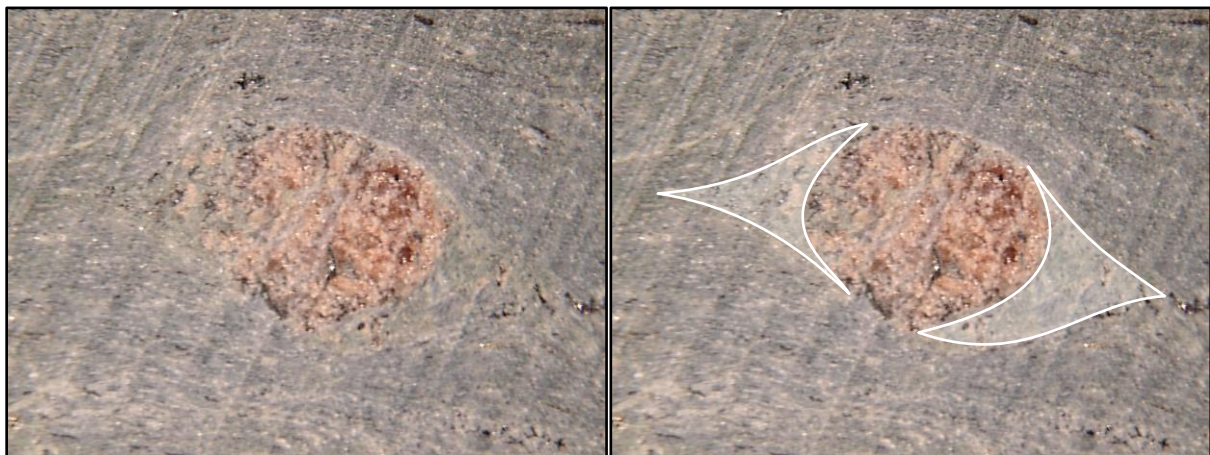


Figure 43: Garnet with so-called pressure shadows (traced with transparent white) to the right and left of the crystal in sample 691. The size of the garnet is approximately 4 mm.

According to (Grimmer, et al., 2015) P-T calculations provide evidence of eclogite facies metamorphism for the Upper and Middle Seve Nappe with pressure conditions ranging from 17.5 to 11 kbar and temperature conditions of $\sim 670 \pm 50$ °C. These conditions allow a garnet growth (Grimmer, et al., 2015) as they were identified in the COSC-1 core in the lower part of the Lower Seve Nappe.

Besides to mica-rich phyllonites also a majority of leucocratic gneisses show a platy, fine-grained, strongly parallel and very stretched out texture. For example sample 689 (**Figure 44**), shows such strong mylonitic quartz recrystallization (Oliot, et al., 2014). According to the mineral classification based on the LIBS data and macroscopic investigations, these mylonitic gneisses consist of grey areas with high contents of K-feldspar, albites and minor quantities of biotite, alternating with bright areas consisting of quartz. The orientation of the strongly deformed mylonitic gneiss is identical to the flaky phyllonites found in sample 550. Leucocratic quartz bands are very elongated and also show lenticular accumulations typical in quartzo-feldspathic mylonites (Vinx, 2015). Similar mylonites have been found by Oliot et al. (2014) during investigations in the Gotthard Massif. The ductile deformation of quartz starts at temperatures of approximately 300°C in greenschist facies conditions (Heitzmann, 1985). According to (Gilotti, 1989) the mylonitic zone at the base of the Särvi Nappe (located underneath the Seve Nappe) contains evidence of syntectonic greenschist facies metamorphism. Here also metamorphosed basaltic dikes similar to the amphibolites found in the samples of this study occur. However rocks found in the Lower Seve Nappe implement metamorphic conditions more typical for an amphibolite facies (Vinx, 2015). Also the mylonites studied in the Gotthard Massif (Oliot, et al., 2014) have been metamorphosed under amphibolite facies conditions.

Sample 625 (see last page) is a gneiss with marble cake-like deformation features that typically occurs in metatexitic (partially melted) gneisses (Markl, 2015).

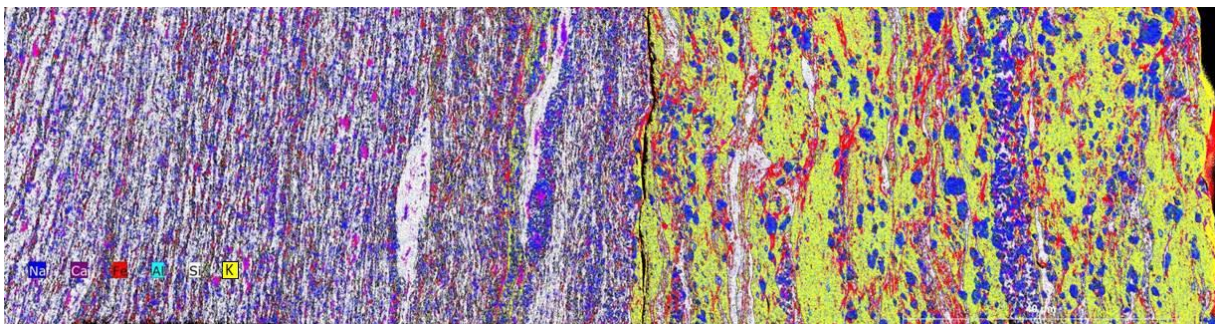


Figure 44: Element distribution map of Si, Fe, Al, Ca, K and Na in sample 689, showing the parallel stretched out texture of the leucocratic gneiss in the left half of the figure and albite porphyroclasts to the right.

To sum up, the data gained in this study serve very well to elucidate structural features clearly and to provide critical information on metamorphic petrology such as porphyroblastic syn-metamorphic growth and deformation.

7.3 COMPARISON OF CORE SCANNING METHODS

A comparison of XRF-measurements acquired by the Tornado instrument, the AVAATECH line point measurements, the LIBS-maps and the HySpex data was one of the major goals of this study in order to provide guidelines for future core investigations. Therefore the devices used have been evaluated in terms of speed, accuracy, detectable elements, sample size and resolution.

One initial advantage of the LIBS technique over other methods is the minimal sample preparation. Drill cores only have to be cut roughly and don't need to be polished. Areas of up to a size of 25 x 1000 mm (Rammlmair & Maima, 2014) can be investigated. This detection length of up to one meter is ideal for core pieces, while the small width of 25 mm is a limitation. Perhaps the biggest advantage of LIBS is that light elements from H to Na can be detected in high precision that cannot be acquired with any XRF tool. Li, Be, B, C and F that play major roles in geochemistry (White, 2005) can be investigated with this instrument. Disadvantages are the relatively long working time of 14 min/cm² and that the prototype LIBS core scanner used at the BGR can only be focused down to 100 µm (for this study 200 µm were used) (Rammlmair & Maima, 2014). The TORNADO M4 EDXRF core scanner has a big advantage in comparison to the LIBS-scanner due to its very high resolution down to 15 µm (TORNADO-brochure, 2015). With a maximum detection area of 160 mm to 200 mm, the maximum length of a sample needs to be shorter than for the LIBS core scanner, in which the maximum possible width allowed a complete analysis of the investigated core samples. Since the analyzed core samples 550, 625 and 689 had a maximum length of 192 mm the EDXRF core scanner was well suited to record the entire analyzable area. However, a full core section of one meter could not be detected. Depending on the resolution the average time for scanning with the EDXRF device totals to 22 min/cm², but very fast scans of 1 min/cm² can provide overviews with a poorer resolution (Rammlmair & Maima, 2014). Disadvantages are and that heavy elements appear in higher concentrations than in reality because they fluoresce more strongly from the depths. Crystal lattice diffraction is compensated by using two orthogonal positioned detectors. Grain boundaries not perpendicular to the sample surface provide mixed mineral compositions difficult to interpret.

The biggest advantage of the AVAATECH core scanner is the very fast detection. Within 26 minutes the complete sample 550 was analyzed with a step size of 2 mm,

corresponding to a speed of approximately 2 min/cm. The results are very similar to the horizontal profile results of the M4 TORNADO EDXRF measurements. However the resolution was much lower compared to the EDXRF CS Tornado M4 by Bruker and the line scan did neither provide element distribution nor mineral maps. As the AVAATECH CS has a X-Y table included, a measurement in two directions is possible. However a complete mapping is not possible and diffraction caused by crystal lattice cannot be compensated as with the Tornado CS, because only one detector is in use. Additionally point analysis can provide information of single spots or minerals, but an exact positioning of the X-ray is very difficult to achieve. However, as shown in this study, in metamorphic rocks semi-quantitative line scan analysis provide excellent results that are comparable to Tornado detailed mapping (**Figure 45** and **Figure 46**). Using the AVAATECH CS line scans on metamorphic rocks is useful, fast and produces oversight data in similar quality as the other tools but has limitations in terms of mapping.

The hyperspectral camera was the fastest scanning instrument producing a map of a whole sample with measurement time for the three samples 550, 625 and 689 of approximately 6 minutes. After the scanning procedure the data have to be post-processed, which takes additional 10 minutes time (personal com. F. Körting) and the following classification with the algorithm MICA requires additional 2 hours. However, the algorithms available currently to classify hyperspectral data are calibrated for a still limited number of minerals mostly from sedimentary rocks and are currently not suitable without several limitations for metamorphic mineral assemblages, e.g. the identification of quartz and feldspar is not possible with the used hyperspectral cameras. A detection of these minerals can be achieved using mid-wavelength infrared cameras (TERRACORE-brochure, 2016). Hence, the results of the hyperspectral measurements have to be interpreted with caution.

The results of the horizontal profiling of the EDXRF and the LIBS scans, as well as the results of the line scan of the AVAATECH core scanner are compared in **Figure 45**. It shows the K intensities in sample 550. Since all devices result in intensity variations of different magnitude and scale, the values have been normalized based on the maximum values set as 100 to achieve comparability. In addition, the results for the Al intensities of sample 550 from all three devices are displayed in **Figure 46**. The comparison diagrams of other elements and of sample 689 can be found in the appendix.

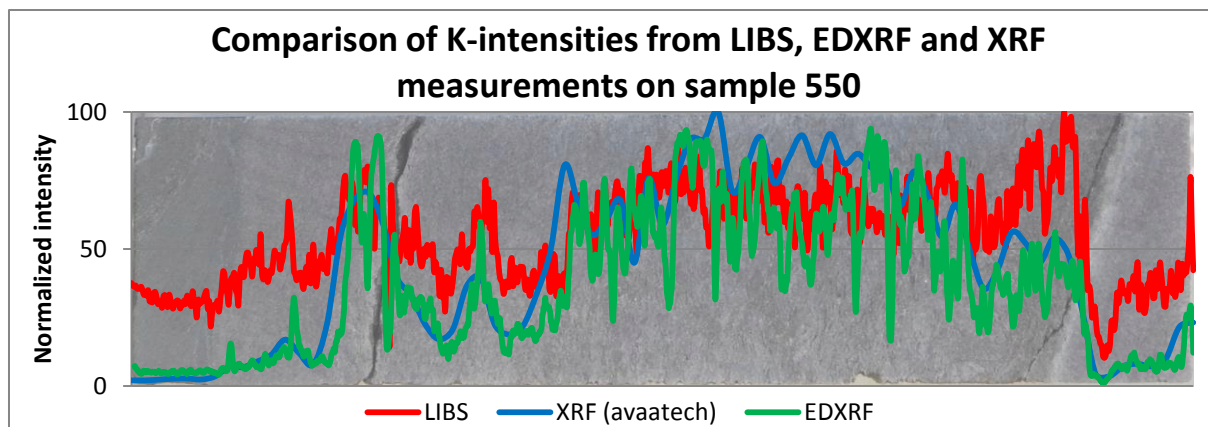


Figure 45: Comparison of the K-intensities obtained by LIBS, EDXRF and XRF on sample 550.

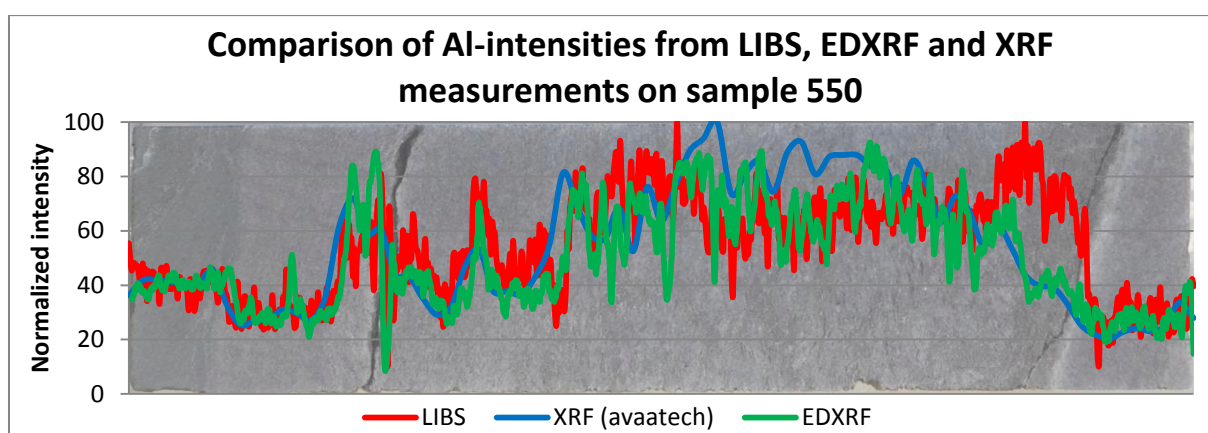


Figure 46: Comparison of the Al-intensities obtained by LIBS, EDXRF and XRF on sample 550.

In general the results of all devices are very similar. Whenever small or high intensities have been measured, they have been measured with all three methods. The only bigger variations exist between the data of the XRF and the LIBS method. The graph representing the results of the Avaatech core scanner follows almost perfectly the results of the EDXRF scan. The only noticeable difference is the density of the data. The EDXRF results are displayed as the average of 51 parallel profile lines and with the trend function of a moving average of 10 values. However, the graph is still much more detailed than the results of the AVAATECH core scanner. The variations in the results from the LIBS measurements to the XRF results might be due to the different underlying physical phenomena of the analyzing techniques. As detailed before, some elements can be detected more precisely with the LIBS technique, because elements lighter than Mg usually led to trouble with an X-ray fluorescence that is too low for the detector to analyze. For an identification of phyllonites in the analyzed Seve Nappe samples, the most detailed results can be achieved using the EDXRF M4-Tornado. The resolution is very high and therefore a very detailed depiction of microstructures and element

distributions can be achieved. The big advance of LIBS is the possibility to detect light elements such as Li or Na that cannot be detected with XRF methods. This is particularly important for investigations of light elements like Li to highlight possible element mobility in samples (White, 2005).

The investigation of core samples from the Seve Nappe with the EDXRF scanner AVAATECH delivered very convincing results for line scans. However, this was possibly due to the parallel orientation of the different lithologic units almost orthogonal to the drill direction. Whenever a different orientation of rock lithologies exists, an analysis with a line scanning device such as the Avaatech core scanner should take the orientation into account.

Comparing the results of the LIBS, the EDXRF and the Avaatech XRF with the results of the hyperspectral imaging, the areas classified as muscovite and illite are the areas where high intensities of K as well as lower intensities of Si were measured. The areas classified as Fe-bearing carbonate and epidote in sample 550 show very high intensities of Fe and Mg and low intensities of Si, as displayed in **Figure 47**. Here the EDXRF results of the Avaatech core scanner are laid over the mineral classification map of the hyperspectral analysis on sample 550. The identification of phyllosilicate-rich mylonites by the hyperspectral camera is poor and by far not as accurate as the scanning methods EDXRF or LIBS. Many of the mica-rich areas classified by microscopic investigations and EDXRF and LIBS analysis were not classified as such with the hyperspectral analysis. However, if a calibration of the hyperspectral data on metamorphic rocks is achieved and quartz and feldspars are detected by the cameras, this scanning method is promising for future projects.

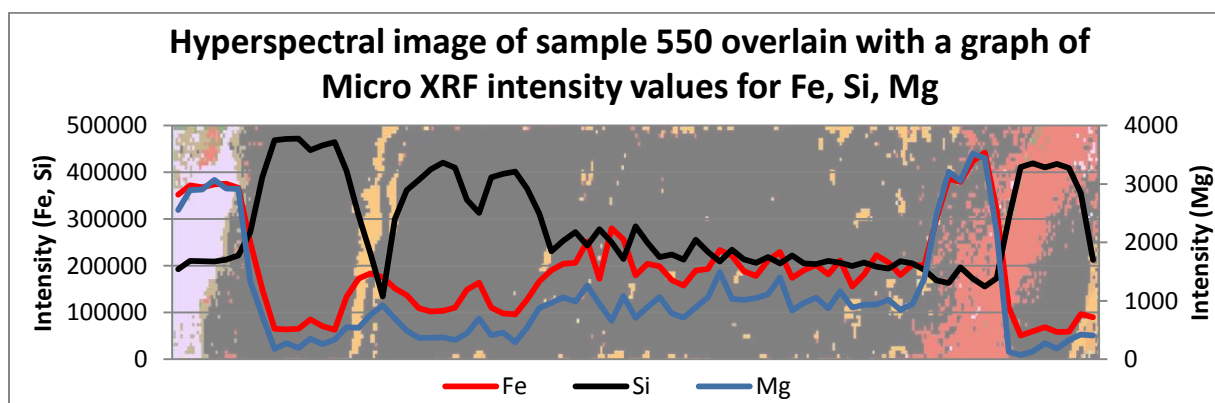


Figure 47: Comparison of the hyperspectral data with the EDXRF results of the Avaatech core scanner.

7.4 COMPARISON TO THIN SECTION MICROSCOPY

Thin sections can usually only be applied very selectively and therefore can only provide information on limited areas. In addition, they do not provide statistically relevant data except for point counting studies on a small area. Further, sample preparation requires a long time and can only be conducted by trained professional staff. In comparison the sample preparation for the devices used in this study requires only longitudinal cutting and for the μ -EDXRF measurements additional slight polishing. Also the analyses with the used scanning tools are all nondestructive to almost nondestructive (LIBS), while sample preparation for thin sections is destructive in form of cutting core samples to small pieces. A very important aspect is the reproducibility of data and results. Reproducibility is always bound to possible errors. The identical localization of investigated areas will for example be difficult to obtain. Possible errors of the used analytic methods are systematical due to individual calibration. Thus, the reproducibility of the data obtained with the used analytical methods is better than statistical data of thin sections.

Finally, the data obtained with the μ -EDXRF Tornado M4 CS, as well as with the LIBS CS provide two-dimensional data maps with information about intensities of the distributed elements. Using additional software, possible mineral assemblages, microstructures or different rock types can be revealed in expressive color maps, making interpretations possible.

However, thin sections are not outnumbered by XRF/LIBS when it comes to petrological investigations such as mineral paragenesis and equilibria or identification of minerals.

7.5 INTEGRATED ROCK CLASSIFICATION

In order to interpret chemical and mineralogical data in terms of the total rock column of the strongly sheared Lower Seve Nappe between 1500 to 2500 m drill depth (Lorenz, et al., 2015), the data set gained in this study has been compared and evaluated with pre-existing data sets. Best suited is the petrophysical data set gained on the whole core with the MSCL (Lorenz, et al., 2015). Density values captured every cm along the core are the data with the highest resolution available.

In the core samples selected for this study, differences in the density correlate surprisingly well with lithology. **Figure 48** and **Figure 49** exhibit samples 550 and 689 as RGB-figures with the distribution of Fe (red), K (green) and Si (blue) to demonstrate the chemical composition in comparison to the rock densities.

Three different rock types were classified according to density in this study: amphibolite, potassium-rich phyllonite and gneiss. Densities that are not included in these rock categories are related to fissures, or neglectable rare compositions in the core. The borders between the classes have been set by detailed interpretation of density values for samples 550 and 689. For additional adjustment the density values were laid over the digital photos over the entire lower COSC-1 core using the software “corelyzer”. For the classification the following densities borders have been set:

- fissures or gaps <2.5 g/cm³
- gneiss >2.5 g/cm³ and <2.705 g/cm³
- phyllonite >2.705 g/cm³ and <2.82 g/cm³
- amphibolite >2.82 g/cm³

The classification was applied on the complete bottom part of the core beginning at a depth of 1650 m according to the interpretation of borehole data (Lorenz, et al., 2015) and seismic data (Hedin, et al., 2016) that implied the beginning of the mylonitic zone at about this depth.

The results show that by using the classification based on density values a total 220 m of potassium-rich phyllonites (about 26%) were identified in the lower 850 m of the drill core.

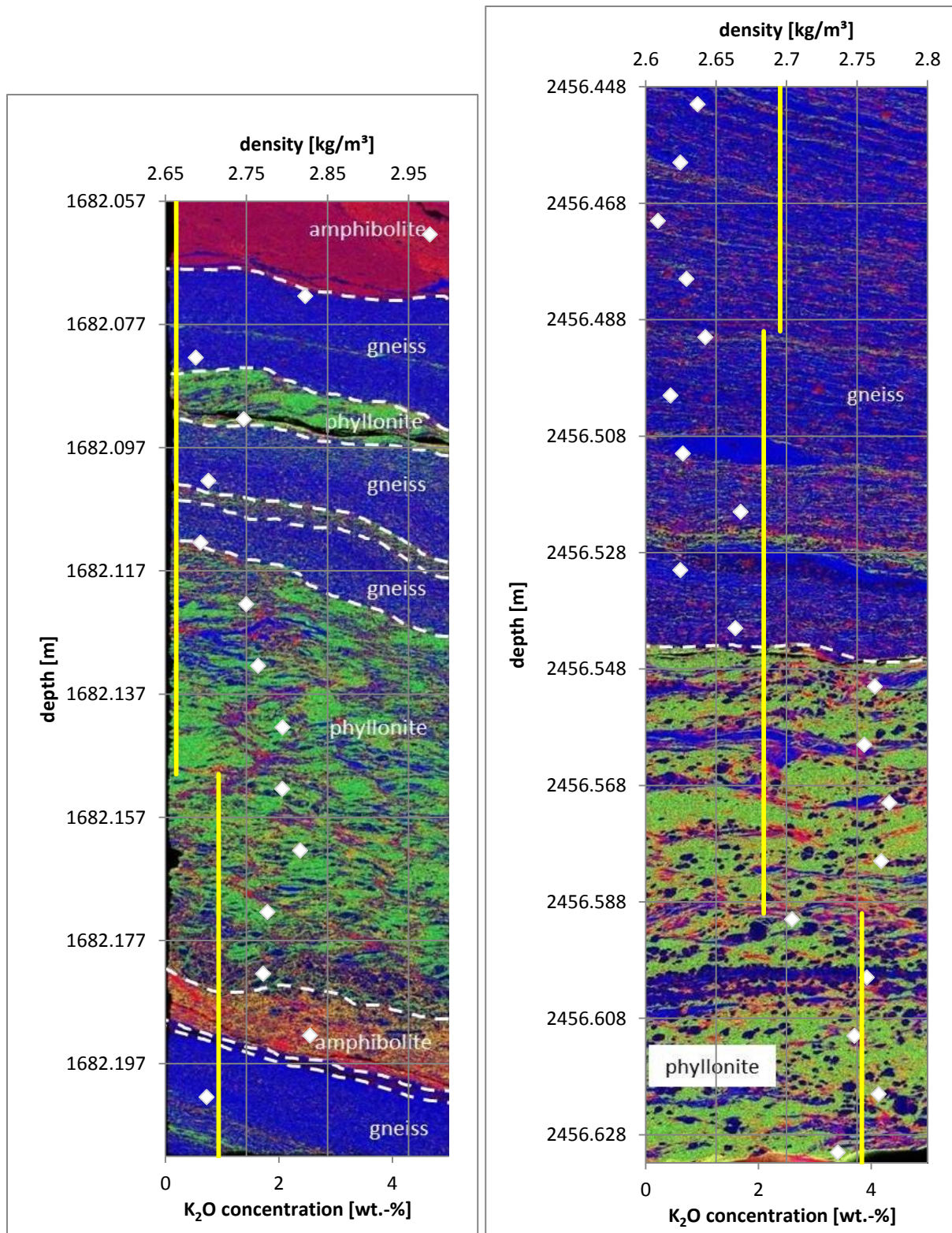


Figure 48 (Left): Element distribution of Fe (red), K (green) and Si (blue) in sample 550. The white diamonds represent the density values; the yellow lines show the K₂O concentration according to Minalyze CS data.

Figure 49 (Right): Element distribution of Fe (red), K (green) and Si (blue) in sample 689. The white diamonds represent the density values; the yellow lines show the K₂O concentration according to Minalyze CS data.

Additionally the K_2O concentrations (depicted as a yellow line) measured by the Minalyzer CS were included in the diagrams (**Figure 48** and **Figure 49**). K-differences that appear to relate to phyllonite occurrences can be seen. However, the results show that due the integration of the data over the length of 10 cm the analysis resolution of the Minalyzer data is not precise enough to capture any small changes in the core. Furthermore, it is not clear whether a depth correction of the Minalyzer data has been executed. Therefore the XRF-data of the Minalyzer CS are not entirely suitable to identify potassium-rich phyllonites at the correct position.

7.6 ELEMENT DISTRIBUTION IN MYLONITES

The EDXRF element maps of the sample 550 (**Figure 48**) and 689 (**Figure 49**) revealed differences in rock composition as well as in mineral textures very well. One of the key questions of this study was to investigate chemical changes across lithological borders to shed light on material exchange and fluid flow. For this purpose the question has risen if a change in the rock composition during metamorphism even existed or not.

First of all metamorphism is described as transformation of rocks effected by mainly pressure and temperature. During this process the rock is in solid state and usually does not change its whole rock composition and remains isochemical. Whereas allochemical processes include the exchange of elements between rocks, usually driven by fluid phases, e.g. aqueous solutions. This process is called metasomatism. During variation of pressure and temperature conditions, recrystallization of minerals occurs and if dynamic stress, such as in mylonitization, appears as well, recrystallization is strongly enhanced (Grujic, et al., 2011). New minerals consequently will be formed. Recrystallization usually occurs during solution of minerals no longer stable in the pore fluid with simultaneous crystallization of the new metamorphic mineral. (Markl, 2015)

Based on the results of the EDXRF and LIBS analyses, as well as on microscopic investigations using a binocular, differences in microstructural behavior and chemistry could be investigated in this study between the different lithologies. The chemically very sharp borders as depicted in **Figure 30** are a prime example. The origin of the alternating lithologies can be explained by at least two possible scenarios as stated above and in a study with very similar rock material (Spruzeniec & Piazzolo, 2015). The first scenario is a metasomatic fluid causing element mobility, redistribution and accumulation in certain border areas, whereas the second scenario is initially heterogen protolith, which faced mylonitization but did not change chemically across lithological borders.

According to White (2005) the low ionic potential of alkali and alkaline earth elements is the reason for their good solubility in aqueous solutions. This consequently makes the elements quite mobile in processes of metamorphism and weathering.

Element transport caused by a metasomatic fluid can therefore be traced with of alkali and alkaline earth elements such as Li, Na, K, Rb and so on. The distribution maps of

these elements derived from LIBS data reveal very sharp borders, as for example Li in sample 550 (**Figure 50**) and 689 (**Figure 51**). The identified phyllonites in these samples are compared to adjacent gneisses with different mineralogical and chemical composition. The different lithologies exhibit linear chemical trends in horizontal profiles as in sample 689. The EDXRF measurements in **Figure 29** do not show a linear chemical trend over lithological borders. Therefore, a chemical metasomatic exchange between the lithologies could not be ascertained.

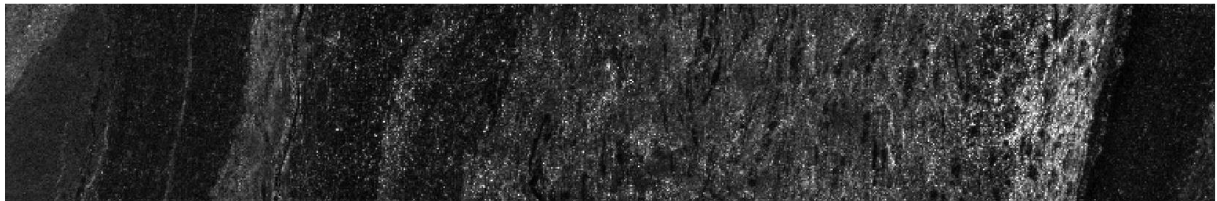


Figure 50: Li distribution map of sample 550 based on LIBS measurements.



Figure 51: Li distribution map of sample 689 based on LIBS measurements.

Additionally, several studies of mylonites with clear metasomatic element transport (Spruzeniece & Piazzolo (2015); Kjøl, et al. (2015); Selverstone, et al. (2012)) had a brittle-ductile deformation and greenschist facies conditions in common. The Lower Seve Nappe in contrast has experienced amphibolite facies conditions (Gee, et al., 2013). Further there were no evidences found of a brittle deformation.

Because of the sharp chemical borders (**Figure 30**), a more explanation for the modification of the mineral composition is the recombination of the chemical element composition inherited from the protolith to a mineral composition that fits to changeable temperature and pressure behaviors due to a tectonical deformation (Vinx, 2015). This implies a protolith with diverse chemistry and grain size. As the most probable source layered greywacke with alternating clay and sand layers often in thick sequences are plausible. According to Vinx (2015) greywacke banks are submarine deposits from suspensions of sediment material and water, so called turbiditic currents. These turbiditic currents are formed when unconsolidated sediment material is deposited on unstable tilted surfaces that episodically collapse and slide down, e.g. on

continental slopes in subduction zones. As explained by Gee (1975) the Seve Nappe Complex is mainly derived from the sedimentary cover of the continent-ocean transition of the outermost margin of Baltica. Sedimentation of greywackes with alternating clay layers on the continental slope before or during subduction is consequently most likely (Gee, et al., 2013). As described by Gee et al. (2013), the Lower Seve Nappe is mainly composed of amphibolite facies metasediments with marbles, calc-silicate rocks and amphibolites. The origin of the amphibolites found for example in sample 550 is possibly an amphibolite facies metamorphosed part of a dolerite dyke-swarms (Gee, et al., 2013). During the subduction of Baltica underneath Laurentia, fault thrusting transported the Seve Nappe Complex several hundreds of kilometers onto Baltica. The high-pressure metamorphism of the Seve Nappe with strong ductile deformation zones is typical in this environment and is called dislocation metamorphism (Vinx, 2015). When metamorphic rock reacts ductile on the mechanical stress, recrystallization forms mylonites with characteristic deformational structure. Mylonitization modifies sedimentary sandy protoliths into stretched mylonitic paragneisses while clay-rich sequences in greywackes are transformed into phyllonites. Such processes explain the strongly oriented minerals and textures in the investigated rocks.

As already mentioned, ductile deformation is very material dependent. According to Heitzmann (1985), quartz already behaves ductile at moving rates of 10^{-10} to 10^{-15} sec^{-1} and temperatures of 300 °C. At temperatures above 650 °C and the presence of water partial melting, called anatexis occurs (Markl, 2015). Rocks including partially molten areas are called migmatitic rocks (Markl, 2015). Because ductile behavior of quartz minerals including recrystallization is present in all samples and beginning anatexis can be observed in sample 625, temperatures must have been at least 650 °C during the pervasive amphibolite facies metamorphism. The strong mylonitization must have been occurred in a later stage at temperatures between 300 and 650 °C.

According to Heitzmann (1985), mylonites are usually common in narrow zones as elongated bands. The mylonitic deformation in the COSC-1 core however is about 850 m thick. Leucocratic mylonitic gneisses alternate with phyllonites, amphibolites, rarely marbles and metasediments. An extrusion wedge was possibly present in the Middle and Upper Seve Nappe as described by Grimmer et al. (2015). It can therefore be speculated that the Lower Seve Nappe studied here has been stacked by an imbrication. The far

transported and elongated Seve Nappe has been piled up forming a stack of several hundred meter thick mylonitic bands.

In summary one quarter of the lower 850 m of the Lower Seve Nappe consists of K-rich phyllonites, while almost two-thirds are composed of leucocratic gneisses. These two different compositions appear in closely interfingering layering with chemically and mineralogically distinct composition. Intercalated amphibolites originated most likely from the metamorphic overprint of dolerite dykes swarms. This metamorphic sequence is a mylonite package of 850 m thickness documenting strong high-grade metamorphisms and intense overprint. The protolith of this rock pile is most likely a layered sequence of alternating sandy to more greywacke turbiditic rocks. The size of the individual layers from mm-wide to several metre wide biotite-rich layers might have been stretched out and thinned out enormously due to the very strong deformation. However, the chemical changes seem to be still those of a layered greywacke sediment rock originated from a continental shelf.

8 OUTLOOK

This master thesis shows the enormous potential of the COSC-1 data set. The very promising results can be used for ongoing research. Research is currently being conducted in Sweden, Australia and Italy on other interesting aspects of the COSC-1 project. In Uppsala, Potsdam and Freiberg further seismic processing and interpretations are still a big part of the project and will be published soon (Hedin, et al., 2016).

The data and results gained in this study will be used for upcoming investigations. Additional core pieces from the lower COSC-1 core section have been sampled for radiometric dating. Dr. Johannes Glodny from section 3.1 of the GFZ: "Inorganic and Isotope Geochemistry" will perform Rb-Sr whole-rock mineral dating on muscovite fractions of phyllonitic sections. The selected samples are completely recrystallized during the strong shearing phase and contain no relictic xenocrysts. This dating method has been used on other Caledonian gneisses quite successfully already (Grimmer, et al., 2015) and is consequently very promising.

Dr. Sandra Piazzolo from Sidney/Australia is working on COSC-1 core samples analyzing their microstructures. Upcoming investigations are aimed at combining geophysical analysis with structural studies on the core samples.

Finally Friederike Körting will try to use the high resolution EDXRF and LIBS data of this master thesis to calibrate the HySpex data in a follow up Master thesis. As already explained in this thesis, the algorithms used on hyperspectral data are based on sedimentary core samples only and can consequently not be used on metamorphic rock samples to get reliable results. Therefore, Friederike Körting will try to address this problem building on the results obtained herein.

9 CONCLUSION

Investigations on the selected core samples of the bottom part of the Lower Seve Nappe confirm the general assumption of a mylonitic zone of approximately 850 m thickness. The interpretations on the results of the different core scanning devices with integration of additional core data further reveal the following conclusions:

- one quarter of the due to seismic interpretations defined mylonitic zone consists of K-rich phyllonites
- two-thirds are composed of leucocratic quartzo-feldspatic gneisses
- they appear in closely interfingering layering with chemically and mineralogically distinct composition
- borders between different lithologies are very sharp
- no chemical trends between different lithologies were proved
- strong high-grade metamorphisms with intense overprint (amphibole facies) including ductile deformation with recrystallization is suggested
- protolith was most likely a pre-metamorphic source rock with layered sequence of alternating sandy to more greywacke turbiditic rocks
- sizes of the individual layers from mm-wide to several metre wide biotite-rich layers may be stretched out and thinned out enormously due to the very strong deformation
- chemical changes seem to be still those of a layered sediment pile of a continental shelf
- μ -EDXRF scanner with high resolution maps of 50 μm can be used perfectly for microstructural investigations and studies on element distributions of heavier elements than Mg
- LIBS can additionally be used to create distribution maps of elements from H to U with a resolution of 200 μm
- hyperspectral analysis show promising results for further investigations
- the used camera requires additional detectors for analyzing quartz and feldspar minerals and a calibration on metamorphic rock

REFERENCES

- Arnbom, J. O., 1980. Metamorphism of the Seve nappes at Åreskutan, Swedish Caledonides. In: *Geol. Fören. Stockh. Förh., 102, Part 4*. s.l.:s.n., pp. 359-371.
- Beckhoff, B. et al., 2006. *Handbook of Practical X-Ray Fluorescence Analysis*. Berlin Heridelberg: Springer.
- Cocks, L. & Torsvik, T., 2002. Earth geography from 500 to 400 million years ago: a faunal and palaeomagnetic review. *Journal of the Geological Society, London*, pp. 631-644.
- Colpron, M. & Nelson, J., 2009. A Palaeozoic Northwest passage: incursion of Caledonian, Baltican and Siberian terranes into eastern Panthalassa, and the early evolution of the North American Cordillera. In: *Cawood, P. A. & Kröner, A. (eds) Earth Accretionary Systems in Space and Time. Geological Society, London, Special Publications, 318*, pp. 273-307.
- Corfu, F., Andersen, T. B. & Gasser, D., 2014. The Scandinavian Caledonides: main features, conceptual. *New Perspectives on the Caledonides of Scandinavia and Related Areas. Geological Society, London, Special Publications, 390*, pp. 9-43.
- Gee, D., 1975. A tectonic model for the central part of the Scandinavian Caledonides. *American Journal of Science, Volume 275A*, pp. 468-515.
- Gee, D. G., Fossen, H., Henriksen, N. & Higgins, A. K., 2008. From the Early Paleozoic Platforms of Baltica and Laurentia to the Caledonide Orogen of Scandinavia and Greenland. *Episodes, 31*, pp. 44-51.
- Gee, D. G. et al., 2012. Subduction along and within the Baltoscandian margin during closing of the Iapetus Ocean and Baltica-Laurentia collision. *Lithosphere, 5(2)*, pp. 169-178.
- Gee, D. G. et al., 2013. The Baltoscandian margin detrital zircon signatures of the central Scandes. *Geological Society, London, Special Publications, Volume 390*.
- Gee, D. & Sturt, B. A. (., 1985. *The Caledonide orogen - Scandinavia and related areas: Chichester: John Wiley and Sons*. Chichester, 1266 pp.: s.n.
- Gilotti, J. A., 1989. Reaction progress during mylonitization of basaltic dikes along the Särsv thrust, Swedish Caledonides. *Contrib Mineral Petrol*.
- Graf, T., 2009. *Grundlagen der Laserstrahlquellen 1. Auflage*. Wiesbaden: Vieweg+Tübner.
- Grimmer, J. C. et al., 2015. Early- to mid-Silurian extrusion wedge tectonics in the central Scandinavian Caledonides. *GEOLOGY, 43(4)*, pp. 347-350.
- Grujic, D., Stipp, M. & Wooden, J. L., 2011. Thermometry of quartz mylonites: Importance of dynamic recrystallization on Ti-in-quartz reequilibration. *Geochemistry Geophysics Geosystems G³, 12(6)*, pp. 1-19.
- Hedin, P. et al., 2016. 3D reflection seismic imaging at the 2.5 km deep COSC-1 scientific borehole, central Scandinavian Caledonides. *Tectonophysics, excepted*.

- Hedin, P., Juhlin, C. & Gee, D. G., 2012. Seismic imaging of the Scandinavian Caledonides to define ICDP drilling sites. *Tectonophysics* 554-557, pp. 30-41.
- Heitzmann, P., 1985. Kakirite, Kataklasite, Mylonite : zur Nomenklatur der Metamorphite mit Verformungsgefügen. *Eclogae Geologicae Helveticae*, Band 78.
- Kjøll, H., Viola, G., Menegon, L. & Sørensen, B. E., 2015. Brittle–viscous deformation of vein quartz under fluid-rich lower greenschist facies conditions. *Solid Earth*, Volume 6, pp. 681-699.
- Klonowska, I. et al., 2015. The UHP metamorphic Seve Nappe Complex of the Swedish Caledonides – a new occurrence of the microdiamond-bearing gneisses and their exhumation. *Geophys. Res. Abstr.*, vol. 17, EGU2015–11609, European Geosciences Union, Vienna.
- Koerting, F. et al., 2015. *Drill core mineral analysis by means of the hyperspectral imaging spectrometer HySpex, XRD and ASD in Proximity of the Mýtina Maar, Czech Republic*. s.l., Sensors & Models in Photogrammetry & Remote Sensing.
- Kokaly, R. F., 2011. *PRISM: Processing Routines in IDL for Spectroscopic Measurements (Installation Manual and User's Guide, Version 1.0) 2011-1155*, s.l.: U.S. Geological Survey.
- Krause, A., 2007. *Die Welt der Kelten - Geschichte und Mythos eines rätselhaften Volkes*. 2nd ed. Frankfurt/Main: Campus Verlag GmbH.
- Ladenberger, A. et al., 2014. Tectonometamorphic evolution of the Åreskutan Nappe – Caledonian history revealed by SIMS U–Pb zircon geochronology. *Geol. Soc. Lond. Spec. Publ.*, 390, p. 337–368.
- Lorenz, H., Gee, D. G., Larionov, A. & Majka, J., 2012. The Grenville-Sveconorwegian Orogen in the High Arctic. *Geol. Mag.*, 149(doi:10.1017/S0016756811001130), pp. 875-891.
- Lorenz, H. et al., 2015. COSC-1 – drilling of a subduction-related allochthon in the Palaeozoic Caledonide orogen of Scandinavia. *Scientific Drilling*, 29 May, pp. 1-11.
- Lorenz, H. et al., 2015. *COSC-1 operational report - Operational data sets*. GFZ Data Services., : <http://dx.doi.org/10.1594/GFZ.SDDB.ICDP.5054.2015>.
- Majka, J. et al., 2014. Microdiamond discovered in the Seve Nappe (Scandinavian Caledonides) and its exhumation by the “vacuum-cleaner” mechanism. *GEOLOGY - Geological Society of America*.
- Markl, G., 2015. *Minerale und Gesteine*. 3rd ed. Berlin Heidelberg: Springer Verlag.
- Marshak, S., 2009. *Essentials of Geology*. 3rd Hrsg. s.l.:W. W. Norton & Company.
- Mielke, C. et al., 2014. Spaceborne Mine Waste Mineralogy Monitoring in South Africa, Applications for Modern Push-Broom Missions: Hyperion/OLI and EnMAP/Sentinel-2. *remote sensing*, Band 6, pp. 6790-6816.
- Norsk Elektro Optikk AS, 2015. *User Guide - HySpex General*, www.hyspex.no, access date 20.10.2015, Phone: +47 67 97 47 00 - Fax: +47 67 97 49 00 E-mail:

- HySpex@neo.no - Web: www.hyspex.no: P.O.Box 384, Solheimveien 62A, N-1471 Lørenskog, NORWAY.
- Oliot, E. et al., 2014. Mid-crustal shear zone formation in granitic rocks: Constraints from quantitative textural and crystallographic preferred orientations analyses. *Tectonophysics*, Volume 612-613, pp. 63-80.
- Rammlmair, D. & Maima, J., 2014. *Multiscale Phase Mapping by LIBS and μ -EDXRF*, Sandton, Johannesburg, South Africa: 21st General Meeting of the International Mineralogical Association (IMA).
- Rogass, C., Segl, K., Kuester, T. & Kaufmann, H., 2013. Performance of correlation approaches for the evaluation of spatial distortion reductions. *Remote Sensing Letters*, 4, 12, pp. 1214-1223.
- Schenk & Kremer, 2014. *Physikalisches Praktikum*. 14 ed. Heidelberg, Wiesbaden: Springer Spektrum.
- Selverstone, J., Axen, G. J. & Luther, A., 2012. Fault localization controlled by fluid infiltration into mylonites: Formation and strength of low-angle normal faults in the midcrustal brittle-plastic transition. *Journal of Geophysical Research*, Volume 117.
- Sjöqvist, A. et al., 2015. An innovative optical and chemical drill core scanner. *Scientific Drilling*, 19, pp. 13-16.
- Spruzeniece, L. & Piazzolo, S., 2015. Strain localization in brittle–ductile shear zones: fluid-abundant vs. fluid-limited conditions (an example from Wyangala area, Australia). *Solid earth*, Band 6, pp. 881-901.
- TERRACORE-brochure, 2016. Anon.. [Online] Available at: http://terracoregeo.com/wp-content/uploads/2014/11/TC_Mineral-Detection-and-Infrared-Wavelengths.pdf [Accessed 14 01 2016].
- TORNADO-brochure, M., 2015. Anon.. [Online] Available at: https://www.bruker.com/fileadmin/user_upload/8-PDF-Docs/X-rayDiffraction_ElementalAnalysis/mXRF/Brochures/Bro_m4_tornado_8p_en_rev_3_1_lowres.pdf [Accessed 7 11 2015].
- Torsvik, T. H. & C. L. R. M., 2005. Norway in space and time: a Centennial cavalcade. *Norwegian Journal of Geology*, 85, pp. 73-86.
- Torsvik, T. H., 1998. Palaeozoic paleogeography: a North Atlantic viewpoint. *Geologiska Föreningens i Stockholm Förhandlingar*, 120, pp. 109-118.
- Torsvik, T. H. S. M. e. a., 1996. Continental break-up and collision in the Neoproterozoic and Palaeozoic – a tale of Baltica and Laurentia. *Earth-Science Reviews*, 40, pp. 229-258.
- Torsvik, T. H. v. d. V. R. e. a., 2012. Phanerozoic polar wander, paleogeography and dynamics. *Earth Science Reviews*, 114, pp. 325-368.

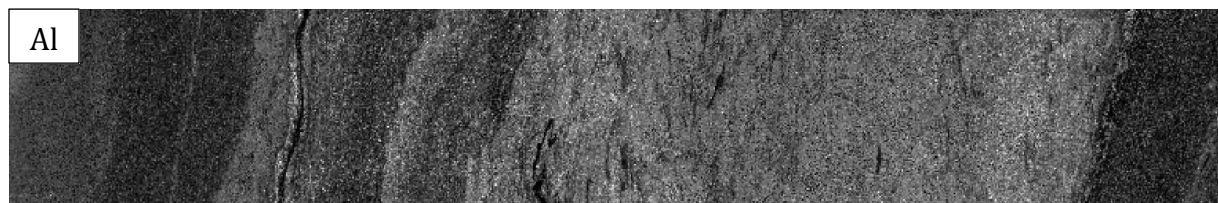
- US Army Research Laboratory, 2015. *Anon.* [Online]
Available at: <http://www.arl.army.mil/www/default.cfm?page=247>
[Accessed 6 11 2015].
- van Staal, C., Barr, S. & Murphy, J., 2012. Provenance and tectonic evolution of Ganderia: Constraints on the evolution of the Iapetus and Rheic oceans. *Geology*, 40, pp. 987-990.
- Vinx, R., 2015. *Gesteinsbestimmung im Gelände; 4. Auflage*. Berlin, Heidelberg: Springer-Verlag GmbH.
- Wastenson, L. et al., 1994. *National Atlas of Sweden - Geology*. s.l.:SNA.
- White, M. W., 2005. Chapter 7: Trace Elements in Igneous Processes. In: *Geochemistry*. s.l.:s.n., pp. 259-313.
- www.appliedspectra.com, 2015. *Anon.* [Online]
Available at: <http://www.appliedspectra.com/technology/LIBS.html>
[Accessed 6 11 2015].
- www.hyspex.no, 2015. *Anon.* [Online]
Available at: <http://www.hyspex.no/products/>
[Accessed 9 11 2015].
- www.laboratoryequipment.com, 2015. *Anon.* [Online]
Available at: <http://www.laboratoryequipment.com/articles/2012/02/pittcon-product-introductions-lead-way>
[Accessed 6 11 2015].
- www.xos.com, 2015. *Anon.* [Online]
Available at: <https://xos.com/technologies/xrf/micro-x-ray-fluorescence-%CE%BCxrf/>
[Accessed 7 11 2015].
- Zachrisson, E. & Sjöstrand, T., 1990. *Bedrock Map 22E Frostviken: Sveriges Geologiska Undersökning (SGU) Ai 44, scale 1:50,000.* s.l.:s.n.

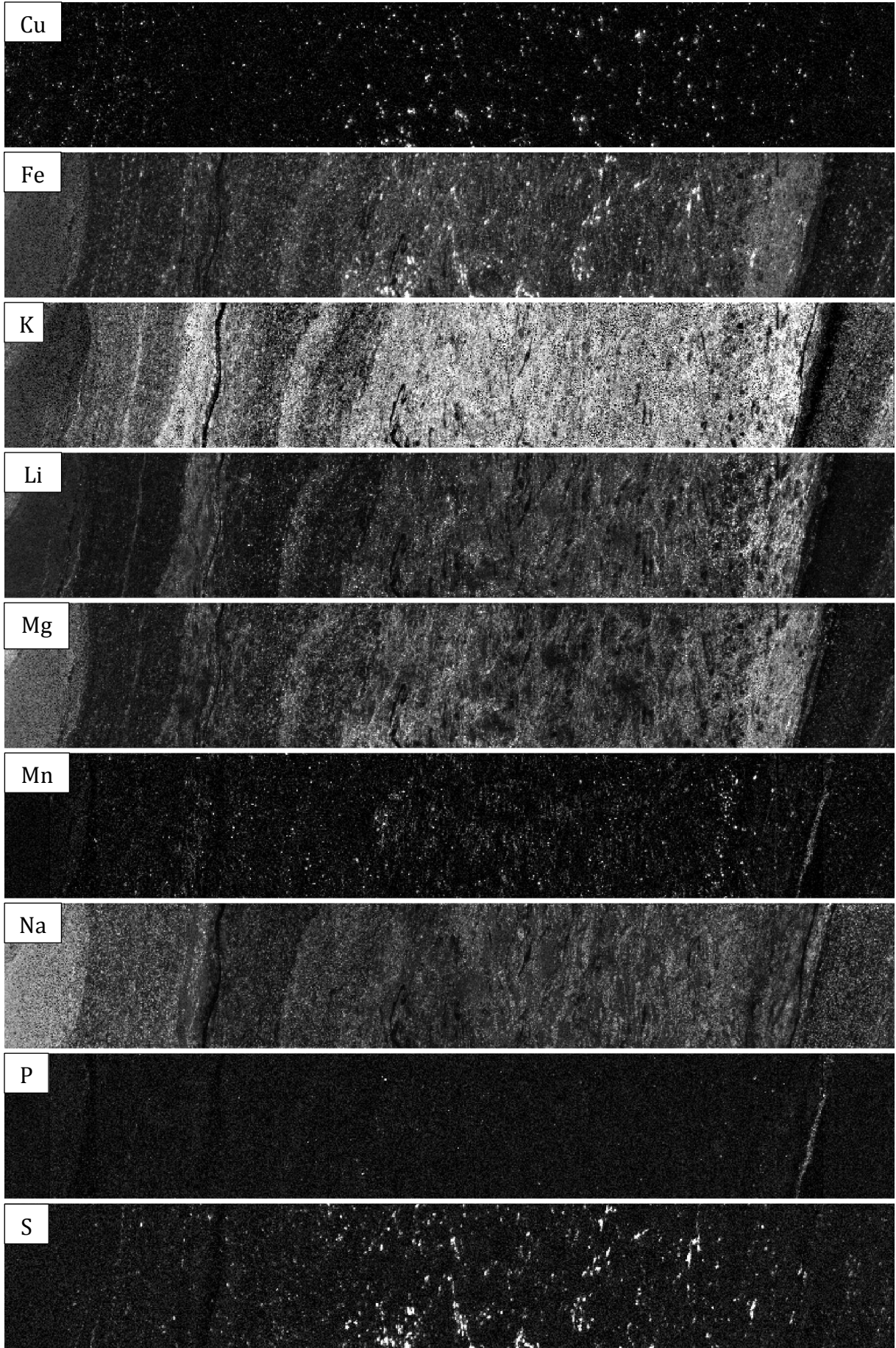
10 APPENDIX

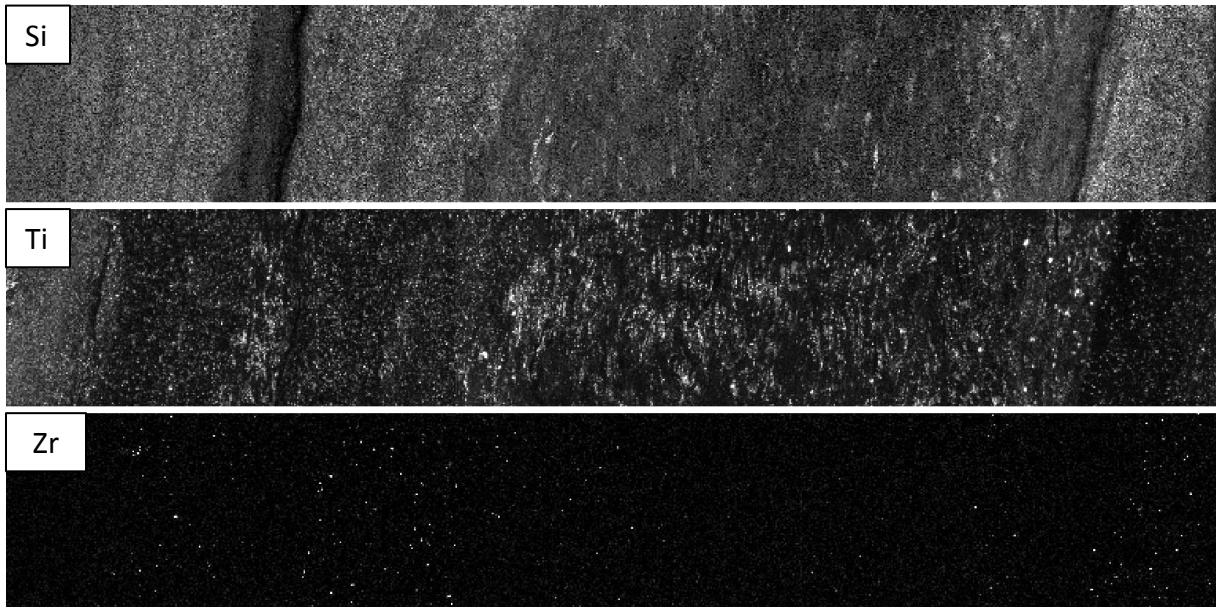
10.1 LIBS DATA

10.1.1 DISTRIBUTION MAPS OF ELEMENTS DETECTED

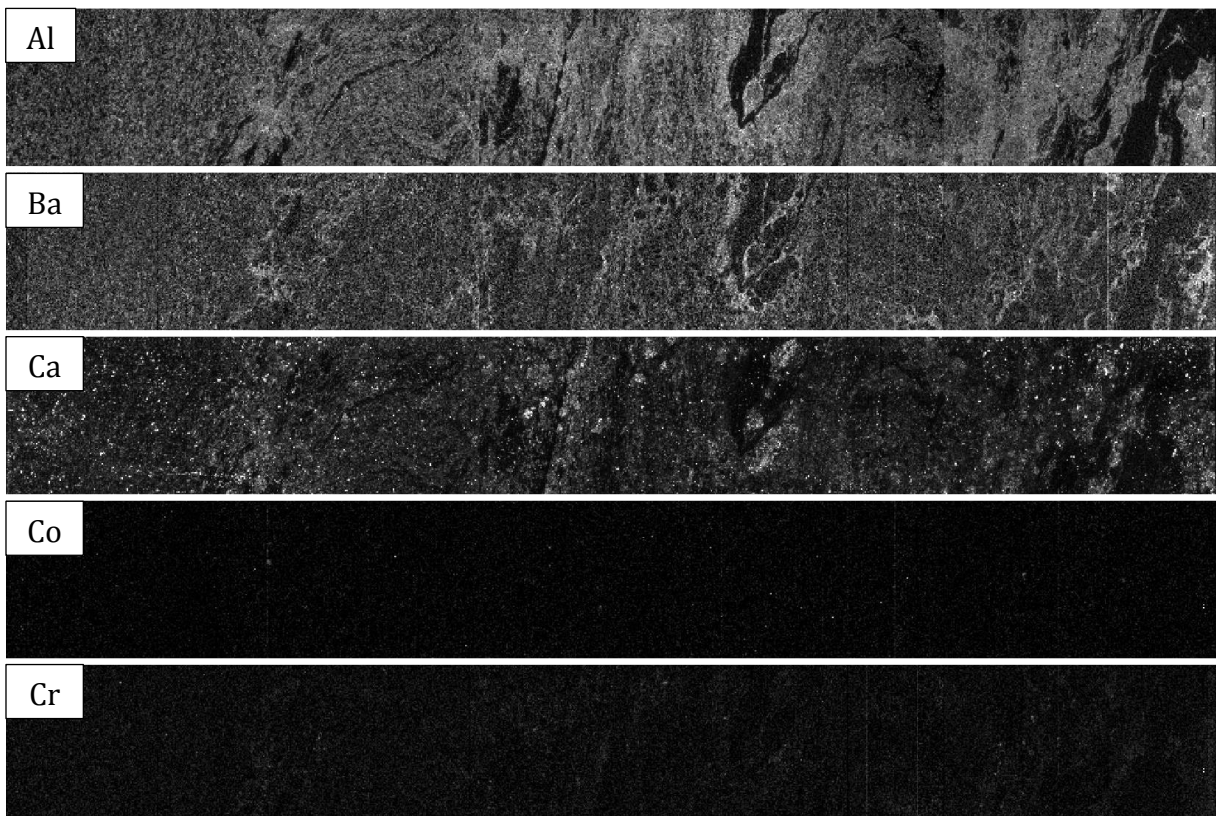
10.1.1.1 SAMPLE 550 (MEASURED AREA ENCIRCLED IN RED)

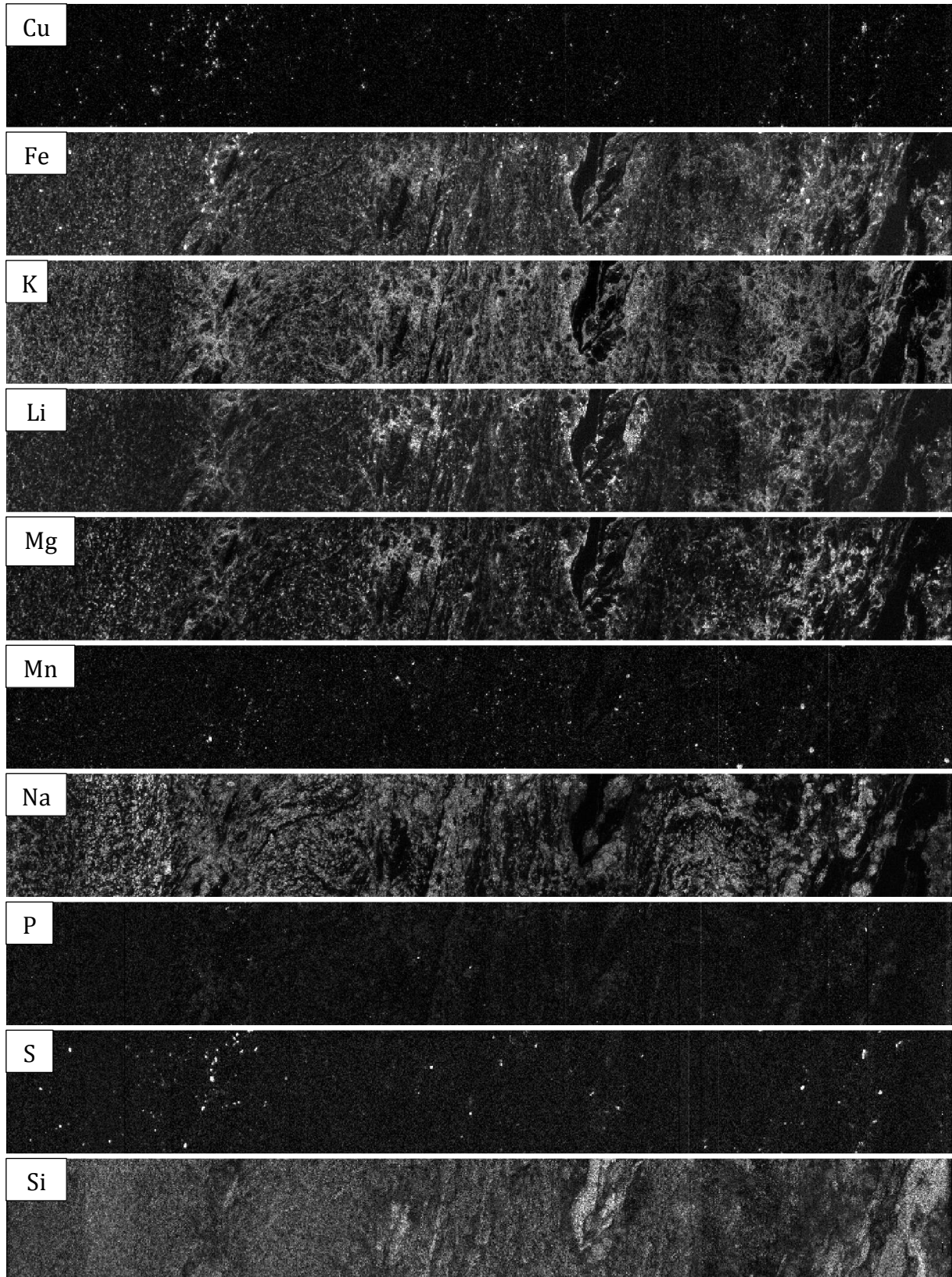


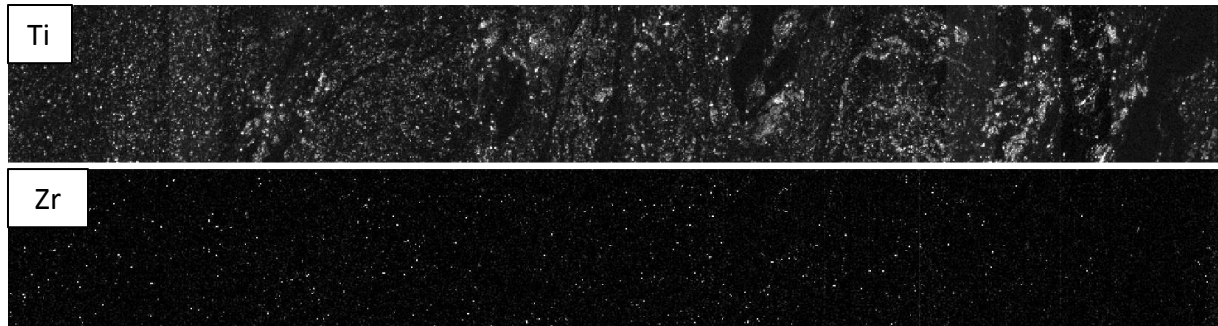




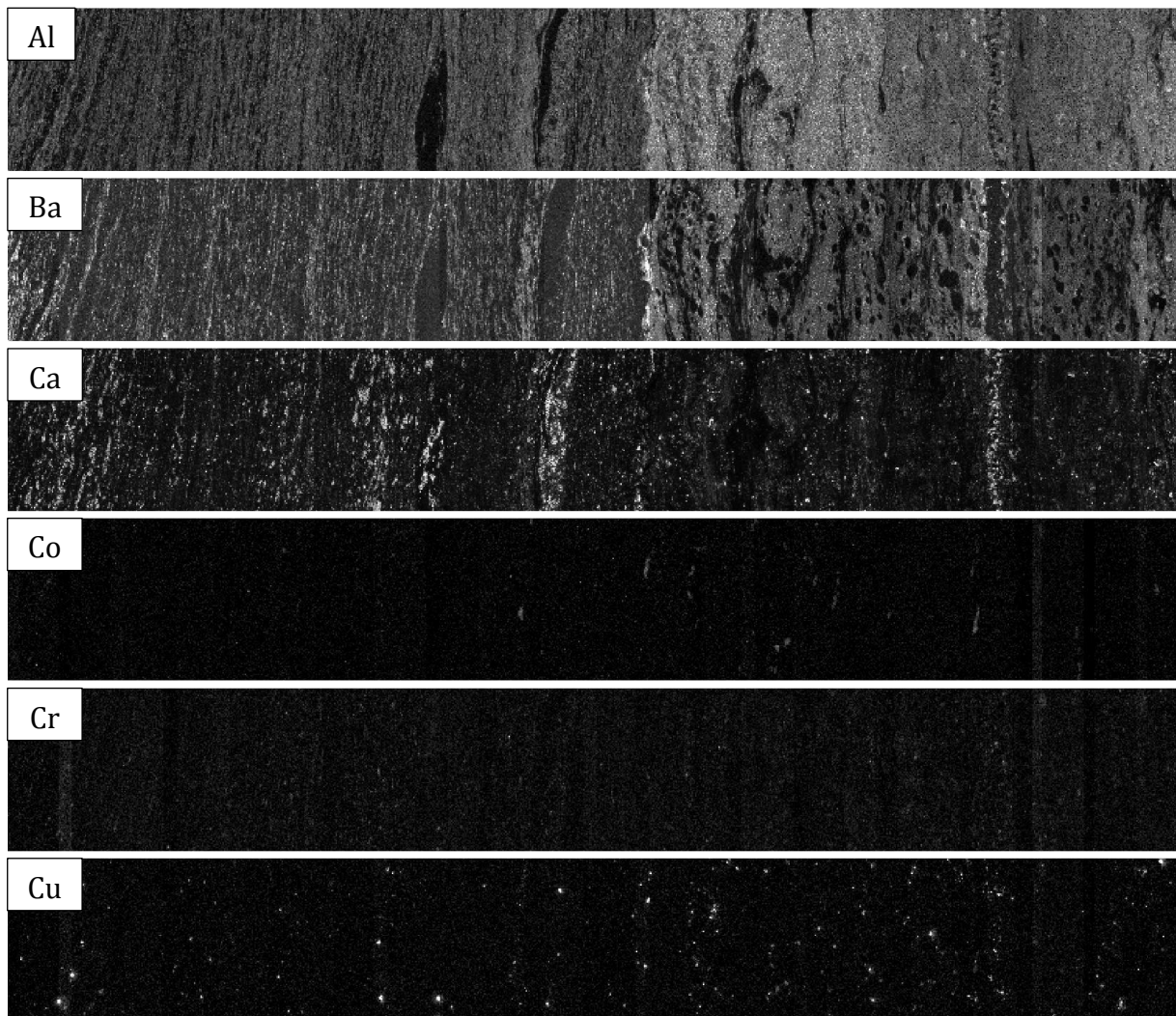
10.1.1.2 SAMPLE 625

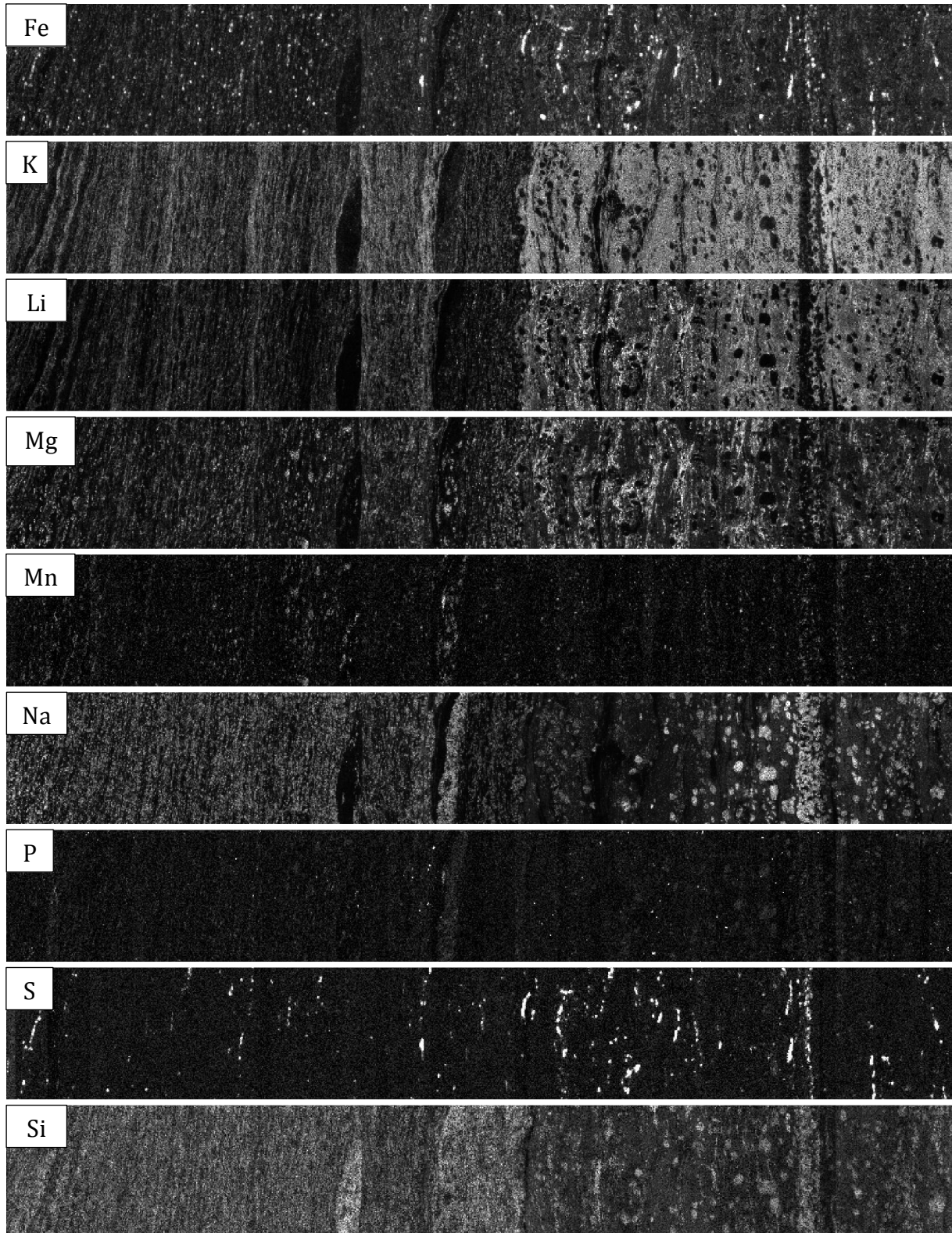


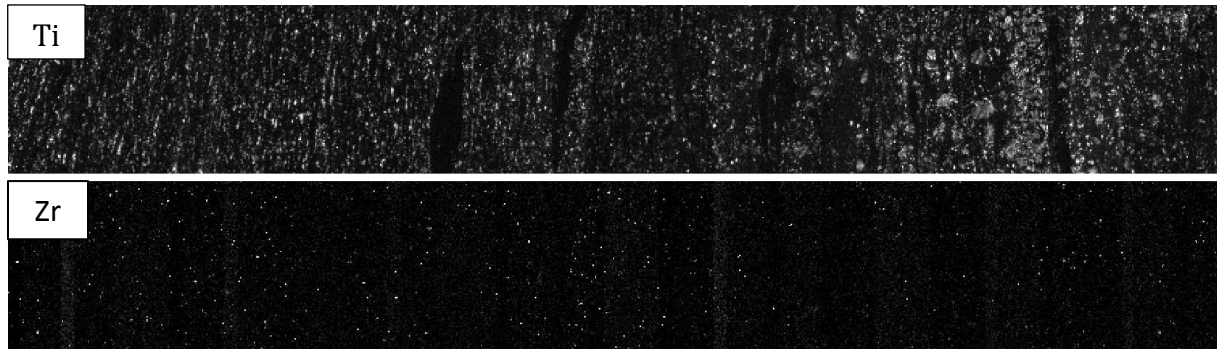




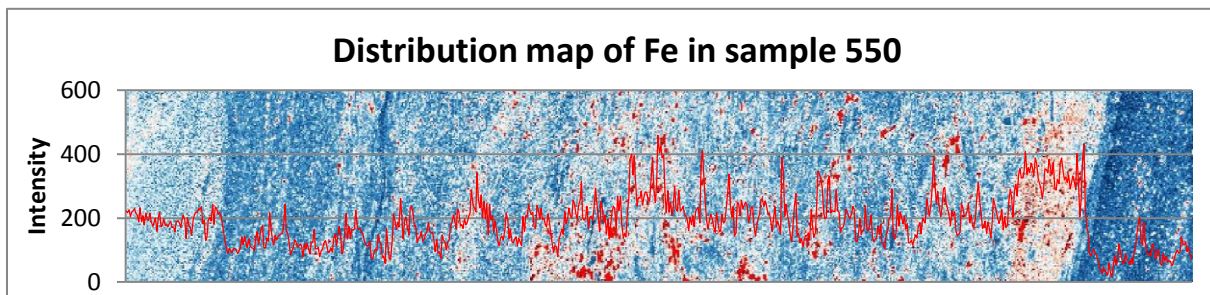
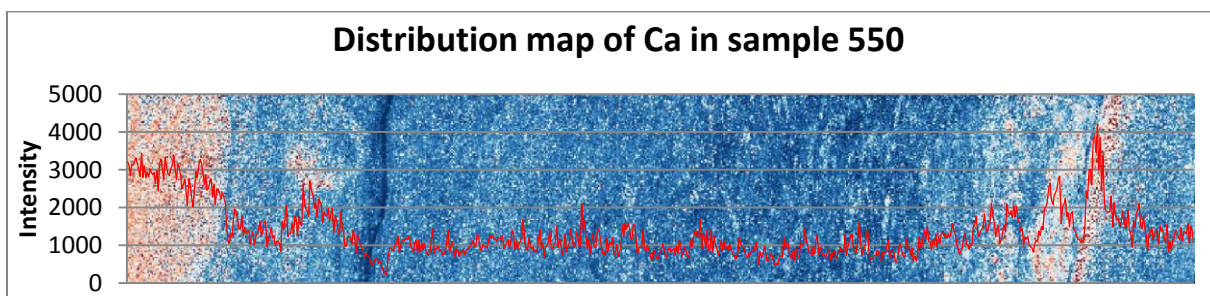
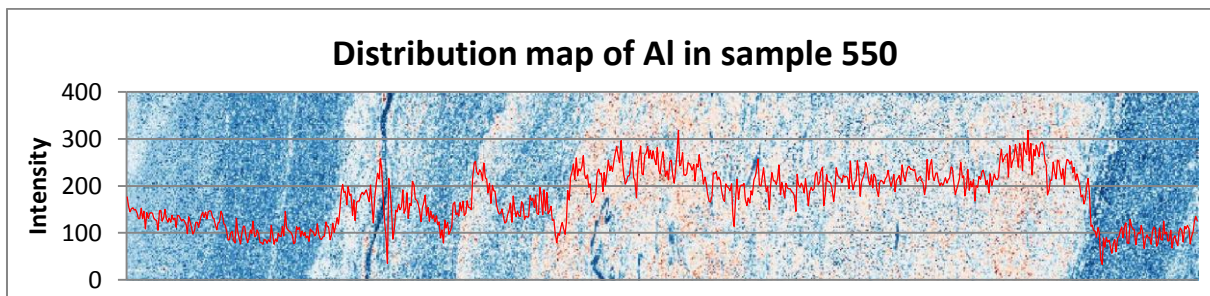
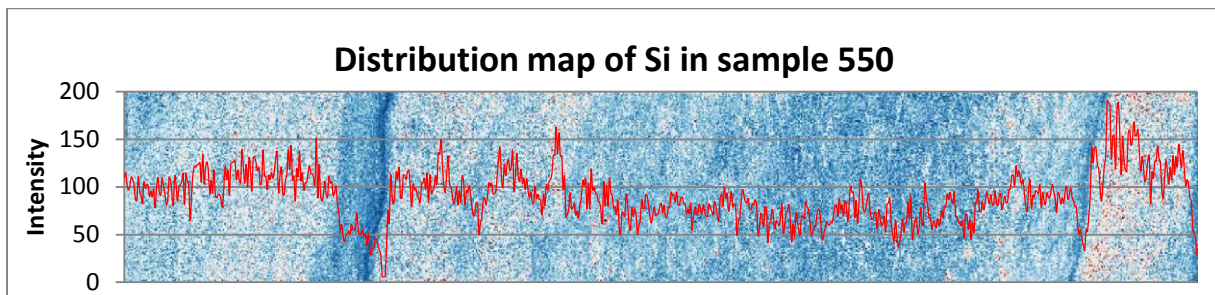
10.1.1.3 SAMPLE 689



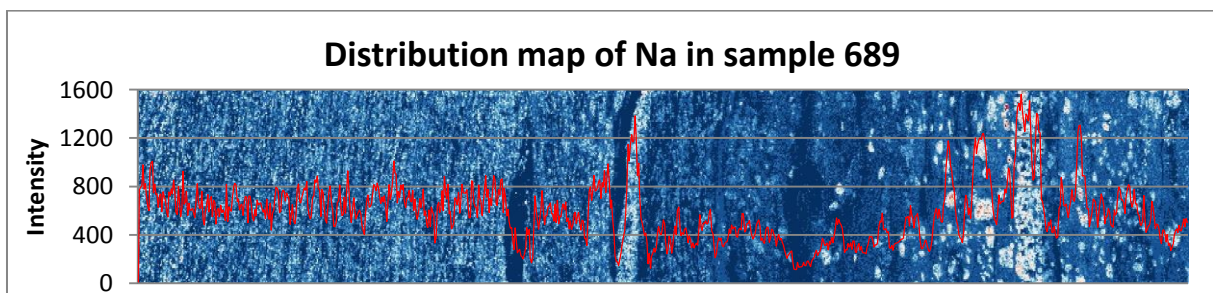
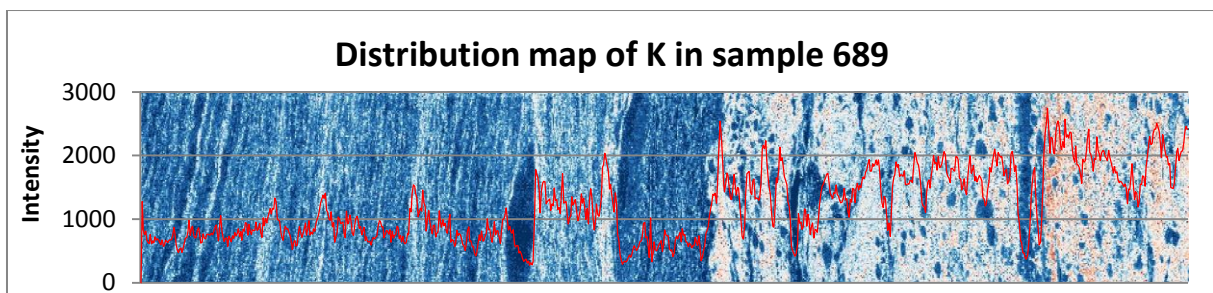
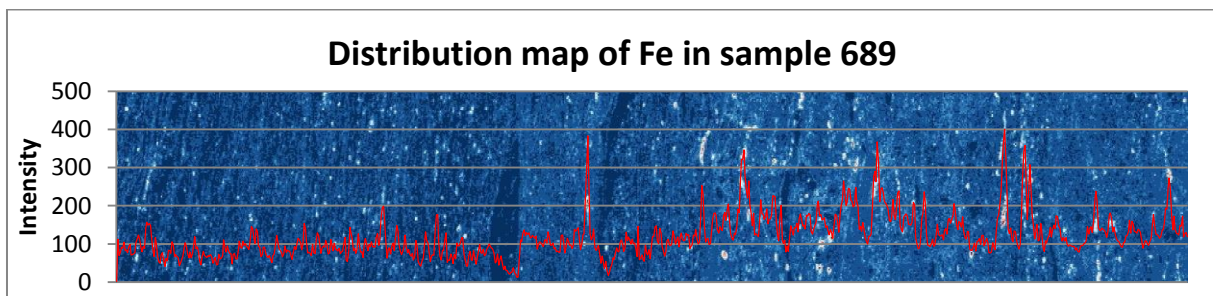
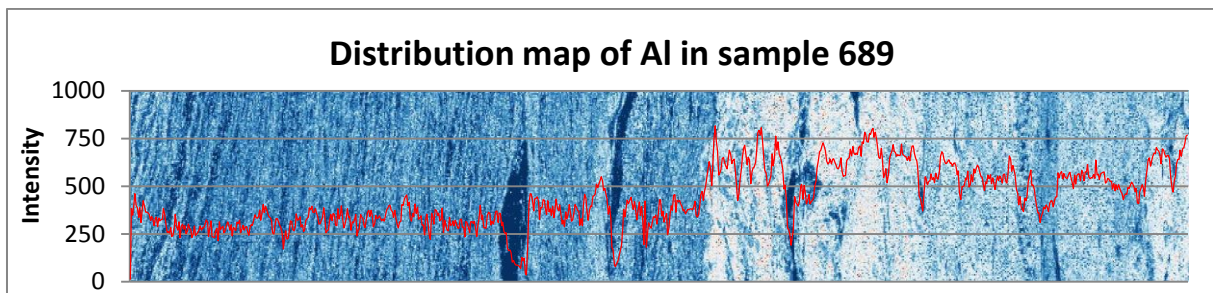
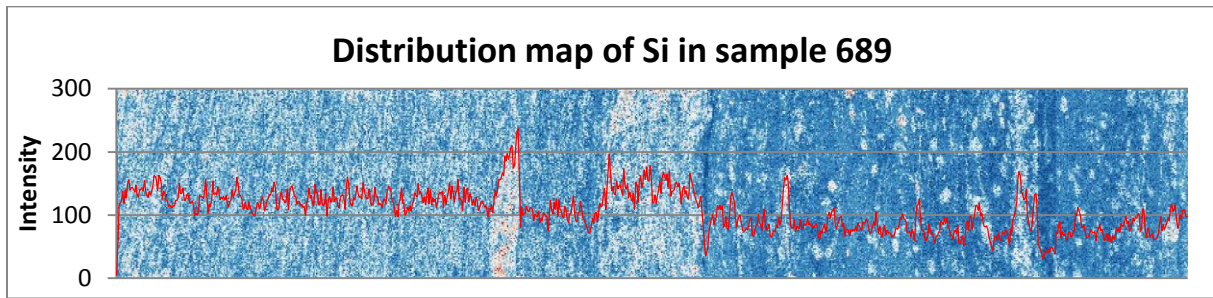




10.1.2 HORIZONTAL PROFILING ON SAMPLE 550



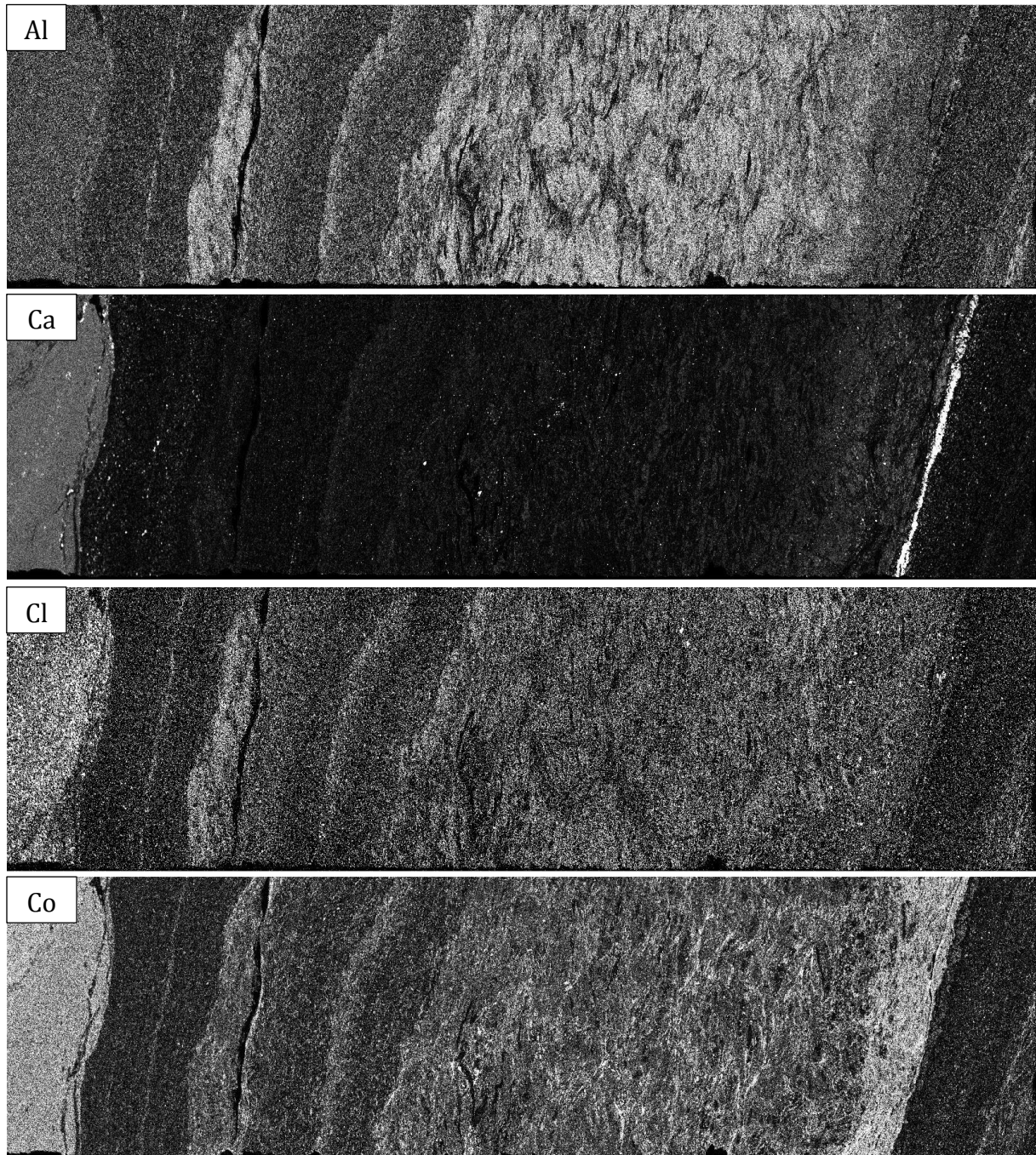
10.1.3 HORIZONTAL PROFILING ON SAMPLE 689

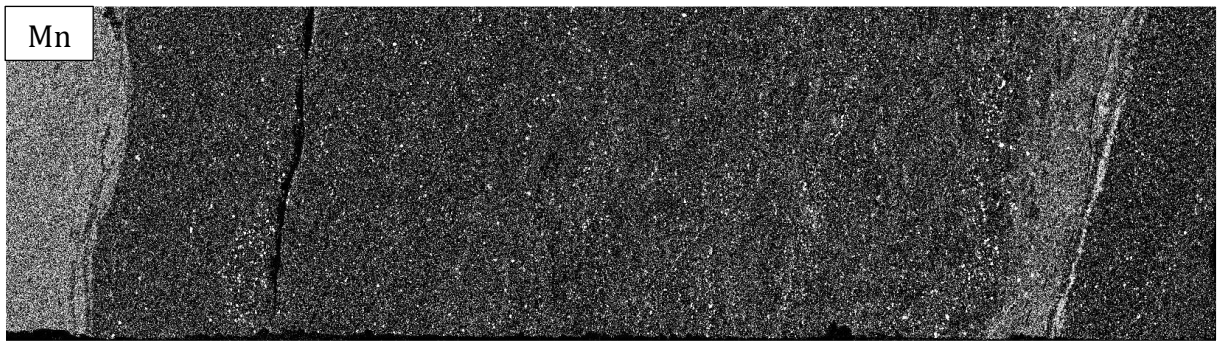
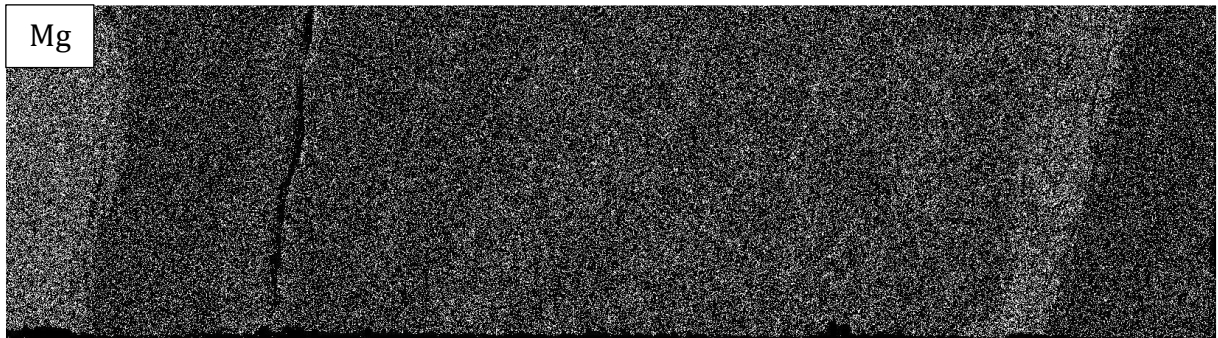
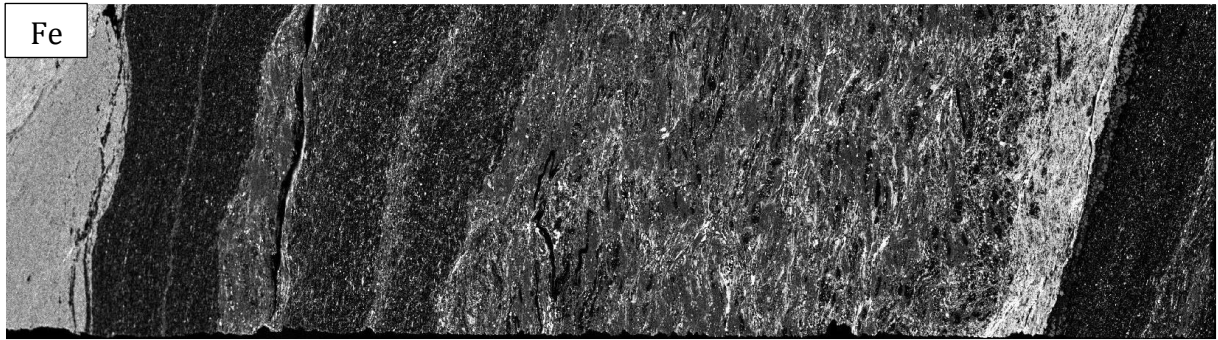
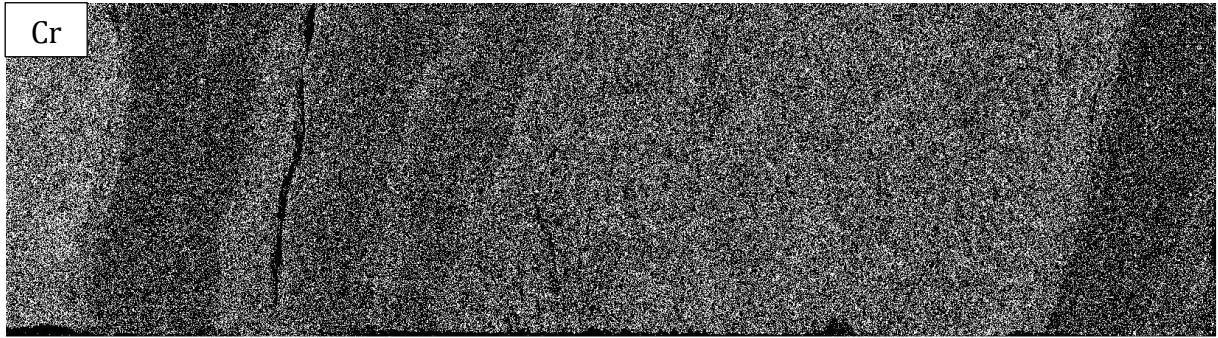


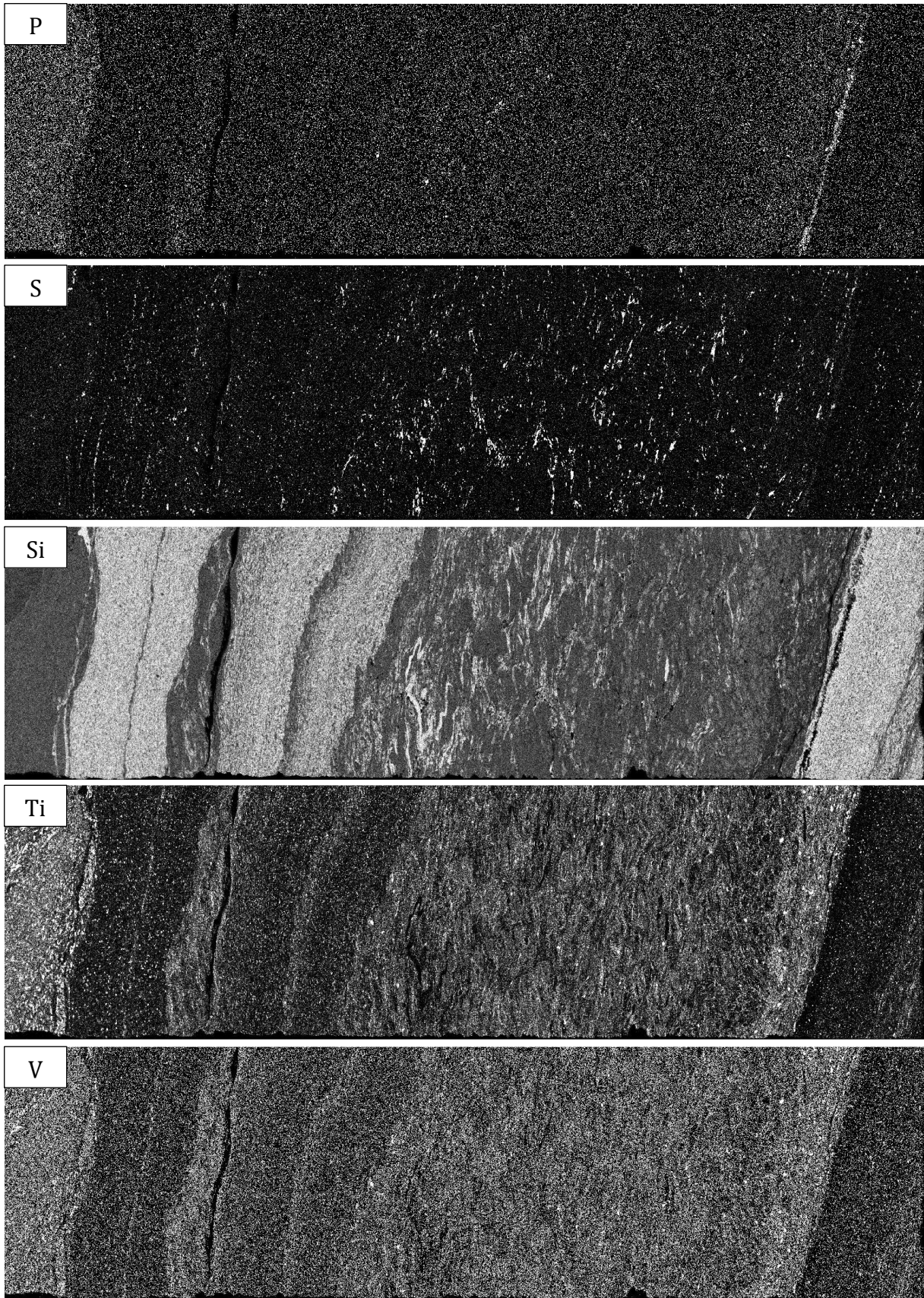
10.2 EDXRF DATA

10.2.1 DISTRIBUTION MAPS OF ELEMENTS DETECTED

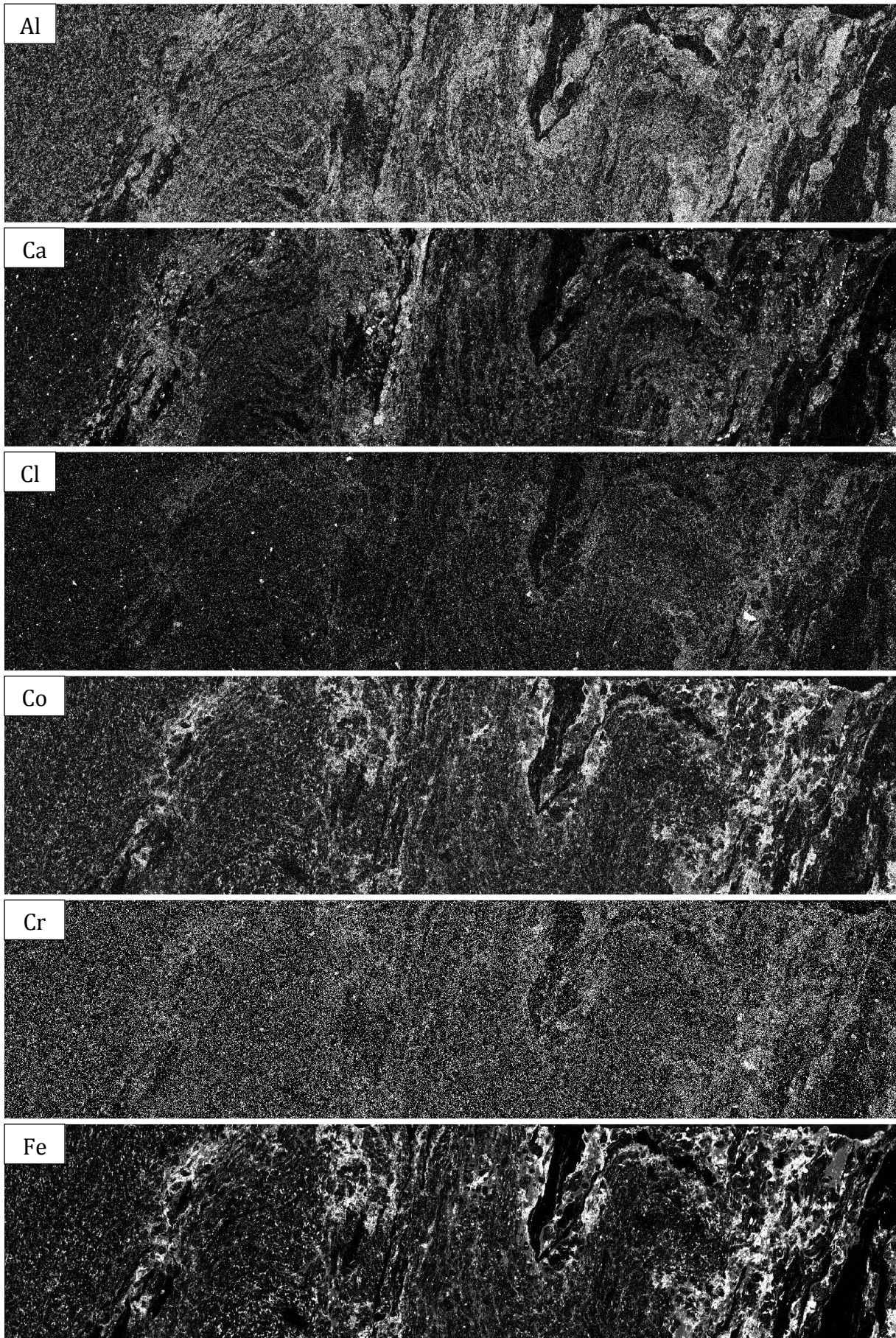
10.2.1.1 SAMPLE 550

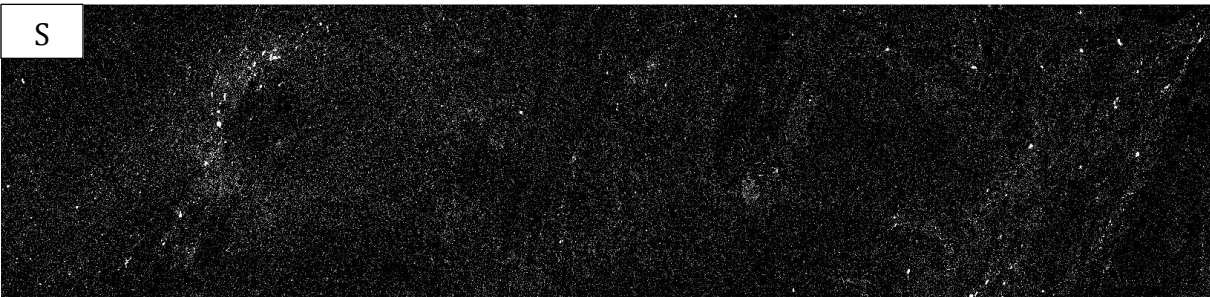
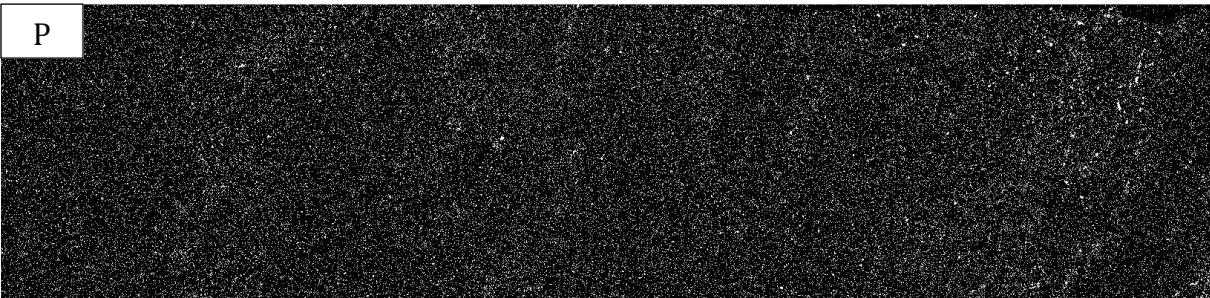
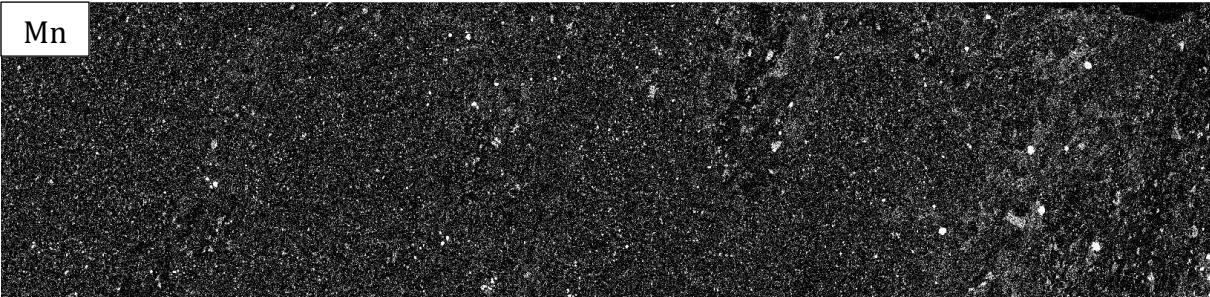
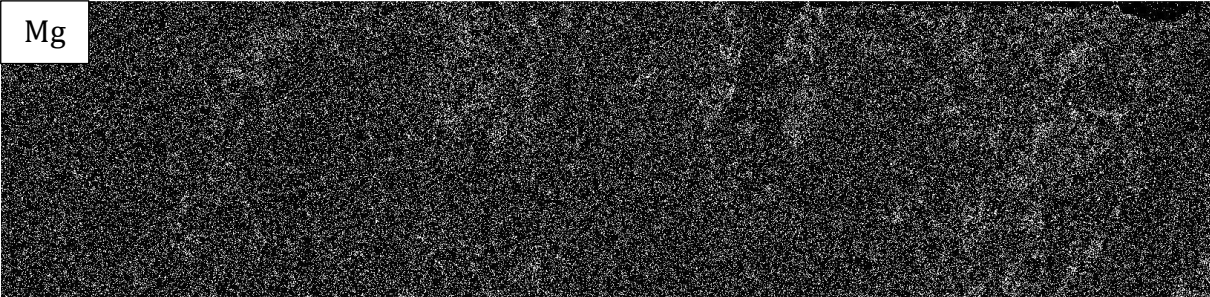
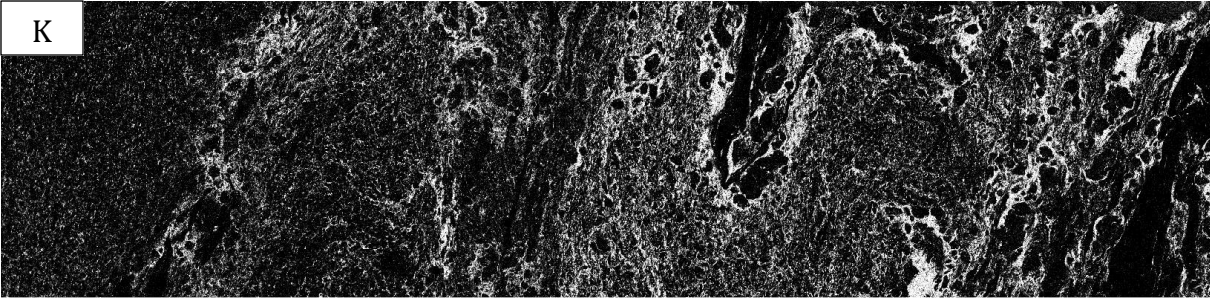


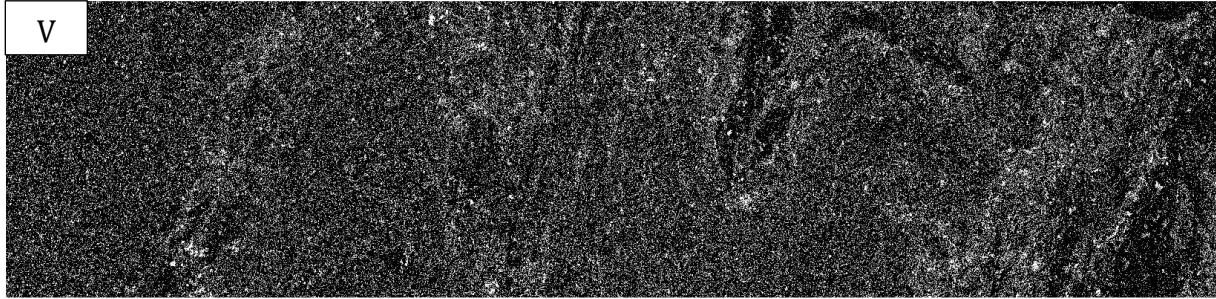
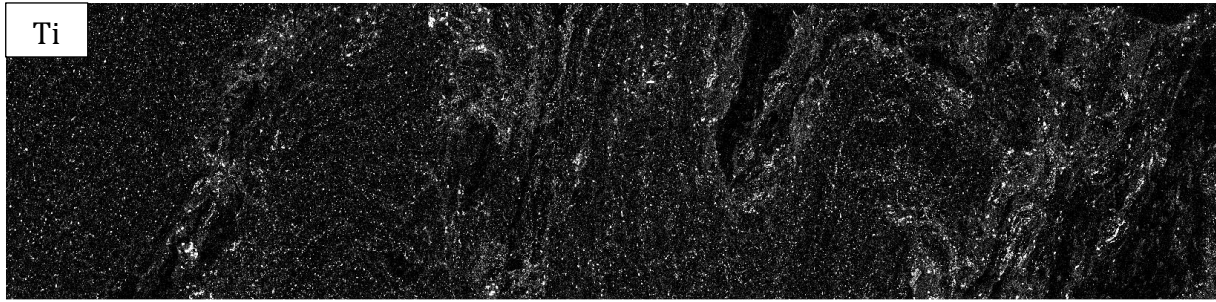




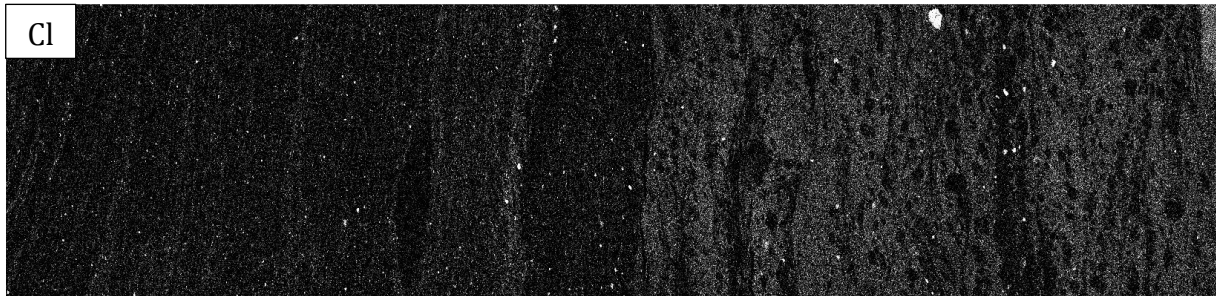
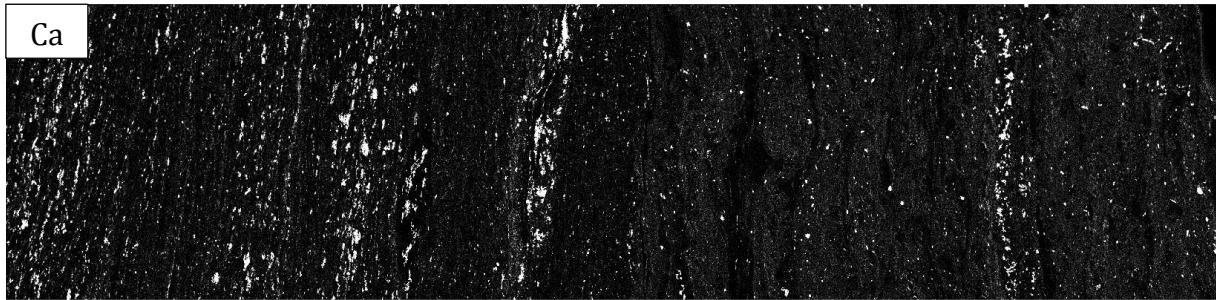
10.2.1.2 SAMPLE 625

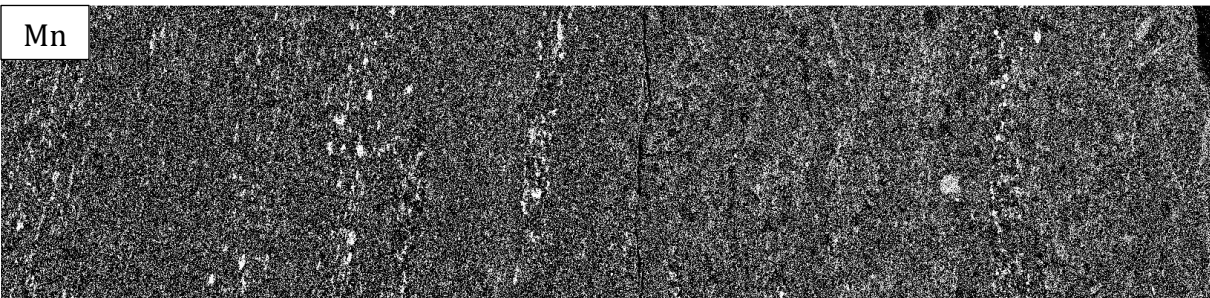
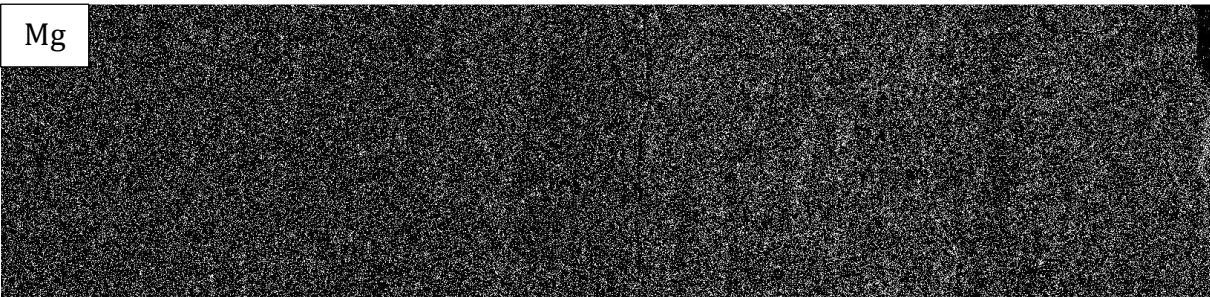
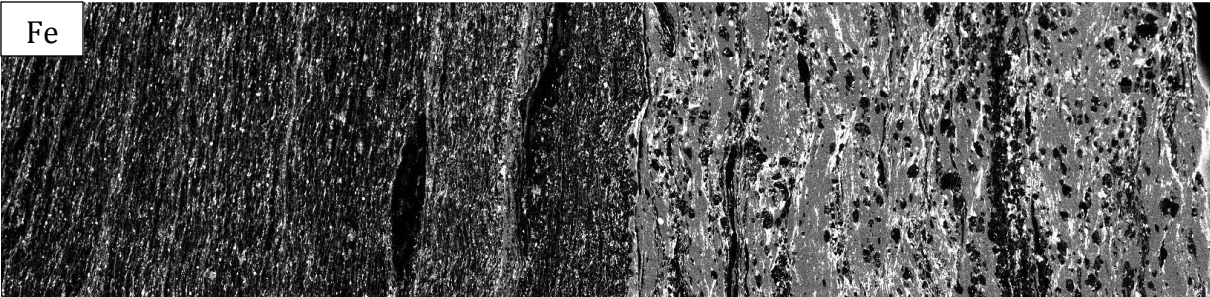
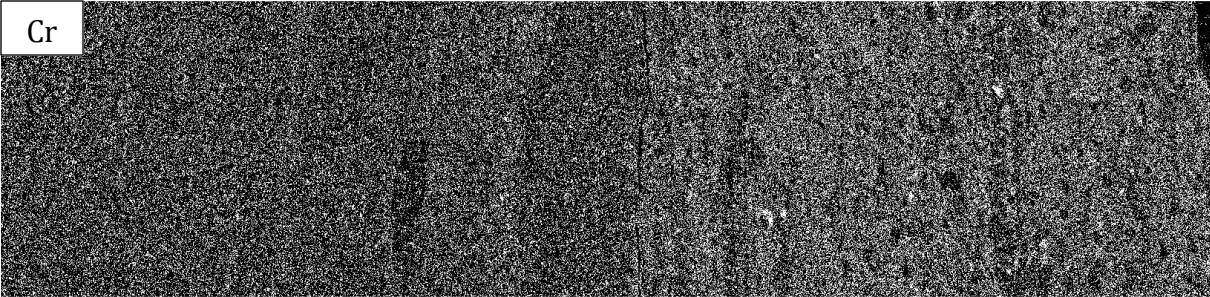


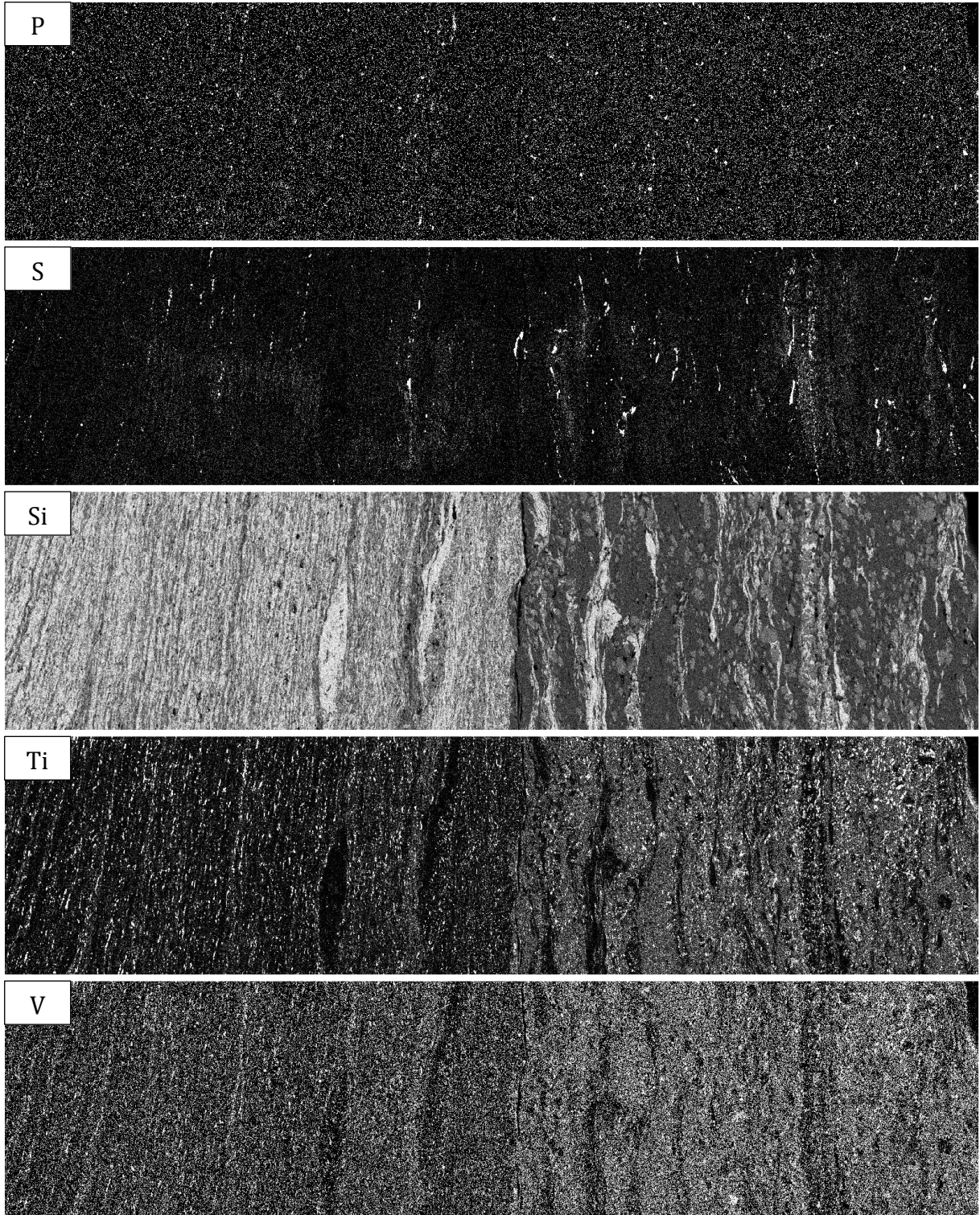




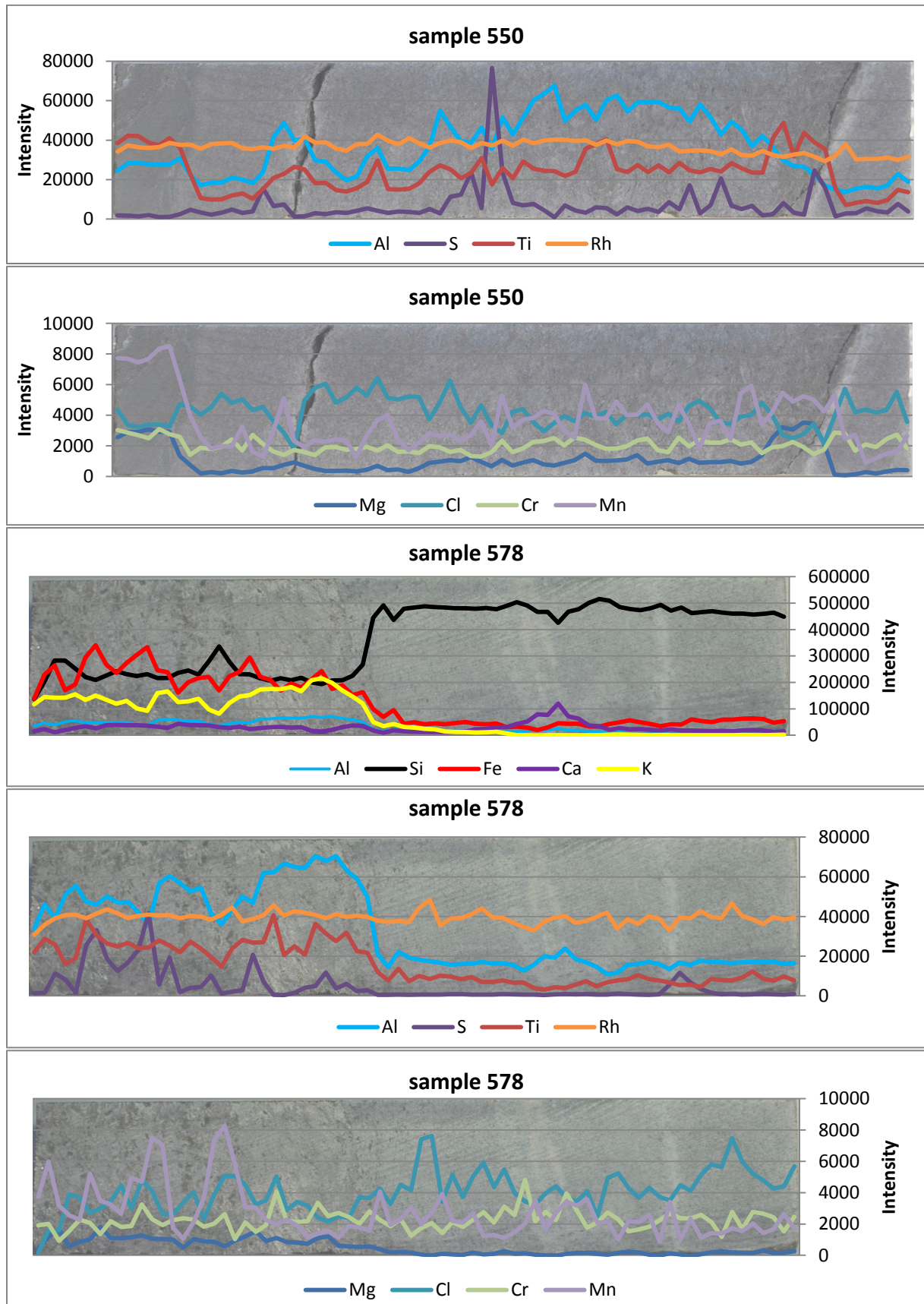
10.2.1.3 SAMPLE 689

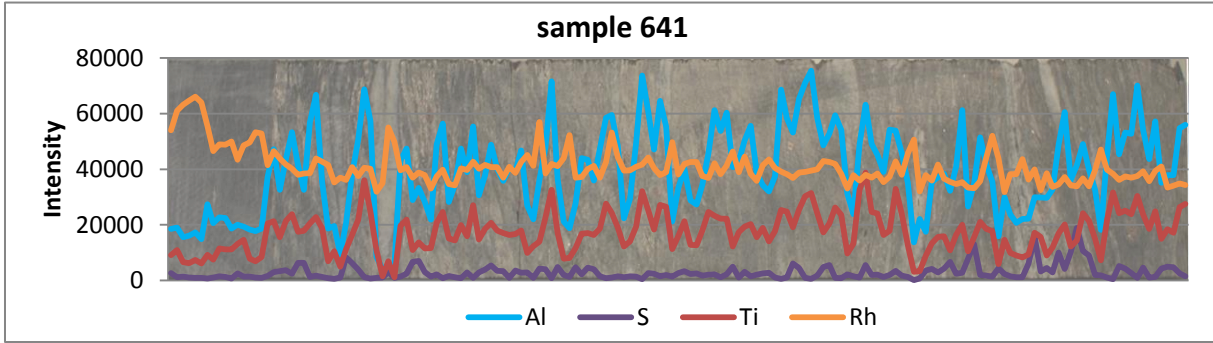
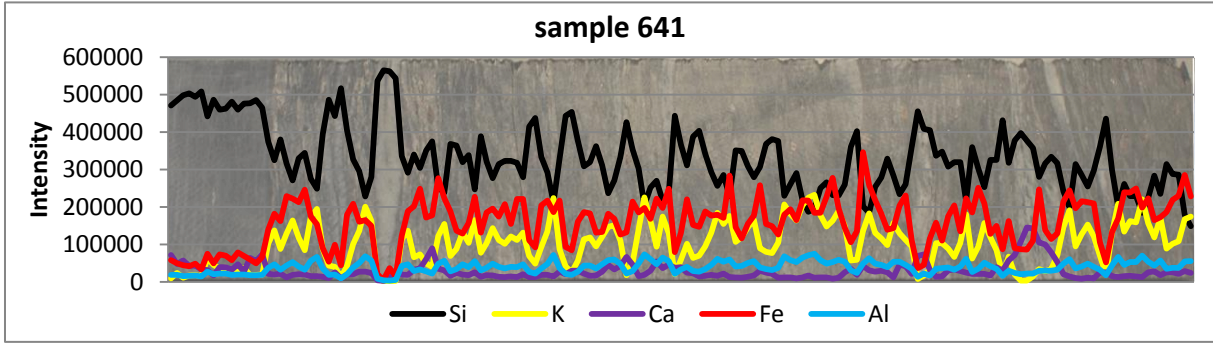
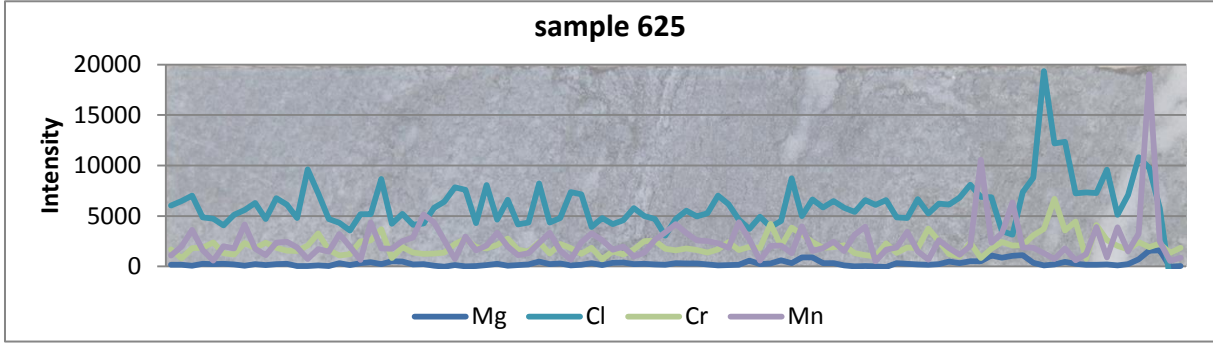
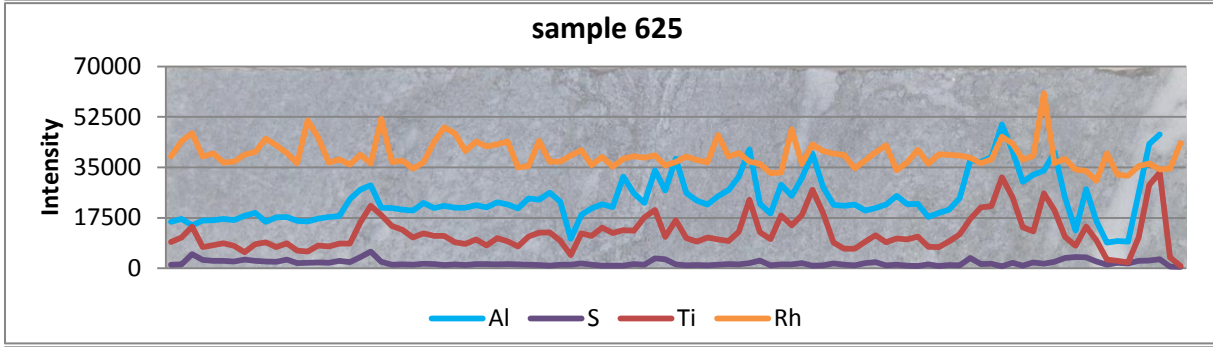
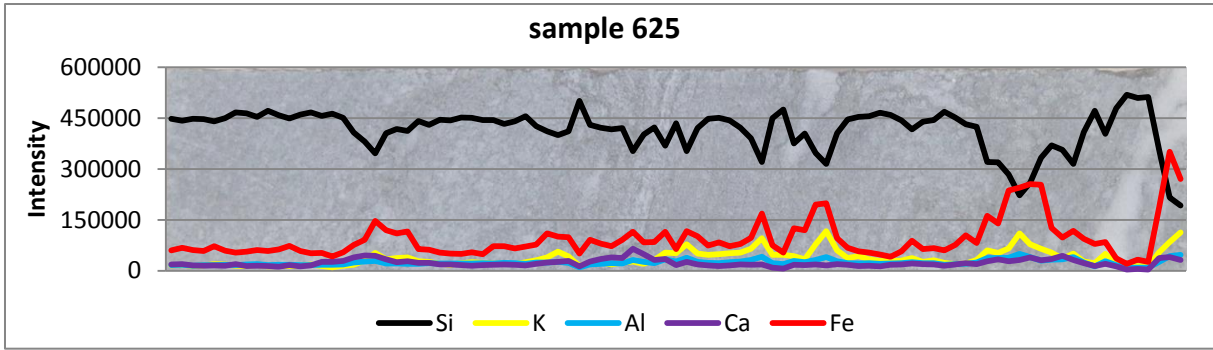


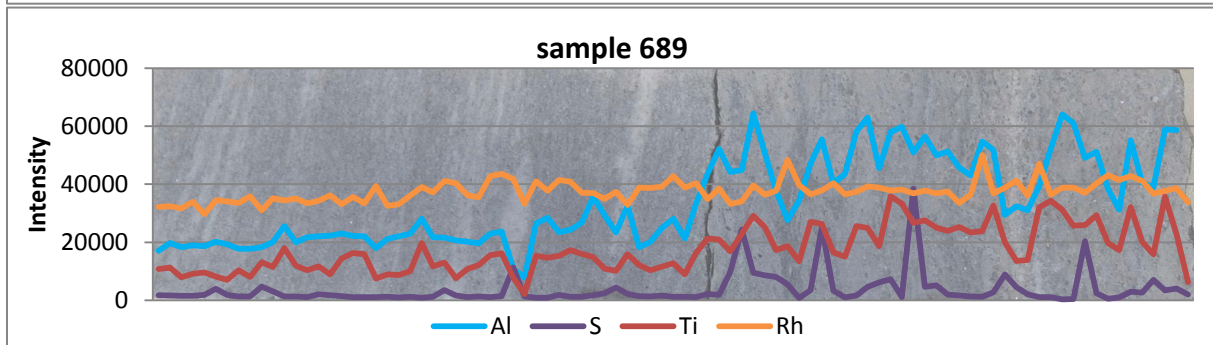
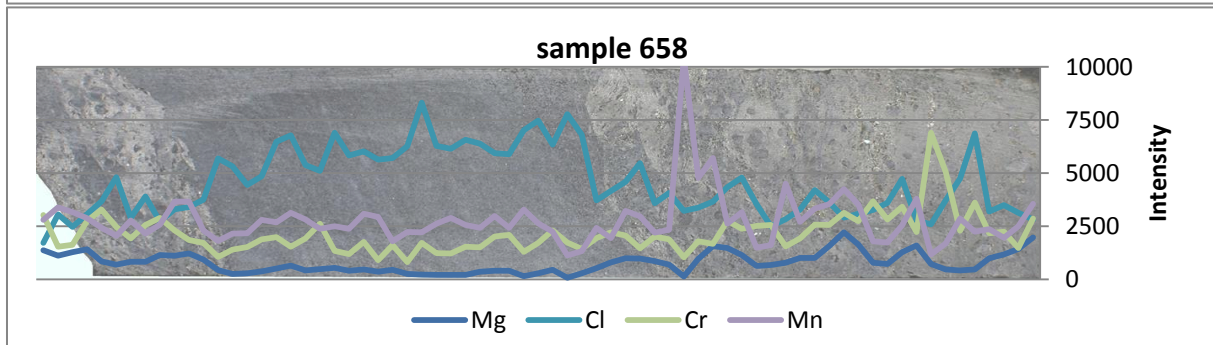
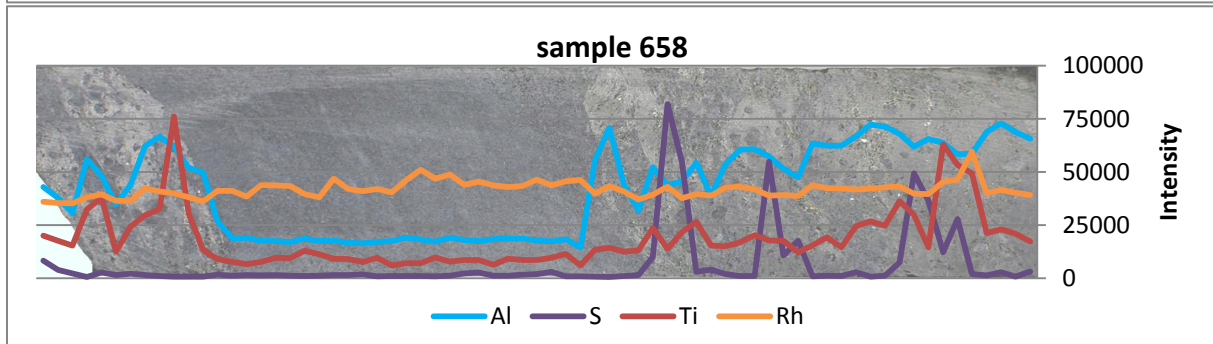
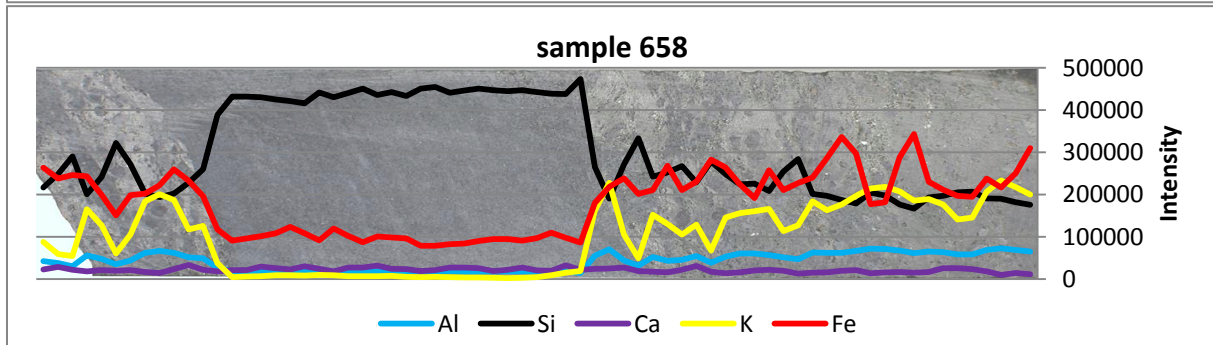
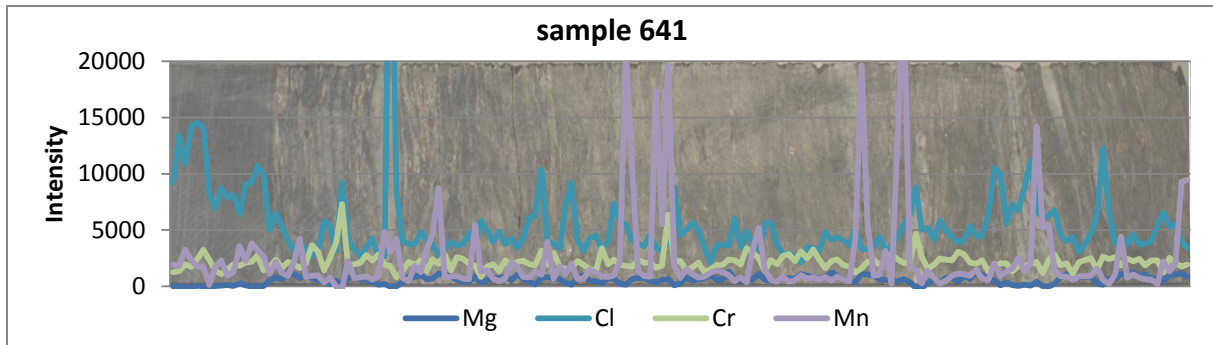


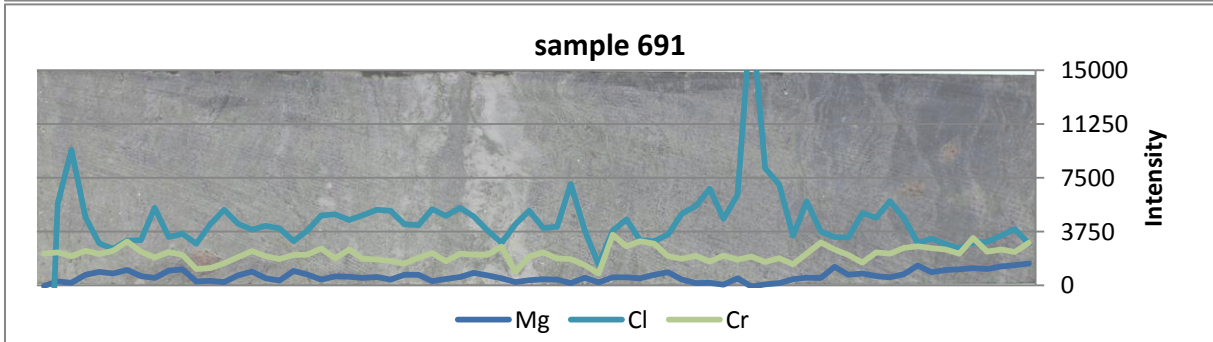
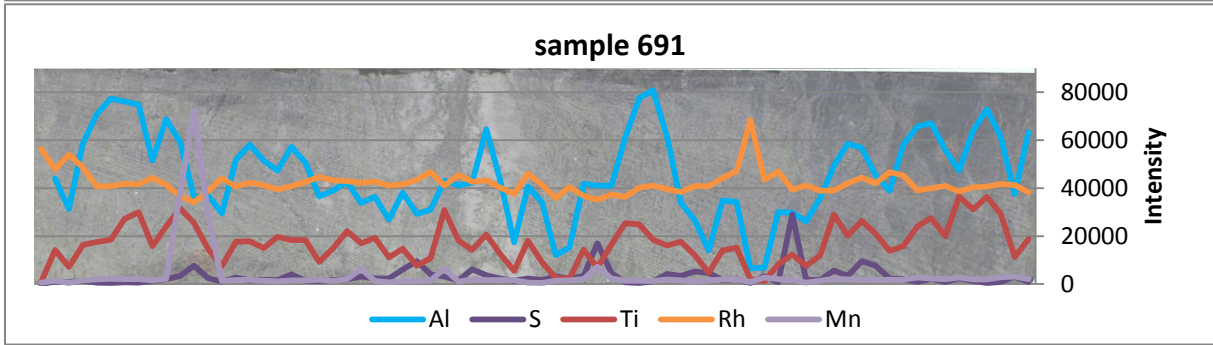
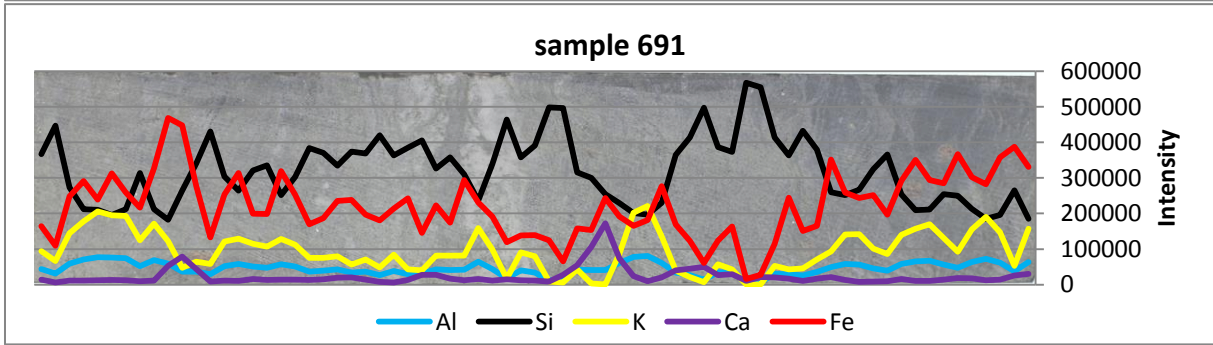
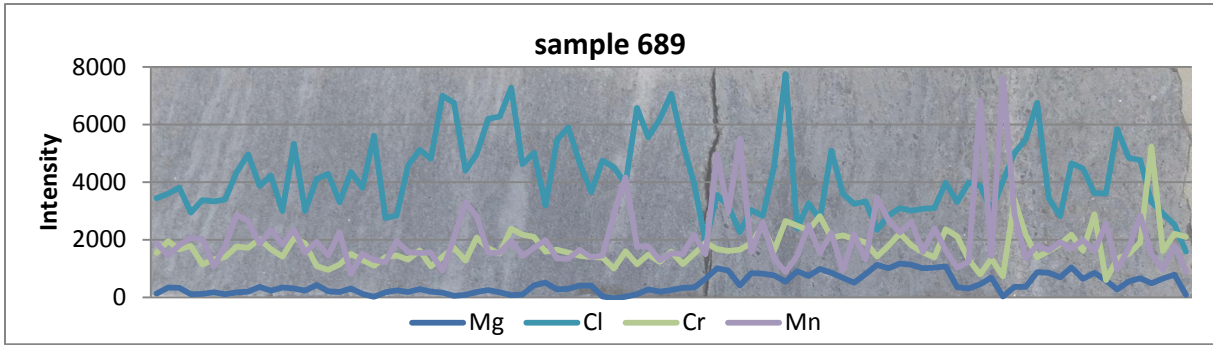


10.3 XRF RESULTS OF THE AVATECH CORE SCANNER

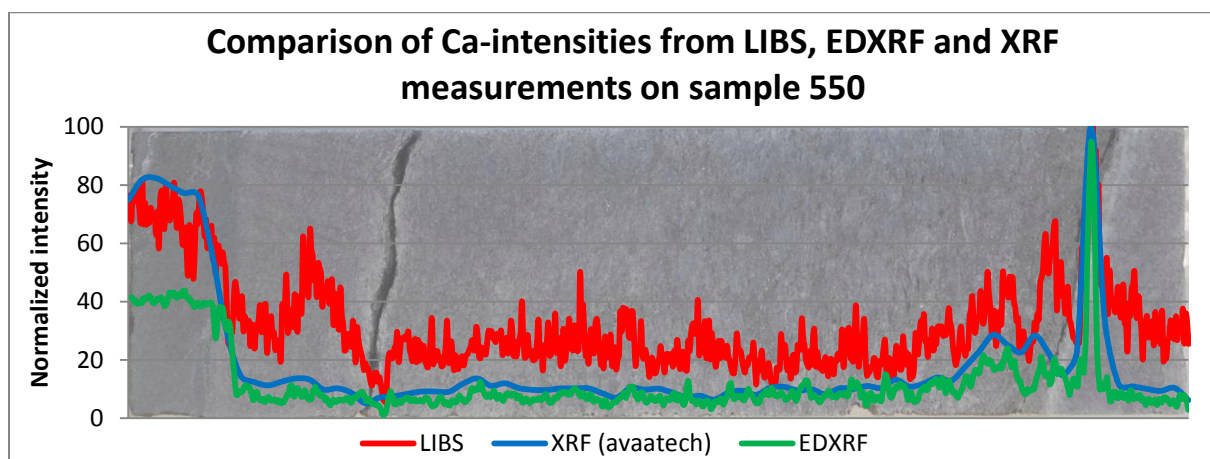
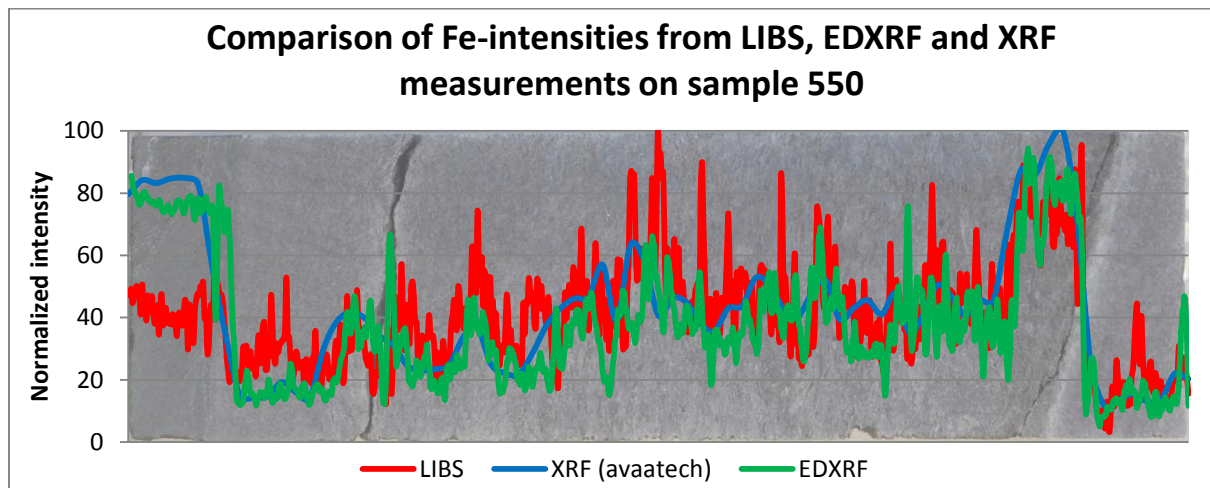
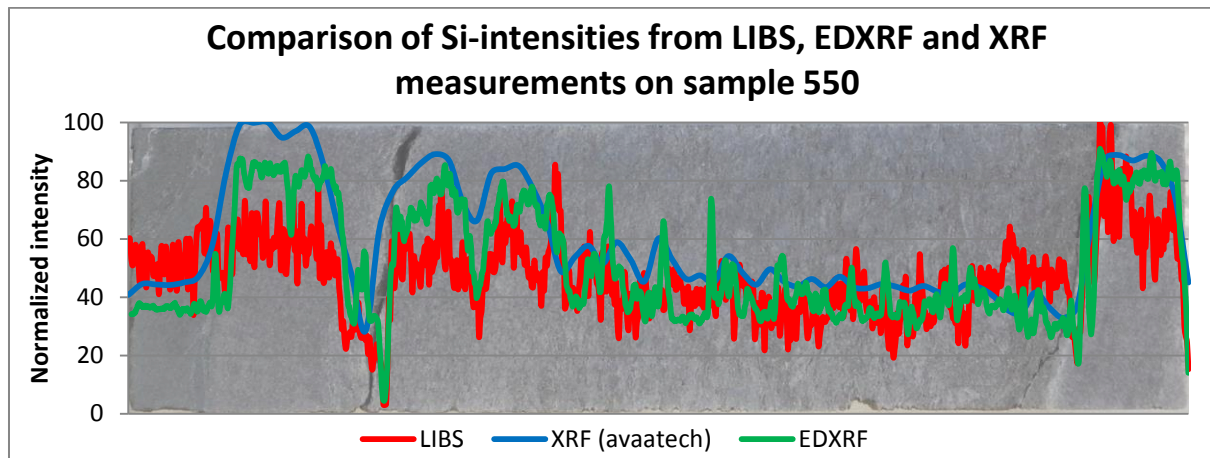


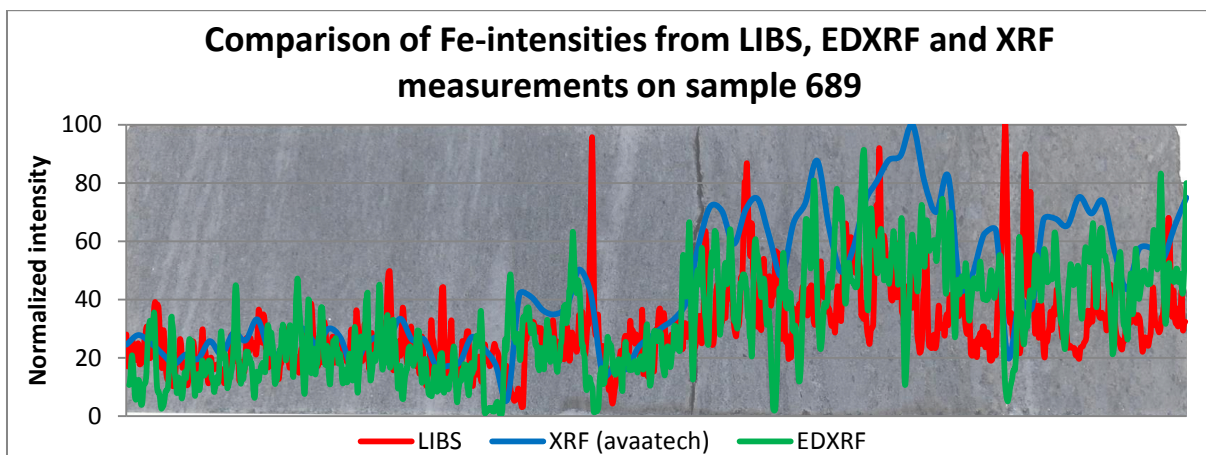
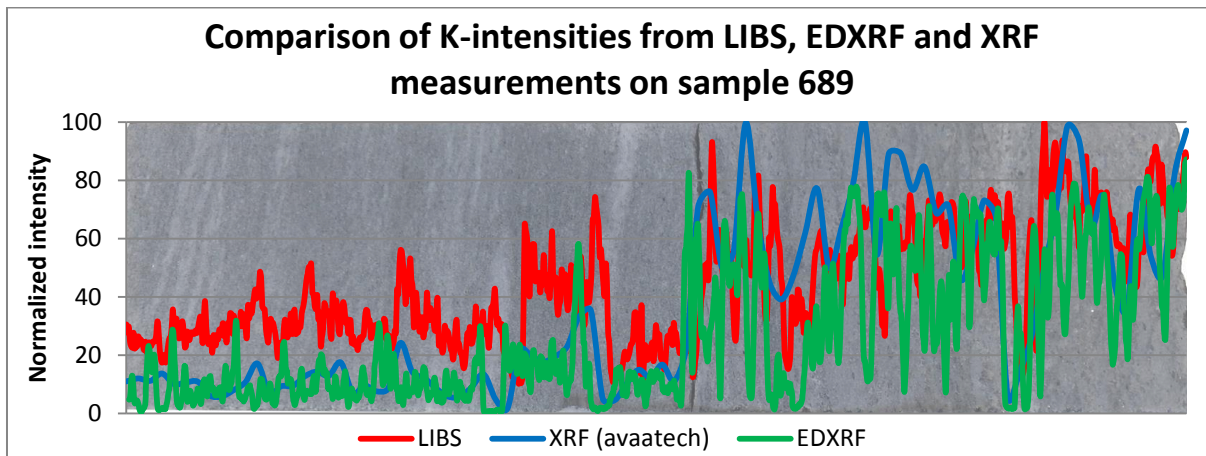
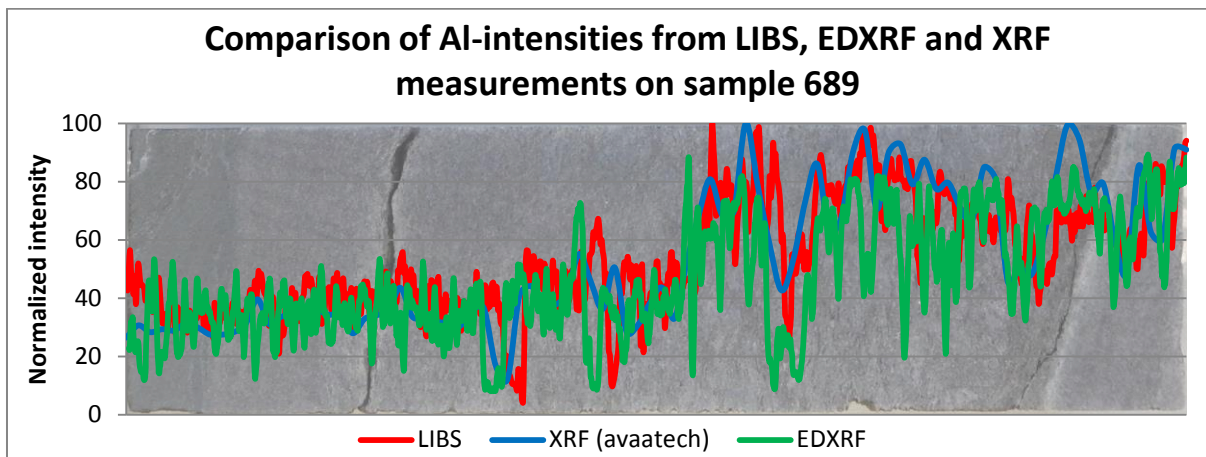
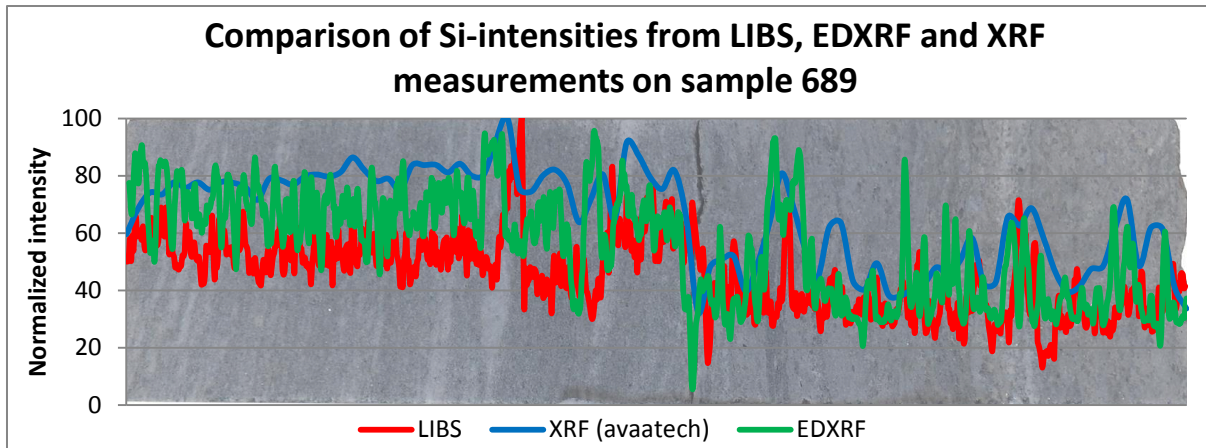






10.4 DIAGRAMS FOR COMPARISON OF THE EDXRF CS TORNADO M4, THE LIBS CS AND THE AVAATECH CS





10.5 CORE SAMPLE PHOTOS (ON A SCALE 1:1)

550



578



625



658



689



691



641





ISSN 2190-7110